

Vector-Leptoquark Interpretation  
of the ATLAS Search for Top Squarks  
with Decays via Tau Sleptons  
in Run-2 of the LHC



Ludwig-Maximilians-Universität München  
Faculty of Physics  
Master Thesis

presented by  
**Kyeong Ro Lee**  
born in Seoul

Munich, June 28th, 2021

Supervisor: PD Dr. Alexander Mann



# Vektor-Leptoquark-Interpretation der ATLAS-Suche nach Top-Squarks mit Zerfällen über Tau-Sleptonen in Run 2 des LHC



Masterarbeit an der Fakultät für Physik  
der  
Ludwig-Maximilians-Universität München

vorgelegt von  
**Kyeong Ro Lee**  
geboren in Seoul

München, den 28.06.2021

Gutachter: PD Dr. Alexander Mann



Leptoquarks (LQ) are hypothetical bosons proposed in various extensions [1–5] of the Standard Model (SM) of elementary particles. As leptoquarks carry both baryon and lepton numbers, they can provide connections between the quark and lepton sectors of the Standard Model. Leptoquark also provides an explanation for Lepton Flavor Universality (LFU) violation, whose hints were found in physics of B-mesons [6–13]. Leptoquarks can be either scalar (spin-0) or vector (spin-1) bosons and can be classified according to their gauge quantum numbers [14]. All leptoquarks carry color charge and fractional electric charge, interacting via strong and electroweak interactions. Vector leptoquarks have additional parameters that determine their nature. Depending on the value of the parameters, vector leptoquark can be a new gauge boson (Yang-Mills case) or just a strongly-interacting vector boson (minimal coupling) which could be a composite resonance state. The  $U_1$  vector leptoquark [15] is an  $SU(2)_W$  singlet that interacts via  $U(1)_Y$  and  $SU(3)_C$  gauge bosons. This leptoquark is proposed as one of the candidates for the B-anomalies [16, 17].

Supersymmetry (SUSY) is a framework of theories extending the Standard Model by introducing partners of each particle constituting it. Top squark and tau slepton are supersymmetric partners of the top quark and tau lepton, having the same quantum number as their SM counterparts except being spin-0. Top squarks can be produced in pairs at the Large Hadron Collider (LHC) via proton-proton collision. They can decay via tau sleptons, leaving tau leptons, b-jets and missing energy in the final states.

As pair production of leptoquarks at the LHC can have similar final states, search for the top squarks and tau sleptons can also be optimized for leptoquarks. This work presents a vector leptoquark interpretation of the search for top squarks decaying via tau sleptons, which was simultaneously optimized for third-generation scalar leptoquarks. The analysis uses the full Run-2 data taken by the ATLAS detector between 2015 and 2018, with integrated luminosity of  $139 \text{ fb}^{-1}$ . A parameter space consisting of the mass of leptoquark ( $m(\text{LQ})$ ) and branching ratio to charged leptons ( $B(\text{LQ} \rightarrow b\tau)$ ) is scanned. The  $U_1$  vector leptoquark is excluded up to around 1.8 TeV (1.5 TeV) for Yang-Mills (minimal coupling) case and intermediate branching ratio.



<b>1</b>	<b>Theoretical Overview</b>	<b>1</b>
1.1	The Standard Model of Elementary Particles . . . . .	1
1.1.1	Lagrangian Formulation . . . . .	1
1.1.2	Quantum Electrodynamics and Local Gauge Invariance . . . . .	3
1.1.3	Quantum Chromodynamics . . . . .	5
1.1.4	Higgs Mechanism and Electroweak Unification . . . . .	6
1.1.5	Particle Contents of the Standard Model . . . . .	9
1.2	Shortcomings of the Standard Model . . . . .	11
1.3	Supersymmetry . . . . .	12
1.4	Leptoquark . . . . .	13
1.4.1	Hints from B-anomalies . . . . .	15
1.4.2	Classification of Leptoquarks . . . . .	17
1.4.3	Production Mechanism of Leptoquarks at Hadron Colliders . . . . .	17
1.4.4	Simplified Scalar Leptoquark . . . . .	18
1.4.5	The $U_1$ Vector Leptoquark . . . . .	19
<b>2</b>	<b>Experimental Setup</b>	<b>21</b>
2.1	The Large Hadron Collider . . . . .	21
2.2	The ATLAS Detector . . . . .	22
2.3	ATLAS Data Taking . . . . .	24
2.4	Particle Reconstruction . . . . .	25
<b>3</b>	<b>Data Set and Simulation</b>	<b>27</b>
3.1	ATLAS Data . . . . .	27
3.2	Signal . . . . .	27
3.3	Standard Model Backgrounds . . . . .	30

<b>4</b>	<b>Analysis Strategy</b>	<b>33</b>
4.1	Cut-Based Analysis . . . . .	33
4.2	The $CL_s$ Method . . . . .	36
4.3	Discovery and Exclusion Fits . . . . .	37
4.4	Upper Limits . . . . .	38
<b>5</b>	<b>Comparison of Scalar and Vector Leptoquark</b>	<b>39</b>
5.1	Production Cross Section . . . . .	39
5.2	Decay Width and Branching Ratio . . . . .	40
5.3	Kinematics . . . . .	44
5.4	Comparison in the SR . . . . .	50
<b>6</b>	<b>Theoretical Uncertainties</b>	<b>53</b>
6.1	Uncertainties in Production Cross Section . . . . .	53
6.2	Uncertainties in Acceptance . . . . .	57
<b>7</b>	<b>Results</b>	<b>59</b>
7.1	Signal Contamination . . . . .	59
7.2	Kinematic Distributions in the Signal Regions . . . . .	62
7.3	Exclusion Limits . . . . .	64
<b>8</b>	<b>Conclusion and Outlook</b>	<b>67</b>
	<b>Bibliography</b>	<b>69</b>
<b>A</b>	<b>List of Signal Samples</b>	<b>77</b>
<b>B</b>	<b>Decay Width of Leptoquarks</b>	<b>81</b>
B.1	Decay Width of Scalar Leptoquarks . . . . .	81
B.2	Decay Width of Vector Leptoquarks . . . . .	83
<b>C</b>	<b>Additional Plots</b>	<b>87</b>
C.1	Kinematics . . . . .	87
C.2	Observed $CL_s$ Values . . . . .	97
C.3	Observed Upper Limits on Cross Section . . . . .	99

## 1.1 The Standard Model of Elementary Particles

The Standard Model (SM) of particle physics is the theory that describes fundamental constituents of the nature and their interactions except gravity. In this section, a theoretical summary of the Standard Model is presented, which can be found in many textbooks [18–21] with more detail.

### 1.1.1 Lagrangian Formulation

Including the Standard Model, many theories in particle physics are based on Lagrangian formulation of quantum field theory. In this point of view, constructing a theory is finding a plausible Lagrangian density  $\mathcal{L}$  as a function of fields  $\phi_i$  and their derivatives. The equation of motion that  $\phi_i$  obeys is derived using the Euler-Lagrange equation:

$$\frac{\partial \mathcal{L}}{\partial \phi_i} - \partial_\mu \left( \frac{\partial \mathcal{L}}{\partial (\partial_\mu \phi_i)} \right) = 0. \quad (1.1)$$

Noether's theorem states that each continuous symmetry of a field is related to a conservation law. This principle gives rise to fundamental laws of physics, such as conservation of energy and momentum.

The Lorentz-invariant Lagrangian of a real scalar field is

$$\mathcal{L}_{\text{Klein-Gordon}} = \frac{1}{2} (\partial_\mu \phi) (\partial^\mu \phi) - \frac{1}{2} m^2 \phi^2, \quad (1.2)$$

while for a complex scalar field

$$\mathcal{L}_{\text{Klein-Gordon}} = (\partial_\mu \phi)^\dagger (\partial^\mu \phi) - m^2 \phi^\dagger \phi. \quad (1.3)$$

Both Lagrangians are Lorentz invariant and lead to the Klein-Gordon equation

$$(\partial_\mu \partial^\mu + m^2) \phi \equiv (\square + m^2) \phi = 0, \quad (1.4)$$

which is the equation of motion for a free spin-0 particle with mass  $m$ . The scalar field  $\phi$  is quantized using plane-wave solutions of eq. (1.4) and creation- ( $a_{\mathbf{p}}^\dagger$ ) and annihilation ( $a_{\mathbf{p}}$ )

operators:

$$\phi(x) = \int \frac{d^3p}{(2\pi)^3} \frac{1}{\sqrt{2E_{\mathbf{p}}}} \left( a_{\mathbf{p}} e^{-ip \cdot x} + a_{\mathbf{p}}^\dagger e^{ip \cdot x} \right), \quad (1.5)$$

where  $E_{\vec{p}} = p^0$ . It can be shown that eq. (1.5) satisfies eq. (1.4).

The Lorentz invariant Lagrangian of a free spin- $\frac{1}{2}$  particle is

$$\mathcal{L}_{\text{Dirac}} = \bar{\psi} (i\gamma^\mu \partial_\mu - m) \psi \equiv \bar{\psi} (i\rlap{\not{D}} - m) \psi \quad (1.6)$$

where  $\bar{\psi}$  is defined as  $\psi^\dagger \gamma^0$ . Applying the Euler-Lagrange equation to the Dirac Lagrangian leads to the Dirac equation

$$(i\rlap{\not{D}} - m) \psi(x) = 0, \quad (1.7)$$

which is the equation of motion for a free spin- $\frac{1}{2}$  particle with mass  $m$ . For a field  $\psi$  that obeys eq. (1.7),

$$j^\mu = \bar{\psi} \gamma^\mu \psi \quad (1.8)$$

is a conserved current, i.e.  $\partial_\mu j^\mu = 0$ . This can be interpreted as the probability current of the Dirac field. The spinor fields are quantized as

$$\psi(x) = \int \frac{d^3p}{(2\pi)^3} \frac{1}{\sqrt{2E_{\mathbf{p}}}} \sum_{\text{spins}} \left( a_{\mathbf{p}}^s u^s(p) e^{-ip \cdot x} + b_{\mathbf{p}}^{s\dagger} v^s(p) e^{ip \cdot x} \right) \quad (1.9)$$

and satisfy eq. (1.7). In physics of elementary particles, the particles constituting the matter are spin- $\frac{1}{2}$  particles.

The Lorentz-invariant Lagrangian of a free spin-1 particle is

$$\mathcal{L}_{\text{Proca}} = -\frac{1}{4} F_{\mu\nu} F^{\mu\nu} + \frac{m^2}{2} A_\mu A^\mu \quad (1.10)$$

for a real vector field  $A_\mu$ . If the field  $A_\mu$  is complex, the correct Lagrangian is

$$\mathcal{L}_{\text{Proca}} = -\frac{1}{2} F_{\mu\nu}^\dagger F^{\mu\nu} + m^2 A_\mu^\dagger A^\mu. \quad (1.11)$$

The field strength tensor in eqs. (1.10) and (1.11) is defined as

$$F_{\mu\nu} = \partial_\mu A_\nu - \partial_\nu A_\mu. \quad (1.12)$$

Applying the Euler-Lagrange equation to the Proca Lagrangian, the resulting equation of motion is the Proca equation

$$\partial_\mu F^{\mu\nu} + m^2 A^\nu = 0. \quad (1.13)$$

The vector field  $A_\mu$  can be quantized using plane-wave solutions of eq. (1.13):

$$A_\mu(x) = \int \frac{d^3p}{(2\pi)^3} \frac{1}{\sqrt{2E_{\mathbf{p}}}} \sum_{\text{spins}} \left( a_{\mathbf{p}}^s \epsilon_\mu^s(p) e^{-ip \cdot x} + a_{\mathbf{p}}^{s\dagger} \epsilon_\mu^{s*}(p) e^{ip \cdot x} \right) \quad (1.14)$$

where  $\epsilon_\mu^s$  are the polarization vectors.

### 1.1.2 Quantum Electrodynamics and Local Gauge Invariance

The classical theory of electrodynamics, formulated by Maxwell, can be rewritten in Lagrangian formulation:

$$\mathcal{L}_{\text{Maxwell}} = -\frac{1}{4}F_{\mu\nu}F^{\mu\nu} - j^\mu A_\mu, \quad (1.15)$$

where  $j^\mu$  is the electromagnetic source and  $F_{\mu\nu}$  is defined as in eq. (1.12). Applying eq. (1.1) to eq. (1.15), the resulting equation of motion

$$\partial_\mu F^{\mu\nu} = j^\nu \quad (1.16)$$

is the inhomogeneous part of Maxwell's equations (Gauss' law and Ampère's law with Maxwell's modification). Furthermore, eq. (1.12) satisfies the Bianchi identity

$$\partial_\mu F_{\nu\lambda} + \partial_\nu F_{\lambda\mu} + \partial_\lambda F_{\mu\nu} = 0, \quad (1.17)$$

which becomes the homogeneous part of Maxwell's equations (Gauss' law for magnetism and Faraday's law). In classical electrodynamics, the electromagnetic potential can undergo arbitrary 'gauge' transformation without changing the physics<sup>1</sup>:

$$\begin{aligned} \mathbf{A} &\rightarrow \mathbf{A} + \nabla\Lambda \\ V &\rightarrow V - \frac{\partial\Lambda}{\partial t} \end{aligned}$$

or, in four-vector notation,

$$A_\mu \rightarrow A_\mu - \partial_\mu\Lambda \quad (1.18)$$

where  $\Lambda$  is a function of position and time. This is one of the key ideas used in more sophisticated theories of fundamental interactions.

To construct 'quantum' electrodynamics, it is essential to describe a fermion field  $\psi$  interacting with a vector field  $A_\mu$ . The first term to include is the free Dirac Lagrangian in eq. (1.6). The next part is the homogeneous case of eq. (1.15)

$$-\frac{1}{4}F_{\mu\nu}F^{\mu\nu},$$

which also is the massless case of eq. (1.13). To describe the interaction between the fermion  $\psi$  and photon  $A_\mu$ , the source term  $-j^\mu A_\mu$  in eq. (1.15) needs to be understood properly. The electromagnetic current  $j^\mu$  can be thought of as the charge times the probability current of the fermion in eq. (1.8):

$$j^\mu = q\bar{\psi}\gamma^\mu\psi. \quad (1.19)$$

Therefore the Lagrangian of an electromagnetically interacting fermion becomes

$$\mathcal{L}_{\text{QED}} = \bar{\psi}(i\cancel{\partial} - m)\psi - \frac{1}{4}F_{\mu\nu}F^{\mu\nu} - q\bar{\psi}\gamma^\mu\psi A_\mu. \quad (1.20)$$

In quantum electrodynamics (QED), one can imagine a global phase rotation

$$\psi(x) \rightarrow e^{i\alpha}\psi(x) \quad (1.21)$$

---

<sup>1</sup>What we measure is the electric or magnetic field, not the potential itself.

where  $\alpha$  is a constant. The physics remains unchanged since the Lagrangian is invariant under this transformation. In fact, the QED Lagrangian is invariant under even more general transformation

$$\psi(x) \rightarrow e^{i\alpha(x)}\psi(x), \quad (1.22)$$

provided the vector field  $A_\mu$  transforms together:

$$A_\mu \rightarrow A_\mu - \frac{1}{q}\partial_\mu\alpha(x), \quad (1.23)$$

which is exactly the gauge transformation of classical electrodynamics given in eq. (1.18). Such transformations form a unitary group  $U(1)$ .

Taking this *local gauge invariance* as a fundamental principle of physics, the quantum electrodynamics can be completely restored by constructing a gauge invariant Dirac Lagrangian. The fermion mass term  $-m\bar{\psi}\psi$  in eq. (1.20) is already invariant under local gauge transformations. To add any term including derivative of  $\psi$ , one needs to see which problem the normal derivative has. The derivative of  $\psi$  in in direction of  $n^\mu$  can be expressed as

$$n^\mu\partial_\mu\psi = \lim_{\epsilon \rightarrow 0} \frac{1}{\epsilon} [\psi(x + \epsilon n) - \psi(x)].$$

For general case of local phase rotation,  $\psi(x + \epsilon n)$  and  $\psi(x)$  transform differently. By defining a quantity  $U(y, x)$  that compensates the difference with the following properties:

$$\begin{aligned} U(x, x) &= 1 \\ U(y, x) &\rightarrow e^{i\alpha(y)}U(y, x)e^{-i\alpha(x)}, \end{aligned}$$

it follows that

$$\begin{aligned} \psi(y) &\rightarrow e^{i\alpha(y)}\psi(y) \\ U(y, x)\psi(x) &\rightarrow e^{i\alpha(y)}U(y, x)\psi(x). \end{aligned}$$

Therefore a modified definition of derivative

$$n^\mu D_\mu\psi = \lim_{\epsilon \rightarrow 0} \frac{1}{\epsilon} [\psi(x + \epsilon n) - U(x + \epsilon n, x)\psi(x)] \quad (1.24)$$

makes sense since  $\psi(x + \epsilon n)$  and  $U(x + \epsilon n, x)\psi(x)$  transform in the same manner. Expanding  $U(x + \epsilon n, x)\psi(x)$  to the first order of  $\epsilon$ , it can be shown that  $D_\mu$  must have a form of

$$D_\mu = \partial_\mu + iqA_\mu(x) \quad (1.25)$$

where a vector field  $A_\mu$  has appeared. Inserting eqs. (1.22) and (1.23) to eq. (1.25), it can be shown that  $D_\mu\psi(x)$  transforms the same as  $\psi(x)$  under local gauge transformations:

$$D_\mu\psi(x) \rightarrow e^{i\alpha(x)}D_\mu\psi(x).$$

Therefore it makes sense to call  $D_\mu$  the gauge-covariant derivative or simply *covariant derivative*. Furthermore, applying the commutator of covariant derivatives to  $\psi(x)$ , it can be shown that the commutator is invariant:

$$[D_\mu, D_\nu]\psi(x) \rightarrow e^{i\alpha(x)}[D_\mu, D_\nu]\psi(x). \quad (1.26)$$

Evaluating the commutator of covariant derivative,

$$[D_\mu, D_\nu] = iqF_{\mu\nu}. \quad (1.27)$$

From eqs. (1.26) and (1.27), it is shown that the field strength tensor  $F_{\mu\nu}$  is invariant under local gauge transformation as in the classical electrodynamics.

Summarizing all of these, the minimal Lagrangian invariant under Lorentz transformations and  $U(1)$  local gauge transformations is the QED Lagrangian:

$$\mathcal{L}_{\text{QED}} = \bar{\psi} (i\not{D} - m) \psi - \frac{1}{4} F_{\mu\nu} F^{\mu\nu}. \quad (1.28)$$

Yang and Mills [22] expanded this idea of local gauge transformation to more general continuous groups. For a doublet of fermions

$$\psi = \begin{pmatrix} \psi_1(x) \\ \psi_2(x) \end{pmatrix} \quad (1.29)$$

and transformation

$$\psi(x) \rightarrow V(x)\psi(x) = \exp\left\{i\alpha^k(x)\frac{\tau^k}{2}\right\}\psi(x) \quad (1.30)$$

where  $\alpha^k(x)$  are real functions and  $\tau^k$  are the Pauli matrices, the covariant derivative becomes

$$D_\mu = \partial_\mu - igA_\mu^k \frac{\tau^k}{2}, \quad (1.31)$$

which implies that three vector fields  $A_\mu^1(x)$ ,  $A_\mu^2(x)$  and  $A_\mu^3(x)$  have appeared. The transformation in eq. (1.30) construct an  $SU(2)$  group, which is a nonabelian special unitary group. In this case, the vector fields transform differently:

$$\vec{A}_\mu \rightarrow \vec{A}_\mu + \frac{1}{g}\partial_\mu\vec{\alpha} - \vec{\alpha} \times \vec{A}_\mu. \quad (1.32)$$

The commutator of covariant derivatives becomes

$$[D_\mu, D_\nu] = -ig\vec{F}_{\mu\nu} \cdot \frac{\vec{\tau}}{2} \quad (1.33)$$

where the definition of field strength tensor has changed:

$$\vec{F}_{\mu\nu} = \partial_\mu\vec{A}_\nu - \partial_\nu\vec{A}_\mu + g\vec{A}_\mu \times \vec{A}_\nu. \quad (1.34)$$

In Yang-Mills theory, the field strength tensor is not invariant under local gauge transformation anymore:

$$\vec{F}_{\mu\nu} \rightarrow \vec{F}_{\mu\nu} - \vec{\alpha} \times \vec{F}_{\mu\nu}. \quad (1.35)$$

However, it is still possible to construct a gauge-invariant Lagrangian

$$\mathcal{L}_{\text{YM}} = \bar{\psi} (i\not{D} - m) \psi - \frac{1}{4} F_{\mu\nu}^i F^{i\mu\nu}, \quad (1.36)$$

which predicts three massless vector bosons.

### 1.1.3 Quantum Chromodynamics

While the similarity between proton and neutron was the motivation of isospin, Gell-Mann [23] and Ne'man [24] took notice of the  $SU(3)$  symmetry<sup>2</sup> in the property of baryons and mesons

<sup>2</sup>This is a broken symmetry, since the hadrons have different masses.

known at the time. To account for their quantum numbers, Gell-Mann [25] and Zweig [26, 27] introduced three elementary particles - up ( $u$ ), down ( $d$ ) and strange ( $s$ ) quarks. However,  $\Delta^{++}$  ( $uuu$ ),  $\Delta^-$  ( $ddd$ ) and  $\Omega^-$  ( $sss$ ) become inconsistent with Pauli's exclusion principle, since these baryons consist of three identical fermions with symmetric spatial and spin configurations. This can be solved by introducing color charges [28], consisting of *red*, *green* and *blue*. The color charges generate the  $SU(3)_C$  symmetry which is analogous to the flavor  $SU(3)$  symmetry. In this model, baryons consist of three quarks with three different colors, while mesons consist of a quark and antiquark with the same color and anticolor.

As an  $SU(3)_C$ -analogy of the Yang-Mills theory, the Quantum Chromodynamics predicts eight vector fields appearing in the covariant derivative

$$D_\mu = \partial_\mu - ig_s G_\mu^a \frac{\lambda^a}{2}, \quad (1.37)$$

where  $\lambda^a$  are the Gell-Mann matrices. The vector bosons  $G_\mu^a$  are gluons, the mediators of strong interaction. The field strength tensor becomes

$$G_{\mu\nu}^a = \partial_\mu G_\nu^a - \partial_\nu G_\mu^a + g_s f_{abc} G_\mu^b G_\nu^c \quad (1.38)$$

where  $f_{abc}$  are the structure constants of  $SU(3)$ . As in the Yang-Mills theory, it is possible to construct a Lagrangian invariant under  $SU(3)$  local gauge transformations:

$$\begin{aligned} \mathcal{L}_{\text{QCD}} &= \bar{\psi} (i\not{D} - m) \psi - \frac{1}{4} G_{\mu\nu}^a G^{a\mu\nu} \\ &= \bar{\psi} (i\not{\partial} - m) \psi + g_s \bar{\psi} \gamma^\mu \frac{\lambda^a}{2} \psi G_\mu^a - \frac{1}{4} G_{\mu\nu}^a G^{a\mu\nu}. \end{aligned} \quad (1.39)$$

#### 1.1.4 Higgs Mechanism and Electroweak Unification

Interpreting the new vector bosons of the Yang-Mills theory as mediators of the weak interaction raises a serious problem. Once the gauge bosons are given nonzero mass, the local gauge invariance of the theory does not hold anymore. At the time the Yang-Mills theory was formulated, the existence of the weak force had already been known and its short range was predicting heavy mediators.

This contradiction can be resolved by introducing spontaneous symmetry breaking and local gauge invariance together, as formulated independently by Englert and Brout [29], Higgs [30], Guralnik, Hagen and Kibble [31]. Introducing a potential term to the Lagrangian where the vacuum state does not need to be invariant under gauge transformations, expansion of the Lagrangian near the vacuum state introduces a massive scalar field and mass terms for the gauge bosons. Meanwhile, Goldstone's theorem [32] states that every spontaneously broken continuous symmetry gives rise to a massless scalar field called the Goldstone boson. The experimental absence of such massless scalar boson can be explained if the entire Lagrangian is still invariant under local gauge transformations. Choosing an appropriate local gauge transformation, the terms for Goldstone boson disappear from the Lagrangian, which is often said each gauge boson eats a Goldstone boson by acquiring mass and an additional degree of freedom. By this mechanism which is often called the Higgs mechanism, various gauge theories with massive mediators can be constructed using plausible gauge groups.

Weinberg [33] applied the Higgs mechanism to Glashow's attempt to unify EM and weak interactions [34]. Introducing a doublet of complex scalar fields

$$\phi = \begin{pmatrix} \phi^+ \\ \phi^0 \end{pmatrix}$$

described by the Higgs Lagrangian

$$\begin{aligned}\mathcal{L}_{\text{Higgs}} &= (D_\mu\phi)^\dagger (D^\mu\phi) - V(\phi) \\ &= (D_\mu\phi)^\dagger (D^\mu\phi) + \mu^2\phi^\dagger\phi - \lambda(\phi^\dagger\phi)^2,\end{aligned}\quad (1.40)$$

the potential term  $V(\phi)$  can be minimized at  $\phi^\dagger\phi = \frac{\mu^2}{2\lambda}$ . The Lagrangian in eq. (1.40) is invariant under  $SU(2)$  and  $U(1)$  gauge transformations

$$\phi(x) \rightarrow e^{i\alpha^k(x)\frac{\tau^k}{2}} e^{i\frac{\beta(x)}{2}}\phi(x) \quad (1.41)$$

where  $\tau^k$  ( $k = 1, 2, 3$ ) are the Pauli matrices and  $D_\mu\phi$  is the appropriate covariant derivative. This transformation resembles a composition of the isospin transition in Yang-Mills theory and a QED-like transformation. The covariant derivative becomes

$$D_\mu = \partial_\mu - igA_\mu^k\frac{\tau^k}{2} - i\frac{g'}{2}B_\mu \quad (1.42)$$

where  $A_\mu^k$  and  $B_\mu$  are the gauge bosons of  $SU(2)$  and  $U(1)$ . By spontaneous symmetry breaking, the doublet  $\phi$  gets a vacuum expectation value

$$\langle\phi\rangle = \frac{1}{\sqrt{2}}\begin{pmatrix} 0 \\ v \end{pmatrix} \quad (1.43)$$

where  $v = \sqrt{\frac{\mu^2}{\lambda}}$ . The quadratic terms of the gauge bosons

$$\begin{aligned}\Delta\mathcal{L} &= \left( (-igA_\mu\tau - i\frac{1}{2}g'B_\mu)\langle\phi\rangle \right)^\dagger \left( (-igA^\mu\tau - i\frac{1}{2}g'B^\mu)\langle\phi\rangle \right) \\ &= \frac{v^2}{8} [g^2(A_\mu^1)^2 + g^2(A_\mu^2)^2 + (-gA_\mu^3 + g'B_\mu)^2]\end{aligned}\quad (1.44)$$

naturally appear, showing that three vector bosons acquire mass:

$$W_\mu^\pm = \frac{1}{\sqrt{2}}(A_\mu^1 \mp iA_\mu^2), \quad m_W = \frac{gv}{2} \quad (1.45)$$

$$Z_\mu^0 = \frac{1}{\sqrt{g^2 + g'^2}}(gA_\mu^3 - g'B_\mu), \quad m_Z = \sqrt{g^2 + g'^2}\frac{v}{2} \quad (1.46)$$

while one vector boson

$$A_\mu = \frac{1}{\sqrt{g^2 + g'^2}}(g'A_\mu^3 + gB_\mu) \quad (1.47)$$

remains massless. The massive vector bosons in eqs. (1.45) and (1.46) can be interpreted as charged and neutral weak bosons respectively, while the massless boson in eq. (1.47) is interpreted as the photon. Indeed, assuming that the fermionic terms are invariant under  $SU(2) \times U(1)$  gauge transformations, the covariant derivative for fermions becomes

$$\begin{aligned}D_\mu &= \partial_\mu - igA_\mu^k T^k - ig'Y B_\mu \\ &= \partial_\mu - i\frac{g}{\sqrt{2}}(W_\mu^+ T^+ + W_\mu^- T^-) - i\frac{1}{\sqrt{g^2 + g'^2}}Z_\mu(g^2 T^3 - g'^2 Y) \\ &\quad - i\frac{gg'}{\sqrt{g^2 + g'^2}}A_\mu(T^3 + Y)\end{aligned}\quad (1.48)$$

where  $T^k = \frac{\tau^k}{2}$ ,  $T^\pm = T^1 \pm iT^2$  and  $Y$  is the *hypercharge* of the fermion. Interpreting  $\frac{gg'}{\sqrt{g^2+g'^2}}$  as the elementary charge  $e$  and setting  $I^3 + Y = Q$  where  $I^3$  is the eigenvalue of  $T^3$ , the photon term in eq. (1.48) is identical to the QED covariant derivative. Introducing the Weinberg angle  $\theta_W$ , eqs. (1.46) to (1.48) can be further simplified to

$$\begin{aligned} Z_\mu^0 &= A_\mu^3 \cos \theta_W - B_\mu \sin \theta_W \\ A_\mu &= A_\mu^3 \sin \theta_W + B_\mu \cos \theta_W \\ D_\mu &= \partial_\mu - i \frac{e}{\sqrt{2} \sin \theta_W} (W_\mu^+ T^+ + W_\mu^- T^-) \\ &\quad - i \frac{e}{\sin \theta_W \cos \theta_W} Z_\mu (T^3 - \sin^2 \theta_W Q) - ie A_\mu Q. \end{aligned}$$

This theory is often referred to as the Glashow-Weinberg-Salam theory. At the time this theory was suggested, the chiral nature of the weak interaction had already been known [35]. The particles that undergo both  $SU(2)$  and  $U(1)$  gauge transformations are left-chiral lepton and quark doublets

$$E_L = \begin{pmatrix} \nu_L \\ e_L \end{pmatrix}, \quad Q_L = \begin{pmatrix} u_L \\ d_L \end{pmatrix},$$

which have hypercharge  $Y = -\frac{1}{2}$  and  $Y = \frac{1}{6}$  respectively. The right-chiral fermions  $\nu_R$ ,  $e_R$ ,  $u_R$  and  $d_R$  are isospin singlets that undergo only  $U(1)$  transformations. These singlets have hypercharge identical to their electric charge  $Q$ , which means  $\nu_R$  is automatically excluded from any form of electroweak interaction. The electroweak sector of the Lagrangian is then

$$\begin{aligned} \mathcal{L}_{\text{EW}} &= \bar{E}_L (i\not{D}) E_L + \bar{e}_R (i\not{D}) e_R + \bar{Q}_L (i\not{D}) Q_L + \bar{u}_R (i\not{D}) u_R + \bar{d}_R (i\not{D}) d_R \\ &= \bar{E}_L (i\not{\partial}) E_L + \bar{e}_R (i\not{\partial}) e_R + \bar{Q}_L (i\not{\partial}) Q_L + \bar{u}_R (i\not{\partial}) u_R + \bar{d}_R (i\not{\partial}) d_R \\ &\quad + g \left( W_\mu^+ J_W^{\mu+} + W_\mu^- J_W^{\mu-} + Z_\mu^0 J_Z^\mu \right) + e A_\mu J_{\text{EM}}^\mu \end{aligned} \quad (1.49)$$

where the charged and neutral weak currents are

$$J_W^{\mu+} = \frac{1}{\sqrt{2}} (\bar{\nu}_L \gamma^\mu e_L + \bar{u}_L \gamma^\mu d_L) \quad (1.50)$$

$$J_W^{\mu-} = \frac{1}{\sqrt{2}} (\bar{e}_L \gamma^\mu \nu_L + \bar{d}_L \gamma^\mu u_L) \quad (1.51)$$

$$\begin{aligned} J_Z^\mu &= \frac{1}{\cos \theta_W} \left[ \bar{\nu}_L \gamma^\mu \left( \frac{1}{2} \right) \nu_L + \bar{e}_L \gamma^\mu \left( -\frac{1}{2} + \sin^2 \theta_W \right) e_L + \bar{e}_R \gamma^\mu (\sin^2 \theta_W) e_R \right. \\ &\quad + \bar{u}_L \gamma^\mu \left( \frac{1}{2} - \frac{2}{3} \sin^2 \theta_W \right) u_L + \bar{u}_R \gamma^\mu \left( -\frac{2}{3} \sin^2 \theta_W \right) u_R \\ &\quad \left. + \bar{d}_L \gamma^\mu \left( -\frac{1}{2} + \frac{1}{3} \sin^2 \theta_W \right) d_L + \bar{d}_R \gamma^\mu \left( \frac{1}{3} \sin^2 \theta_W \right) d_R \right] \end{aligned} \quad (1.52)$$

and the EM current is

$$J_{\text{EM}}^\mu = \bar{e} \gamma^\mu (-1) e + \bar{u} \gamma^\mu \left( \frac{2}{3} \right) u + \bar{d} \gamma^\mu \left( -\frac{1}{3} \right) d. \quad (1.53)$$

The EM current multiplied by the elementary charge  $e$  is exactly an example of eq. (1.19), with electric charge  $-e$ ,  $+\frac{2}{3}e$  and  $-\frac{1}{3}e$ . The currents in eqs. (1.50) and (1.51) show that  $W^+$  and  $W^-$  are the physical bosons that mediate weak interaction changing the flavor of the fermions. The neutral current in eq. (1.52) consists of terms analogous to eqs. (1.19) and (1.53), with a difference that this interaction acts as if left- and right-chiral fermions have different charge.

However, the chiral nature of the weak interaction makes it difficult to add mass terms to eq. (1.49) as in eq. (1.6), since left- and right-handed fermions transform differently. For example, the mass term for the electron

$$-m_e(\bar{e}e) = -m_e(\bar{e}_L e_R + \bar{e}_R e_L) \quad (1.54)$$

breaks the  $SU(2) \times U(1)$  gauge invariance. The Higgs field  $\phi$  resolves this problem nicely, under the assumption that  $\phi$  transforms as in eq. (1.41). Introducing Yukawa-type terms

$$\Delta\mathcal{L}_e = -\lambda_e \bar{E}_L \phi e_R + \text{h.c.} \quad (1.55)$$

$$\Delta\mathcal{L}_q = -\lambda_d \bar{Q}_L \phi d_R - \lambda_u \epsilon^{ab} \bar{Q}_{La} \phi_b^\dagger u_R + \text{h.c.} \quad (1.56)$$

which are invariant under  $SU(2) \times U(1)$  local gauge transformations, the mass terms naturally appear at the vacuum expectation value of  $\phi$ :

$$\Delta\mathcal{L}_e = -\frac{1}{\sqrt{2}} \lambda_e v (\bar{e}_L e_R + \bar{e}_R e_L) \quad (1.57)$$

$$\Delta\mathcal{L}_q = -\frac{1}{\sqrt{2}} \lambda_d v \bar{d}_L d_R - \frac{1}{\sqrt{2}} \lambda_u v \bar{u}_L u_R + \text{h.c.} \quad (1.58)$$

The higgs field terms in eq. (1.40) can be expanded near the vacuum expectation value  $v$ . Due to the local gauge invariance of the Glashow-Weinberg-Salam theory, the Higgs field  $\phi$  can be expressed as a fluctuation from the vacuum rotated by  $U(x) \in SU(2)$  at every point:

$$\phi(x) = U(x) \frac{1}{\sqrt{2}} \begin{pmatrix} 0 \\ v + h(x) \end{pmatrix} \quad (1.59)$$

such that the fluctuation  $h(x)$  is always real. Expanding and rearranging eq. (1.40), the Higgs field terms become

$$\begin{aligned} \mathcal{L}_{\text{Higgs}} = & \frac{1}{2} (\partial_\mu h) (\partial^\mu h) - \mu^2 h^2 - \sqrt{\lambda} \mu h^3 - \frac{\lambda}{4} h^4 \\ & + \left[ m_W^2 W^{\mu+} W_\mu^- + \frac{1}{2} m_Z^2 Z^\mu Z_\mu \right] \left( 1 + \frac{h}{v} \right)^2. \end{aligned}$$

The first two terms are exactly what appear in the Klein-Gordon Lagrangian in eq. (1.2), with mass  $m_h = \sqrt{2}\mu$ . The new real scalar field  $h(x)$ , being its own antiparticle, is the physical scalar boson known as the Higgs boson. The second line shows how the Higgs boson couples to the  $W$  and  $Z$  bosons, as well as their Proca mass terms as in eqs. (1.10) and (1.11).

### 1.1.5 Particle Contents of the Standard Model

The particles constituting the Standard Model are classified into four categories: quarks, leptons, gauge bosons and the Higgs boson.

- **Quarks:** consisting of six flavors, quarks are the constituents of baryons and mesons. In addition to the up-, down- and strange quarks that were first proposed, Glashow and Bjorken [36] introduced a fourth quark later named the *charm*, to account for the mechanism of neutral kaon decays suggested by Glashow, Iliopoulos and Maiani [37]. The existence of the charm quark was proven by the discovery of the  $J/\psi$  meson [38, 39], which is a bound state of  $c\bar{c}$ . Two additional quarks, bottom- and top quarks were introduced by Kobayashi and Maskawa [40], to account for the  $CP$ -violation, which is the intrinsic asymmetry between matter and antimatter. The existence of the bottom quark was proven by the discovery of the  $\Upsilon$  meson [41], which is a bound state of  $b\bar{b}$ . The top quark, being the heaviest particle in the SM, was discovered at the Tevatron in 1995 [42, 43].

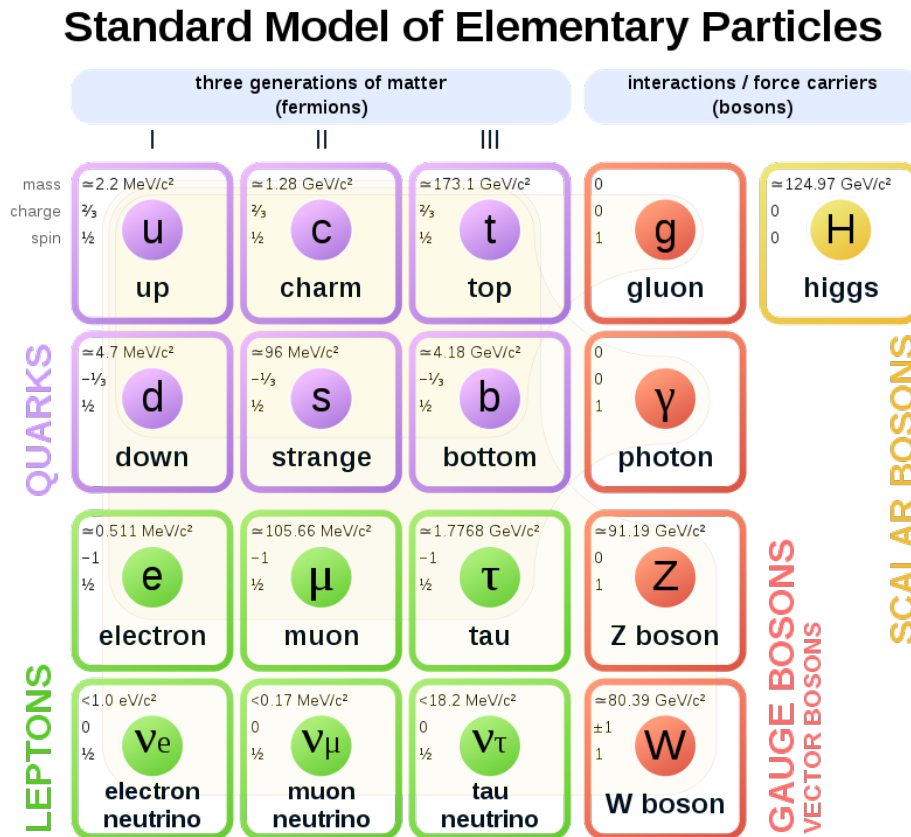


Figure 1.1: Particle contents of the Standard Model [51].

- Leptons:** while the electron was one of the first elementary particle to be found, its heavier version, muon was discovered in cosmic rays. In addition to these charged leptons, neutral leptons were proposed to account for the energy distribution of the  $\beta$ -decay of neutrons. These are the neutrinos, interacting only via weak interaction. The third charged lepton was found in anomalous signatures of  $e^+e^-$  collisions at the SPEAR, in 1975 [44]. The lepton sector is then summarized into three charged leptons and their neutrino counterparts, although the properties of the neutrinos are still under active investigations.
- Gauge bosons:** the photon,  $W$  boson,  $Z$  boson and gluons are the mediators of fundamental interactions. The  $W$  and  $Z$  bosons were found at the SPS in 1983 [45, 46]. The existence of gluons were proven by observation of three-prong jets in electron-positron colliders such as DORIS and PETRA [47, 48]. All of these gauge bosons are spin-1.
- Higgs boson:** being the only scalar boson in the SM, the Higgs boson is an essential part of the theory to account for the mass of  $W$  and  $Z$  bosons, as well as the fermions. Its existence was found at the LHC [49, 50], being one of the biggest achievements of the experiment.

All of these elementary particles are summarized in fig. 1.1.

## 1.2 Shortcomings of the Standard Model

Despite its great success in many experiments, there are hints that suggest there might be a more fundamental theory of physics than the Standard Model.

- **Arbitrary parameters in electroweak unification:** in the Glashow-Weinberg-Salam theory, there are three fundamental parameters  $e$ ,  $\theta_W$  and  $m_W$  which can be completely arbitrary. The reason these parameters have the experimentally observed values is unknown.
- **No unification of the electroweak and strong interactions:** although the electroweak (EW) and strong interactions are formulated in a similar manner, they are still different interactions, with different couplings without any evidence that they originated from the same coupling.
- **Mass of neutrinos:** since right-chiral neutrino never appears in eqs. (1.50) to (1.53), neutrinos are usually assumed massless in the SM. However, experiments observed ‘neutrino oscillations’, implying they do have small mass and their flavor eigenstates and mass eigenstate do not match. In the Glashow-Weinberg-Salam theory, a Yukawa term

$$\Delta\mathcal{L}_\nu = -\lambda_\nu \epsilon^{ab} \bar{E}_{La} \phi_b^\dagger \nu_R + \text{h.c.}$$

analogous to eqs. (1.55) and (1.56) can be included [20]. The coupling strength  $\lambda_\nu$  must be extremely small for compatibility with the neutrino mass, which has no apparent reason. Alternatively, neutrino might be a Majorana fermion where the right-chiral neutrino is just the right-chiral antineutrino [52]. This hypothesis predicts neutrinoless double  $\beta$ -decay and is under active investigations.

- **Mass of particles in general:** the SM successfully explained how the particles acquire mass - via Higgs mechanism. However, the SM does not explain why the masses should be the very values measured experimentally. For the SM gauge bosons, their masses are expressed in terms of the vacuum expectation value of the Higgs field and couplings of the gauge groups. For the fermions, the masses are expressed in terms of the vacuum expectation value and the Yukawa couplings. This merely replaces the mass with another empirical parameter and the reason why the masses of fermions with different generations are so different remains unknown.
- **Hierarchy problem:** in the Glashow-Weinberg-Salam theory, all particle masses are proportional to the vacuum expectation value of the Higgs field. As all the constituents have been discovered, the vacuum expectation value is known to be

$$v \approx 246 \text{ GeV.}$$

This is unnatural, since  $v$  is much smaller than  $10^{16}$  GeV where the fundamental interactions are believed to unify. If such unification scheme is to exist, this discrepancy requires extremely fine tuning of parameters to avoid divergences in computations of loop diagrams involving the Higgs boson.

- **Gravitation:** the SM does not say anything about gravitational interactions, as there is no completely proven quantum field theory of gravity yet.
- **Dark matter:** astronomical observations imply there is unknown matter that does not interact electromagnetically or current formulation of gravitational theories needs modification. The SM explains neither of them.

Names		spin-0	spin- $\frac{1}{2}$	$SU(3) \times SU(2) \times U(1)$
squarks and quarks ( $\times 3$ families)	$Q$	$(\tilde{u}_L, \tilde{d}_L)$	$(u_L, d_L)$	$(\mathbf{3}, \mathbf{2}, \frac{1}{6})$
	$\bar{u}$	$\tilde{u}_R^*$	$u_R^\dagger$	$(\bar{\mathbf{3}}, \mathbf{1}, -\frac{2}{3})$
	$\bar{d}$	$\tilde{d}_R^*$	$d_R^\dagger$	$(\bar{\mathbf{3}}, \mathbf{1}, \frac{1}{3})$
sleptons and leptons	$L$	$(\tilde{\nu}_L, \tilde{e}_L)$	$(\nu_L, e_L)$	$(\mathbf{1}, \mathbf{2}, -\frac{1}{2})$
	$\bar{\nu}$	$\tilde{\nu}_R^*$	$\nu_R^\dagger$	$(\mathbf{1}, \mathbf{1}, 0)$
	$\bar{e}$	$\tilde{e}_R^*$	$e_R^\dagger$	$(\mathbf{1}, \mathbf{1}, 1)$
Higgs and higgsinos	$H_u$	$(H_u^+, H_u^0)$	$(\tilde{H}_u^+, \tilde{H}_u^0)$	$(\mathbf{1}, \mathbf{2}, \frac{1}{2})$
	$H_d$	$(H_d^0, H_d^-)$	$(\tilde{H}_d^0, \tilde{H}_d^-)$	$(\mathbf{1}, \mathbf{2}, -\frac{1}{2})$

Table 1.1: Chiral multiplets of the Minimal Supersymmetric Standard Model and their SM partners [54].

Names	spin- $\frac{1}{2}$	spin-1	$SU(3) \times SU(2) \times U(1)$
gluino and gluon	$\tilde{g}$	$g$	$(\mathbf{8}, \mathbf{1}, 0)$
wino and $W$ bosons	$\tilde{W}^\pm, \tilde{W}^3$	$W^\pm, W^3$	$(\mathbf{1}, \mathbf{3}, 0)$
bino and $B$ boson	$\tilde{B}$	$B$	$(\mathbf{1}, \mathbf{1}, 0)$

Table 1.2: Gauginos in the Minimal Supersymmetric Standard Model and their SM partners [54].

- **Lepton Flavor Universality:** in the SM, all generations of leptons interact identically, except they have different masses. However, recent experimental results imply there might be a violation in this universality. This will be explained with more details in section 1.4.1.
- **Magnetic moment of muon:** the muon  $g - 2$  experiment has reported a strong evidence of deviation from the prediction of the SM [53] by measuring the magnetic moment of the muon. This suggests there might be unknown particles or processes contributing to the EM interaction of the muon.

### 1.3 Supersymmetry

One of the most remarkable candidates for the extension of the SM is supersymmetry, often referred to as SUSY. Supersymmetry introduces a broken symmetry<sup>3</sup> between fermions and bosons by assigning a *superpartner* to each SM particle. In supersymmetry, every SM fermion (spin- $\frac{1}{2}$ ) has a supersymmetric scalar boson (spin-0) counterpart called sfermion. The sfermions are called *squarks* or *sleptons* depending on their SM partners. Unlike in the SM, two Higgs doublets are needed and have spin- $\frac{1}{2}$  partners called *higgsinos*. These fields which have chiral structures are summarized in table 1.1. A notable property is that each SM particle and its superpartner have the same  $SU(3) \times SU(2) \times U(1)$  quantum numbers.

Likewise, each SM gauge boson has a supersymmetric partner called *gaugino*. The SM gluons have gluinos as their superpartners, while  $W$  bosons of the  $SU(2)$  group and the  $B$  boson of the  $U(1)$  have winos and bino. This is the Minimal Supersymmetric Standard Model (MSSM). The gauginos of the MSSM are listed in table 1.2.

<sup>3</sup>The fact there is no observed supersymmetric particle yet implies such particle must be very heavy.

One of the theoretical advantages of the supersymmetry is that the hierarchy problem is resolved. Each loop diagram involving the Higgs boson and a SM fermion can be canceled by a corresponding loop diagram with a sfermion. Likewise, a loop containing a SM gauge boson is can be canceled by a loop with a gaugino. With these properties, divergences in loop diagrams can be avoided without fine tuning of parameters.

Another advantage is that it enables the unification of the SM interactions at higher energies. In the Standard Model, the  $U(1)$ ,  $SU(2)$  and  $SU(3)$  gauge groups have different coupling constants. Extrapolating these running couplings to higher energy scales, the  $U(1)$  coupling increases while the  $SU(2)$  and  $SU(3)$  couplings decrease. This makes the couplings converge but not match at the same point, as shown in the upper plot in fig. 1.2. Grand Unified Theories predict these couplings originate from one coupling of a larger gauge group such as  $SU(5)$  [1]. If the couplings are extrapolated using the Minimal Supersymmetric Standard Model instead, they become identical at the scale of  $10^{16}$  GeV, as shown in the lower plot of fig. 1.2 [55].

Supersymmetry also includes candidates for dark matters. The  $R$ -parity is defined as

$$P_R = (-1)^{3(B-L)+2s} \quad (1.60)$$

where  $B$ ,  $L$  and  $s$  are the baryon number, lepton number and spin respectively. If this new quantum number is conserved, the Lightest Supersymmetric Particle (LSP) is stable [54]. The neutralinos ( $\tilde{\chi}^0$ ), which are mixed states of the gauginos and higgsinos, are the LSP in many scenarios.

The particular supersymmetric scenario that this work re-interprets is the pair production of top squarks ( $\hat{t}$ ) decaying via tau sleptons ( $\tilde{\tau}$ ), shown in fig. 1.3. The three-body decay of the top squark produces a tau slepton, a  $b$ -quark and a neutrino. The tau slepton decays into a tau lepton and a *gravitino* ( $\tilde{G}$ ) which is the LSP and the superpartner of the graviton. The top squarks and tau sleptons are often abbreviated to *stops* and *staus*.

## 1.4 Leptoquark

Leptoquarks (LQ) are hypothetical bosons carrying nonzero baryon and lepton numbers proposed in various extensions of the SM. They can be either scalar (spin-0) or vector (spin-1) bosons.

The  $SU(5)$  Grand Unified Theory proposed by Georgi and Glashow [1] is the simplest grand unification that embeds  $SU(3) \times SU(2) \times U(1)$ . In a different aspect, Pati and Salam suggested an  $SU(4)$  symmetry to unify the lepton and quark sectors of the SM, taking the lepton number as the ‘fourth color’ [2]. Both Georgi-Glashow model and Pati-Salam model can be embedded in a larger gauge group  $SO(10)$  [3]. In these models, leptoquarks are heavy gauge bosons of the larger gauge groups. Technicolor theories [4, 5] and composite models [56, 57] also predict leptoquarks. In supersymmetric theories where the  $R$ -parity defined in eq. (1.60) is not conserved, squarks have the properties of the scalar LQ [58].

In these theories, there are common properties that the leptoquarks must have. The leptoquarks carry color charges, making them color triplets. This automatically allows the leptoquarks to interact via strong interaction. Leptoquarks also carry electroweak hypercharge and thus can interact via charged or neutral EW bosons. As they couple to lepton and quark at the same time, they can turn a quark into lepton or vice versa, mediating processes that are highly suppressed in the SM. The absence of observation of the leptoquarks implies they must be very heavy.

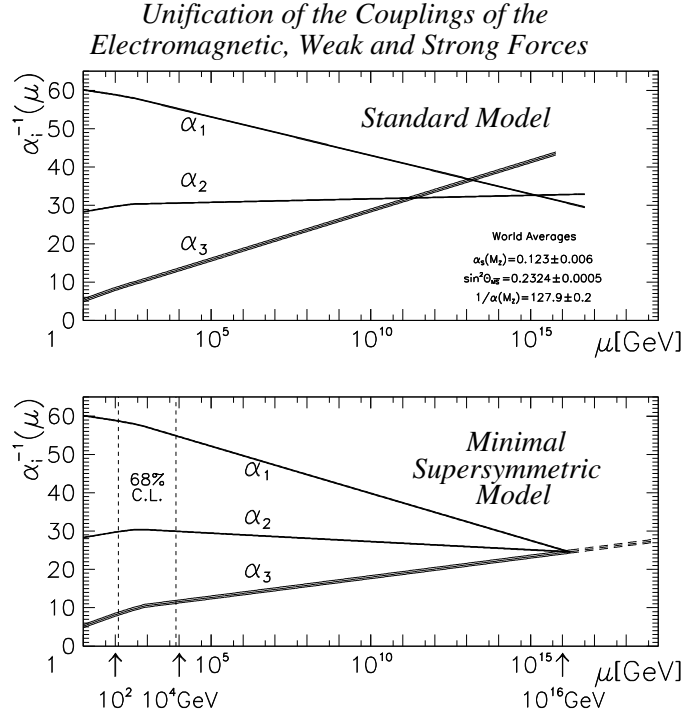


Figure 1.2: Extrapolation of the couplings of the  $U(1)$  ( $\alpha_1 = \frac{5}{3} \frac{\alpha}{\cos^2 \theta_W}$ ),  $SU(2)$  ( $\alpha_2 = \frac{g^2}{4\pi} = \frac{\alpha}{\sin^2 \theta_W}$ ) and  $SU(3)$  ( $\alpha_3 = \frac{g_s^2}{4\pi}$ ) gauge groups to higher energy scales. The upper plot shows the Standard Model prediction where the three couplings do not meet at one point. The lower plot shows the prediction of the Minimal Supersymmetric Standard Model, where the three couplings meet at the scale of  $10^{16}$  GeV [55].

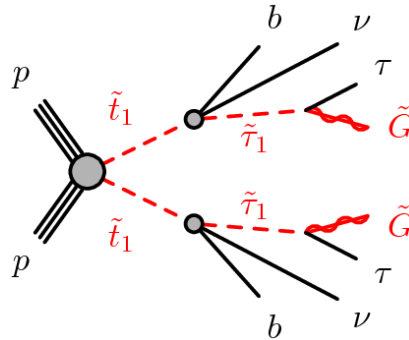


Figure 1.3: Pair production of top squarks ( $\tilde{t}$ ) in a proton-proton collision followed by decays via tau sleptons ( $\tilde{\tau}$ ).

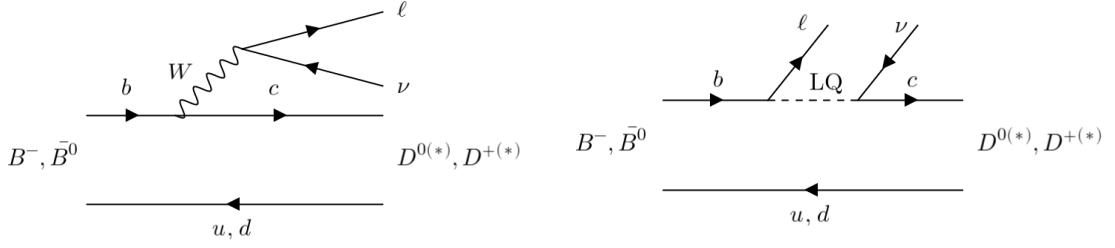


Figure 1.4: Diagrams of  $B$  mesons decaying into  $D$  mesons in the SM (left) and a leptoquark scenario (right).

Focusing on the coupling of leptoquarks with the SM fermions, the effective Lagrangians of the leptoquarks can be constructed according to their gauge quantum numbers [14]. In section 1.4.2, the classification and naming schemes are explained.

Recent results in the physics of  $B$  mesons support the possibility of leptoquark scenarios. The experimental results and phenomenology of the leptoquarks are explained in section 1.4.1.

### 1.4.1 Hints from B-anomalies

In the Standard Model, there is no difference between different generations of leptons in the way they interact. The only difference is the mass, which is purely an empirical parameter in the SM. This principle is called the ‘Lepton Flavor Universality (LFU)’. However, recent measurements in rare decays of  $B$  mesons are reporting hints of LFU violation. One example is the transition of the  $b$  quark via charged currents  $b \rightarrow c l \nu$ . In the SM, the leading order process is the decay via  $W$  boson. To test the LFU, the ratio

$$R(D^{(*)}) = \frac{B(B \rightarrow D^{(*)} \tau \nu)_{\text{exp}}}{B(B \rightarrow D^{(*)} l \nu)_{\text{exp}}} \quad (1.61)$$

is checked, where  $l$  denotes the electron and muon. As shown in fig. 1.5, experimental results deviate from the SM prediction [6–13]. This discrepancy can be explained if there are tree-level processes involving leptoquarks, as shown in fig. 1.4.

Another example is the transition of the  $b$  quark via neutral currents  $b \rightarrow s l l$ . This transition is responsible for rare decay modes  $B \rightarrow K l l$ . Since there is no flavor-changing neutral current (FCNC) at tree level in the SM, such processes can occur only via higher order diagrams, such as the left diagram in fig. 1.6. Due to the small decay rate, these processes are sensitive to potential contributions from physics beyond the Standard Model. For example, if there exist leptoquarks that couple to multiple generations of SM fermions, tree level processes like the right diagram in fig. 1.6 are possible.

Measuring the decay rates allows for the test for LFU, by calculating the rate

$$R(K^{(*)}) = \frac{B(B \rightarrow K^{(*)} \mu \mu)_{\text{exp}}}{B(B \rightarrow K^{(*)} e e)_{\text{exp}}}. \quad (1.62)$$

Measurements in  $R(K^{(*)})$  have shown a hint of its violation [11–13], the most recent result showing  $3.1\sigma$  of significance.

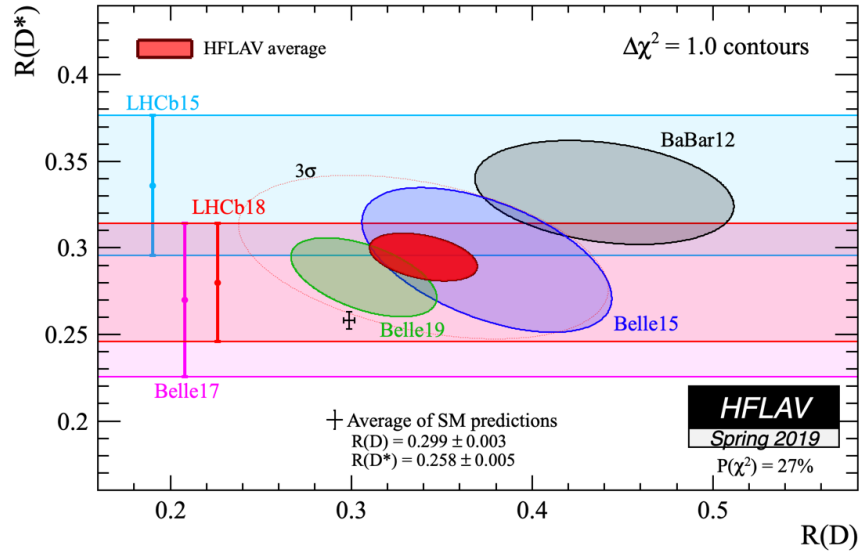


Figure 1.5: Combined plot of  $R(D^{(*)})$  measurements by BaBar, Belle and LHCb collaborations [59].

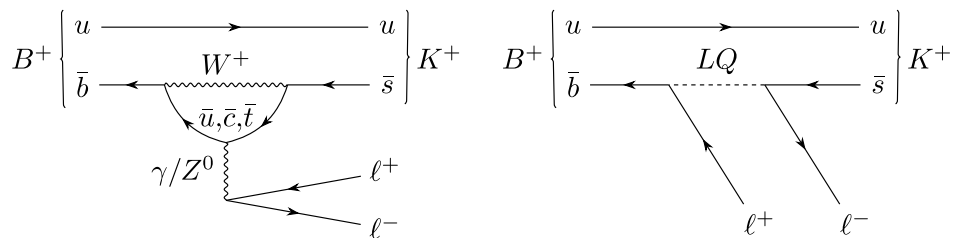


Figure 1.6: Diagrams of charged  $B$  mesons decaying into  $K$  mesons in the SM (left) and a leptptoquark scenario (right) [13].

Name	Spin	$F = 3B + L$	$SU(3)_C$	$SU(2)_W$	$U(1)_Y$	Allowed coupling	$Q = I^3 + Y$
$S_1$	0	-2	$\bar{\mathbf{3}}$	1	$\frac{1}{3}$	$\bar{q}_L^c l_L$ or $\bar{u}_R^c e_R$	$\frac{1}{3}$
$\tilde{S}_1$	0	-2	$\bar{\mathbf{3}}$	1	$\frac{4}{3}$	$\bar{d}_R^c e_R$	$\frac{4}{3}$
$S_3$	0	-2	$\bar{\mathbf{3}}$	3	$\frac{1}{3}$	$\bar{q}_L^c l_L$	$\frac{4}{3}, \frac{1}{3}, -\frac{2}{3}$
$V_2$	1	-2	$\bar{\mathbf{3}}$	2	$\frac{5}{6}$	$\bar{q}_L^c \gamma^\mu e_R$ or $\bar{d}_R^c \gamma^\mu l_L$	$\frac{4}{3}, \frac{1}{3}$
$\tilde{V}_2$	1	-2	$\bar{\mathbf{3}}$	2	$-\frac{1}{6}$	$\bar{u}_R^c \gamma^\mu l_L$	$\frac{1}{3}, -\frac{2}{3}$
$R_2$	0	0	$\mathbf{3}$	2	$\frac{7}{6}$	$\bar{q}_L e_R$ or $\bar{u}_R l_L$	$\frac{5}{3}, \frac{2}{3}$
$\tilde{R}_2$	0	0	$\mathbf{3}$	2	$\frac{1}{6}$	$\bar{d}_R l_L$	$\frac{2}{3}, -\frac{1}{3}$
$U_1$	1	0	$\mathbf{3}$	1	$\frac{2}{3}$	$\bar{q}_L \gamma^\mu l_L$ or $\bar{d}_R \gamma^\mu e_R$	$\frac{2}{3}$
$\tilde{U}_1$	1	0	$\mathbf{3}$	1	$\frac{5}{3}$	$\bar{u}_R \gamma^\mu e_R$	$\frac{1}{3}$
$U_3$	1	0	$\mathbf{3}$	3	$\frac{2}{3}$	$\bar{q}_L \gamma^\mu l_L$	$\frac{5}{3}, \frac{2}{3}, -\frac{1}{3}$

Table 1.3: Quantum numbers of scalar and vector leptoquarks with  $SU(3) \times SU(2) \times U(1)$  invariant couplings to quark-lepton pairs [14].

### 1.4.2 Classification of Leptoquarks

Buchmüller-Rückl-Wyler model [14] classifies leptoquarks by their gauge quantum numbers, as shown in table 1.3. All leptoquarks are color triplets which interact via QCD. One way to classify leptoquarks is the fermion number, defined as  $F = 3B + L$ , where  $B$  is the baryon number and  $L$  is the lepton number. Leptoquarks with  $F = -2$  decay into an antiquark and antilepton. Such leptoquarks are anticolor triplets, denoted by  $\bar{\mathbf{3}}$  in table 1.3. Leptoquarks with  $F = 0$  decay into a quark and antilepton. These leptoquarks are color triplets and denoted by  $\mathbf{3}$  in the  $SU(3)_C$  column of table 1.3. Leptoquarks can be either spin-0 (scalar) or spin-1 (vector). Scalar and vector LQs are denoted by  $S$  and  $V$  respectively in the case  $F = -2$ , while  $R$  and  $U$  in the case  $F = 0$ . In terms of  $SU(2)_W$  dimensionality, the LQs can be a singlet, doublet or triplet. This determines the subscript in the LQ name. The singlet leptoquarks do not interact via charged weak bosons. This thesis addresses the  $U_1$  vector leptoquark, which provides a viable explanation both for  $R(D^{(*)})$  and  $R(K^{(*)})$  anomalies [16, 17, 60].

### 1.4.3 Production Mechanism of Leptoquarks at Hadron Colliders

The dominant processes in pair production of leptoquarks at hadron colliders are gluon-gluon fusion (fig. 1.7a) and quark-antiquark annihilation (left of fig. 1.7b). Lepton exchange (right of fig. 1.7b) is negligible in most cases, as long as the coupling of the LQ with the SM fermion is not large [61].

The production cross section of leptoquarks is discussed in section 5.1, both for scalar and vector cases.

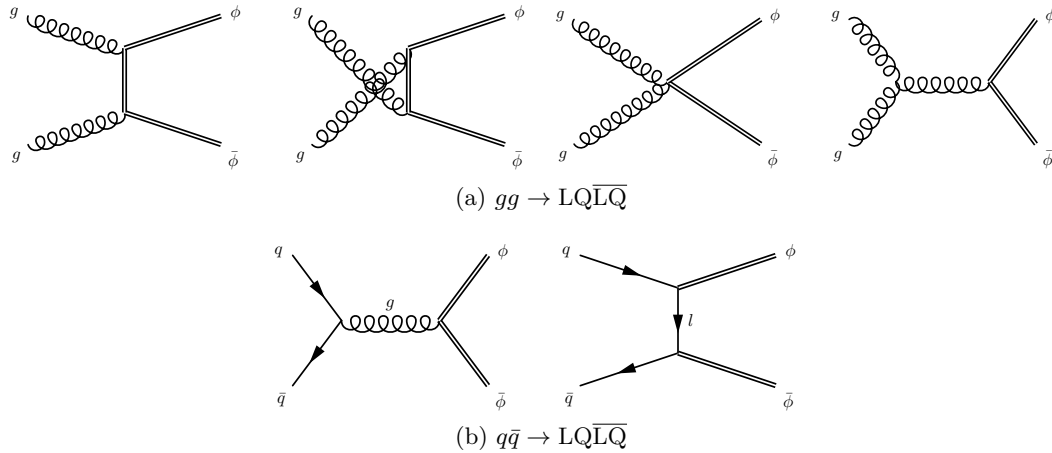


Figure 1.7: Pair-production mechanism of leptoquarks at the LHC [61].

#### 1.4.4 Simplified Scalar Leptoquark

The generic Lagrangian of a scalar leptoquark is similar to eq. (1.3):

$$\mathcal{L} = (D_\mu \Phi)^\dagger (D^\mu \Phi) - m_{LQ}^2 |\Phi|^2 + \mathcal{L}_{\text{int}}, \quad (1.63)$$

but replacing  $\partial_\mu$  with the SM covariant derivative  $D_\mu$  and adding Yukawa terms  $\mathcal{L}_{\text{int}}$  similar to eqs. (1.55) and (1.56). Neglecting difference between particles and antiparticles, it is possible to construct a simplified scalar leptoquark model [62] in which all kinds of Yukawa couplings are possible. In the simplified model, the scalar leptoquarks are assumed to interact only via strong interaction, where the covariant derivative becomes eq. (1.37). The simplified model contains up- ( $Q = +\frac{2}{3}e$ ) and down- ( $Q = -\frac{1}{3}e$ ) type leptoquarks, with Yukawa terms

$$\begin{aligned} \mathcal{L}_{\text{int}}^{\text{u}} &= \lambda_l (\sqrt{\eta_L} \bar{d}_R l_L + \sqrt{\eta_R} \bar{d}_L l_R) \Phi + \lambda_\nu \bar{d}_R \nu_L \Phi + \text{h.c.} \\ \mathcal{L}_{\text{int}}^{\text{d}} &= \lambda_l (\sqrt{\eta_L} \bar{u}_R l_L^c + \sqrt{\eta_R} \bar{u}_L l_R^c) \Phi + \lambda_\nu \bar{d}_R \nu_L^c \Phi + \text{h.c.} \end{aligned}$$

respectively. The fields  $u_{L,R}$  and  $d_{L,R}$  are chiral quarks, while  $l_{L,R}$  and  $\nu_L$  are charged leptons and neutrinos. For the down-type LQ,  $l_{L,R}^c$  and  $\nu_L^c$  denote charge conjugates of the charged leptons and neutrinos, namely their antiparticles. Therefore, the up- and down-type leptoquarks in this simplified model have  $F = 0$  and  $F = 2$ , the latter case being similar to antiparticles of leptoquarks with  $F = -2$  in table 1.3. Restricting the coupling of the LQ to the third-generation SM fermions, the up-type LQ decays into  $(b, \tau)$  or  $(t, \nu)$ , while the down-type LQ decays into  $(b, \nu)$  or  $(t, \tau)$ . This is illustrated in fig. 1.8. Comparing fig. 1.8 and fig. 1.3, the similarities in their final states show that the two scenarios can be covered in one analysis. The ATLAS collaboration has searched for them in Run-2 of the LHC [63, 64].

The coupling strength to charged leptons and neutrinos can be parameterized as

$$\begin{aligned} \lambda_l &= \lambda \sqrt{\beta} \\ \lambda_\nu &= \lambda \sqrt{1 - \beta} \end{aligned} \quad (1.64)$$

where  $\lambda$  represents the global Yukawa coupling strength and  $\beta$  determines the relative coupling strength with charged leptons and neutrinos. The scalar LQ search in this thesis reinterprets assumed  $\beta = 0.5$  such that the coupling strength with charged leptons and neutrinos are the same. Conventionally, it has been assumed that  $\lambda = 0.3$  in searches for pair production of leptoquarks. This parameter affects the  $t$ -channel diagram with lepton exchange (the right diagram of fig. 1.7b). However, as discussed in section 1.4.3, the lepton

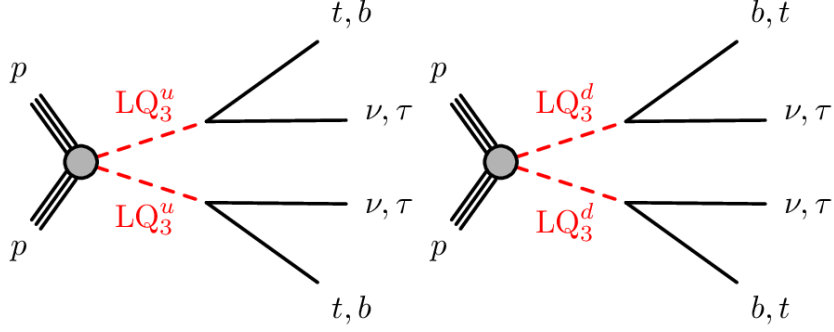


Figure 1.8: Pair production of up-type (left) and down-type (right) leptoquarks in a proton-proton collision followed by decays into third-generation SM fermions [63].

exchange diagram becomes negligible with this choice of value. The parameters  $\eta_L$  and  $\eta_R$  determine the chiral property of the leptoquarks. In the scalar LQ search, it was assumed that  $\eta_L = 1$  and  $\eta_R = 0$ .

Using Run-2 data taken in 2015 and 2016, ATLAS excluded both up- and down-type third-generation scalar leptoquarks up to 800 GeV for  $\beta = 0.5$  [63]. With the full Run-2 data taken from 2015 to 2018 and a new optimization of analysis, the exclusion limit was extended up to 1.25 TeV [64].

#### 1.4.5 The $U_1$ Vector Leptoquark

The Lagrangian of the  $U_1$  leptoquark is

$$\begin{aligned} \mathcal{L}_{U_1} = & -\frac{1}{2}U_{1\mu\nu}^\dagger U_1^{\mu\nu} + m_{U_1}^2 U_{1\mu}^\dagger U_1^\mu - ig_s(1 - \kappa_U)U_{1\mu}^\dagger T^a U_{1\nu} G^{a\mu\nu} \\ & - ig_Y \frac{2}{3}(1 - \tilde{\kappa}_U)U_{1\mu}^\dagger U_{1\nu} B^{\mu\nu} + \frac{g_U}{\sqrt{2}}[U_1^\mu (\beta_L^{ij} \bar{q}_L^i \gamma_\mu l_L^j + \beta_R^{ij} \bar{d}_R^i \gamma_\mu e_R^j) + \text{h.c.}] \end{aligned} \quad (1.65)$$

where the strength tensor of the vector LQ is generically defined as  $U_{1\mu\nu} = D_\mu U_{1\nu} - D_\nu U_{1\mu}$  [15, 16, 60, 65]. The first two terms are similar to eq. (1.11), but replacing  $\partial_\mu$  in the strength tensor with the SM covariant derivative. As  $U_1$  has hypercharge  $Y = \frac{2}{3}$ , its covariant derivative becomes  $D_\mu = \partial_\mu - ig_Y \frac{2}{3} B_\mu - ig_s \frac{\lambda^a}{2} G_\mu^a$  [60, 66]. The parameters  $\kappa_U$  and  $\tilde{\kappa}_U$  determine the nature of the LQ. The first case where  $\kappa_U = \tilde{\kappa}_U = 0$  is often called the ‘Yang-Mills’ case, which means the LQ itself is a heavy gauge boson. Another case where  $\kappa_U = \tilde{\kappa}_U = 1$  is the ‘minimal coupling’ case, where eq. (1.65) gives the minimal vector boson coupling. This thesis covers both cases as  $\kappa_U$  significantly affects the production cross section of the LQ and kinematics of the decay products. The last terms in eq. (1.65) are analogous to the charged weak current terms in eqs. (1.49) to (1.51), with a difference that the leptoquark  $U_1$  couples to a lepton and a quark simultaneously. The quark doublets and lepton doublets are defined as

$$q_L^i = \begin{pmatrix} V_{ji}^* u_L^j \\ d_L^i \end{pmatrix}, \quad l_L^j = \begin{pmatrix} \nu_L^j \\ e_L^j \end{pmatrix}$$

where  $V_{ji}$  are the CKM matrix elements. The fact that  $U_1$  couples to a lepton doublet implies that LQ couples to charged lepton and neutrino with equal strength, which is equivalent to choosing  $\beta = 0.5$  in the simplified scalar LQ model. This benchmark model suppresses certain

generations of couplings such that the coefficients  $\beta_L^{ij}$  and  $\beta_R^{ij}$  form matrices

$$\beta_L = \begin{pmatrix} 0 & 0 & \beta_L^{13} \\ 0 & 0 & \beta_L^{23} \\ 0 & \beta_L^{32} & \beta_L^{33} \end{pmatrix}, \quad \beta_R = \begin{pmatrix} 0 & 0 & 0 \\ 0 & 0 & 0 \\ 0 & 0 & \beta_R^{33} \end{pmatrix}. \quad (1.66)$$

As this analysis addresses the third-generation LQ,  $\beta_L^{33}$  is set to 1 and all other elements of  $\beta_L^{ij}$  are set to 0. The vector LQ is assumed chiral such that the vector LQ couples only to left-chiral fermions, therefore  $\beta_R^{33}$  is also set to 0. The global coupling strength  $g_U$  is equivalent to  $\lambda$  in the simplified scalar LQ model. Although it has been common to assume  $\lambda = 0.3$  in the scalar LQ searches,  $g_U = 3.0$  is chosen such that other heavy gauge bosons ( $g'$  and  $Z'$ ) appearing in the vector LQ model are suppressed [15]. The CMS collaboration has excluded the  $U_1$  vector LQ up to 1.41 TeV in the minimal coupling case and 1.73 TeV in the Yang-Mills case for  $g_U = 2.5$ , combining single and pair production searches [67].

## 2.1 The Large Hadron Collider

The Large Hadron Collider (LHC) is a hadron-hadron collider located near Geneva, operated by CERN. The LHC collides proton beams or heavy ion beams such as lead. Reusing the tunnel built for the Large Electron-Positron Collider (LEP), the collider has a circumference of 27 km, being the largest particle collider ever as of 2021. Targeted at the TeV scale where the electroweak symmetry breaking takes place, the LHC has successfully carried out precise tests of the Standard Model and the discovery of the Higgs boson. In exploring the frontier of particle physics, typically two aspects of challenges are faced.

The first aspect is the energy scale. To reach the mass scale of unknown particles, it is essential to reach as high a center-of-mass energy as possible. One advantage that circular colliders like LHC have over linear accelerators is that the particle beams can be used again and again. However, retaining the circular beam entails technical difficulties, since bending particle beams at such high energy requires extremely strong superconducting magnets. The circular beams also lose energy through synchrotron radiation. For a particle with electric charge  $e$  moving in a circular trajectory with radius  $\rho$ , the energy loss per turn is [19, 68]

$$\Delta E = \frac{4\pi}{3} \frac{e^2}{\rho} \beta^3 \gamma^4 \quad (2.1)$$

where  $\beta = v/c$  and  $\gamma = 1/\sqrt{1-\beta^2}$ . Noting that  $E = \gamma mc^2$  and  $\beta \approx 1$  for relativistic particles, eq. (2.1) becomes

$$\Delta E \approx \frac{4\pi}{3} \frac{e^2 E^4}{\rho c^8} \frac{1}{m^4}. \quad (2.2)$$

Therefore, an electron loses  $10^{13}$  times more energy than a proton when accelerated to the same energy. This is the reason the LHC can reach much a higher energy than the LEP could do, despite using the same tunnel.

Another aspect is the luminosity. The event rate of a physical process can be expressed as  $\sigma(\sqrt{s}) \times \mathcal{L}$ , where  $\sigma(\sqrt{s})$  is the cross section of the process at the center-of-mass energy  $\sqrt{s}$  and  $\mathcal{L}$  is the luminosity. Usually the processes to be searched for have very small cross section and therefore increasing the luminosity is a key part in accumulating sufficient statistics.

The LHC does not accelerate protons from the beginning. Instead, many older accelerators that have retired from the energy frontier are used as boosters for the LHC. The protons from

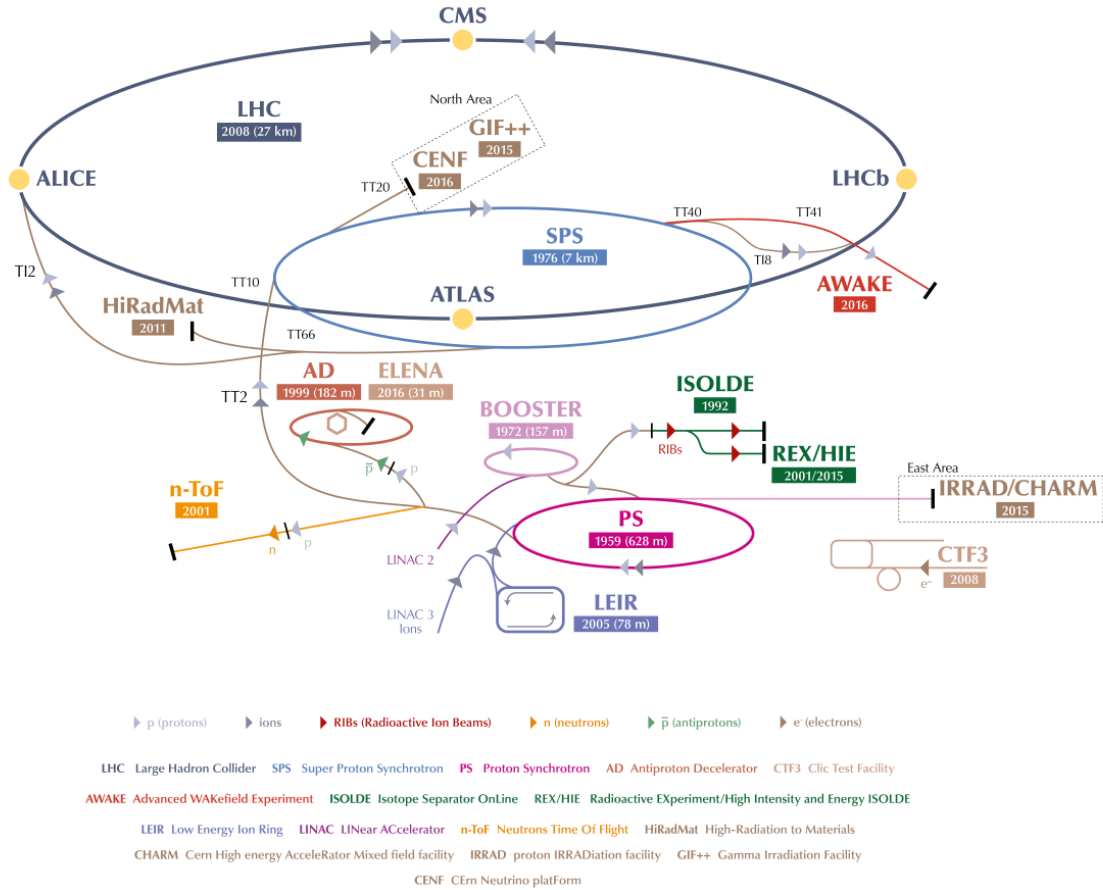


Figure 2.1: The CERN accelerator chain including the LHC [69].

the source are accelerated using a linear accelerator, up to the energy of around 50 MeV. The PS Booster accelerates these protons up to 1.4 GeV, before delivering them to the Proton Synchrotron (PS) which is the oldest operating synchrotron at CERN. At this step, protons reach the energy of 26 GeV. The Super Proton Synchrotron (SPS), known for the discovery of  $W$  and  $Z$  bosons, accelerates the protons to 450 GeV. This chain of acceleration is shown in fig. 2.1, with an overview of the CERN accelerator complex, including the LHC.

The first phase of the LHC operation, called ‘Run 1’, was from 2010 to 2012. Having started at the center-of-mass energy  $\sqrt{s} = 7$  TeV, the energy was ramped up to  $\sqrt{s} = 8$  TeV. The Higgs boson was discovered using part of the data taken in this phase.

The second phase, ‘Run 2’, was from 2015 to 2018. Operated at  $\sqrt{s} = 13$  TeV with higher luminosity, the LHC was improved up to the level such that even events involving the Higgs boson are backgrounds in many analyses. This thesis uses the full Run-2 dataset with an integrated luminosity of  $139 \text{ fb}^{-1}$ .

The next phase, ‘Run 3’, will start in 2022 with a target center-of-mass energy of  $\sqrt{s} = 14$  TeV.

## 2.2 The ATLAS Detector

The ATLAS (A Toroidal LHC ApparatuS) detector [70] is a multi-purpose detector located at the Interaction Point 1 (IP1) of the LHC. In ATLAS, a right-handed Cartesian coordinate system is used, where the  $z$ -axis is along the beam and the  $x - y$  plane is perpendicular to

the beam. The  $x$ -axis points from the interaction point to the center of the LHC ring and the  $y$ -axis points upwards. Additionally, the azimuthal angle  $\phi$  is measured around the  $z$ -axis, starting from the positive  $x$ -axis. The polar angle  $\theta$  is measured from the positive  $z$ -axis. One convention in parametrizing the polar angle is the pseudorapidity

$$\eta \equiv -\ln \left( \tan \frac{\theta}{2} \right) = \frac{1}{2} \ln \left( \frac{|\vec{p}| + p_z}{|\vec{p}| - p_z} \right) \quad (2.3)$$

which converges to rapidity

$$Y \equiv \frac{1}{2} \ln \left( \frac{E + p_z}{E - p_z} \right). \quad (2.4)$$

in the relativistic limit. The angular distance is defined as

$$\Delta R = \sqrt{(\Delta\eta)^2 + (\Delta\phi)^2} \quad (2.5)$$

The ATLAS detector has a cylindrical structure, consisting of many different layers specialized for different purposes.

- **Inner Detector (ID):** since particles are produced and decay near the interaction point, high precision is required in identification of the vertices. Therefore the innermost part of the ATLAS detector is designed to precisely measure the position of charged particles. Furthermore, by applying a magnetic field to charged particles, their momentum can be measured from the trajectories. For ATLAS, a solenoid magnet surrounds the inner detector to produce a magnetic field in the axial direction. An important point is that the particles should not lose too much energy in the inner detector, otherwise this affects the energy measured by the calorimeter system. Using semiconductors like silicon, this problem can be avoided, as only a small amount of energy is needed to excite electrons and thus to create a measurable current in semiconducting materials. The silicon pixel detector and silicon strip detector (SCT) record positions of the particles with high precision. The transition radiation tracker (TRT) provides further information on the type of the particle that passed through. The inner detector covers the range  $|\eta| < 2.5$  and provides electron identification in the range  $|\eta| < 2.0$ .
- **Calorimeters:** the purpose of the calorimeter system is to measure the energy of particles and trigger events. The inner layer of this part consists of lead absorber plates and liquid argon (LAr) used as the active material. In this layer, electrons dissipate energy through *Bremsstrahlung* ('braking radiation'), followed by pair creation of an electron and a positron from the photon. Electrons and photons are 'stopped' by the chain of these processes. Although muons have long enough lifetime to reach this layer, they are not stopped as their bremsstrahlung is negligible compared to electrons. The electromagnetic end-cap (EMEC), hadronic end-cap (HEC) calorimeters and forward calorimeter (FCal) also use liquid argon as the active material, covering regions with high pseudorapidity. The outer layer uses steel as the absorber and scintillator tiles as the active material. This layer is designed to measure the energy of hadrons by cascades of hadronic collisions.

In total, the calorimeter system covers the range  $|\eta| < 4.9$ .

- **Muon Spectrometers:** the outermost part of the ATLAS detector consists of muon spectrometers which measure position and momentum of muons.

The barrel muon system has three concentric layers which consist of monitored drift tubes (MDT) and resistive plate chambers (RPC). The MDT perform high-precision

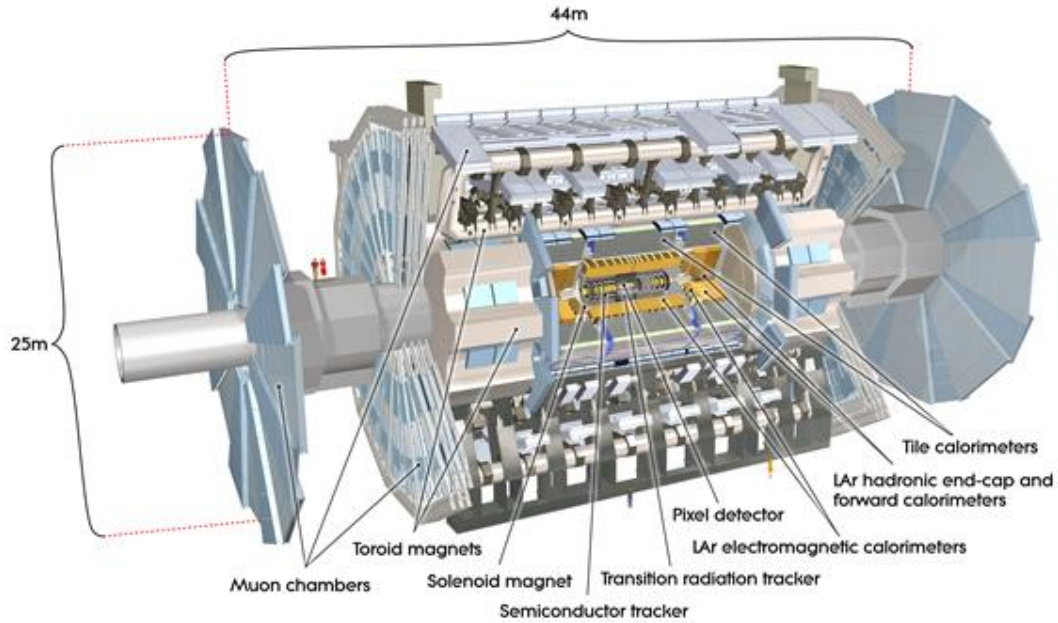


Figure 2.2: Overview of the ATLAS detector [71].

muon tracking, while the RPC provide muon triggers. The end-cap muon system consists of thin gap chambers (TGC) and MDT, where the TGC provide muon triggers. In the forward region close to the beam line, cathode strip chambers (CSC) provide muon tracking. The muon system in total covers the region  $|\eta| < 2.7$  and can trigger on events where a muon within  $|\eta| < 2.4$  is reconstructed by the online algorithms.

- **Magnet System:** the central solenoid surrounding the inner detector produces a magnetic field of 2 T in the axial direction. This enables the inner detector to measure momentum of charged particles. The barrel toroid consisting of eight coils produces a magnetic field of 4 T in azimuthal direction. Two end-cap toroids, each consisting of eight coils, also generate an azimuthal magnetic field of 4 T in the end-cap region. These toroids enable the muon system to measure the momentum of muons.

The configuration of the ATLAS detector is shown in fig. 2.2.

## 2.3 ATLAS Data Taking

At collision points of the LHC, proton bunches collide around 40 million times per second. In each collision of proton bunches, there are around 30 simultaneous proton-proton collisions on average. These concurrent collisions are called *pileups*. Combining these numbers, there are around  $10^9$  proton-proton collisions per second at the luminosity of  $10^{34} \text{ cm}^{-2}\text{s}^{-1}$ . However, most of the collisions do not contain hard scattering processes of interest. Out of the 40 million bunch-crossings happening every second, the trigger system selects and records relevant collision events. In Run-2, ATLAS uses two levels of triggers that make a real-time selection of events to be recorded [72].

The Level-1 (L1) trigger consists of hardware-based systems which make a coarse selection based on information from calorimeters and muon systems. L1Calo uses calorimeter information of electrons, photons and jets, while L1Muon is triggered by muons passing the RPC of

the barrel and TGC of the end-cap. L1Topo combines information from L1Calo and L1Muon into variables that are used in further L1 selections. After these processes, the event rate is reduced to around 100 kHz.

The High-Level Trigger (HLT) is a software-based system. Combined with offline reconstruction tools, the HLT also provides reconstruction of particles which are categorized in section 2.4. After the HLT, the average event rate is reduced to around 1 kHz.

## 2.4 Particle Reconstruction

The physical objects that the ATLAS detector can identify are summarized into the following categories.

- **Electrons and photons:** in general, the energy of electrons and photons ( $e/\gamma$ ) can be measured by the EM calorimeters. Electrons additionally leave a track in the inner detector such that their momentum can be measured. The electrons are then reconstructed by matching electron candidates from the energy deposit in the EM calorimeters to the ID tracks [73]. In this work, electrons and photons are not in the desired final states. However, electrons are used for a veto requiring zero light leptons in the final state. The electron candidates are required to fulfill *Loose* [74] identification criteria, with impact parameter  $z_0 < 5$  mm,  $p_T > 10$  GeV and  $|\eta| < 2.47$ .
- **Muons:** As muons leave no energy in the calorimeter system, inner detectors and muon spectrometers measure and identify muons. The muons are reconstructed if the tracks in the ID and muon spectrometers are matched [75]. In this work, muons are not in the desired final states. However, like electrons, muons are used for the veto that requires zero light leptons in the final state. Muon candidates are required to fulfill *Medium* identification criteria, with impact parameter  $z_0 < 5$  mm,  $p_T > 10$  GeV and  $|\eta| < 2.7$ .
- **Hadronic jets:** due to quark confinement, quarks *hadronize*. The quarks also emit gluons (*parton shower*), which produce further quark-antiquark pairs causing multiple hadronization processes. In the end, these particles form a cone-shaped cluster called *jet*. The jets are reconstructed using the anti- $k_T$  algorithm [76] with distance parameter  $R = 0.4$ . Jet candidates are required to have  $p_T > 20$  GeV and  $|\eta| < 2.8$ , with *Tight* selection criteria [77]. To remove jets from pileup, a jet-vertex-tagger (JVT) [78] is used. Jets with  $p_T < 60$  GeV and  $|\eta| < 2.4$  are rejected if the JVT score is less than 0.5.

Since hadrons containing  $b$ -quarks are relatively long-lived despite their mass, decays of such hadrons usually form a secondary vertex. By identifying the secondary vertices, it is possible to tag  $b$ -hadrons with sufficiently high probability. As this work requires  $b$ -tagged jets in final states, the DL1r  $b$ -tagger [79] is used. Choosing `FixedCutBEff_77` criteria,  $b$ -jets are identified with an efficiency of around 77%.

- **Tau leptons:** due to its short lifetime, the tau lepton decays before leaving any track in the detector. Therefore, the existence of tau leptons must be inferred indirectly. Tau leptons can decay either leptonically (35%) or hadronically (65%). Leptonically decaying tau leptons are observed as muons or electrons, while hadronically decaying tau leptons are observed as hadronic jets with a secondary vertex. As this work requires a hadronically decaying tau lepton in the final state, tau leptons are reconstructed from anti- $k_T$  jets [80] with distance parameter  $R = 0.4$ ,  $p_T > 10$  GeV and  $|\eta| < 2.5$  [81, 82]. Tau candidates are required to have  $p_T > 20$  GeV and lie outside the region  $1.37 < |\eta| < 1.52$  which is between the barrel and end-cap calorimeters. For the

identification of hadronically decaying tau leptons, a recurrent neural network (RNN) algorithm [83] is used, with *Medium* identification criteria.

- **Missing energy:** when there are invisible particles in the final state, the transverse momentum of all particles from one event do not cancel out. By convention, the negative sum of transverse momenta of the detected particles is denoted by  $\mathbf{E}_T^{\text{miss}}$ . The magnitude of this quantity is called *missing transverse energy*, denoted by  $E_T^{\text{miss}}$  or  $\cancel{E}_T$ . As mismeasurements of the objects can also lead to nonzero  $E_T^{\text{miss}}$ , this also requires a dedicated identification algorithm. One typical example of the invisible particles is the neutrino. Some theories beyond the Standard Model, like SUSY, also predict invisible particles. Therefore, large  $E_T^{\text{miss}}$  is a good criterion to search for new particles or phenomena.

### 3.1 ATLAS Data

The proton-proton collision data used in this work was taken by the ATLAS detector between 2015 and 2018, at a center-of-mass energy of  $\sqrt{s} = 13$  TeV. However, not all of the data can be used in the analysis, since there are times in which the beam does not meet the quality standards or parts of the detector are not fully functioning. In Run-2, an integrated luminosity of  $156 \text{ fb}^{-1}$  was delivered in total. Out of this,  $145 \text{ fb}^{-1}$  was recorded by the ATLAS detector and 95.6% of the data was qualified to be ‘good for physics’, amounting to an integrated luminosity of  $139 \text{ fb}^{-1}$  [84]. The qualified luminosity blocks are contained in the Good Runs List (GRL), which is used in the analysis. The GRLs are summarized in table 3.1.

GRL	$\int Ldt[\text{fb}^{-1}]$
data15_13TeV.periodAllYear_DetStatus-v89-pro21-02.Unknown_PHYS.StandardGRL.All.Good.25ns.xml	3.22
data16_13TeV.periodAllYear_DetStatus-v89-pro21-01.DQDefects-00-02-04.PHYS.StandardGRL.All.Good.25ns.xml	32.99
data17_13TeV.periodAllYear_DetStatus-v99-pro22-01.Unknown_PHYS.StandardGRL.All.Good.25ns.Triggerno17e33prim.xml	44.31
data18_13TeV.periodAllYear_DetStatus-v102-pro22-04.Unknown_PHYS.StandardGRL.All.Good.25ns.Triggerno17e33prim.xml	58.45

Table 3.1: GRLs used in this analysis and their corresponding integrated luminosity.

### 3.2 Signal

The signal process, namely pair production of vector leptoquarks, is simulated using various softwares and Monte Carlo (MC) generators, specialized in each step of the process.

Usually, theorists use FEYNRULES [85] to derive Feynman rules from the Lagrangian of a physics model, which formats the results in Universal FEYNRULES Output (UFO) [86]. The UFO can be read by MC generators to simulate physics processes of the corresponding model. The UFO used in this work can be found at [87].

In this work, the MADGRAPH5\_AMC@NLO (v2.8.1) [88] framework is used for the simulation of the hard-scattering processes at parton level. MADGRAPH5 computes the scattering matrix elements using the UFO provided by theorists at leading order (LO) in QCD. At this step, the momentum distribution of partons in the protons is interpolated by LHAPDF (v6.2.3) [89], using NNPDF 3.0 NLO [90] PDF sets. In subsequent two-body decays of the leptoquarks,

MADSPIN [91] is used to preserve spin correlations. As the width can be exactly computed for two-body decays, an analytic formula derived by FEYNRULES and stored in the UFO is used [92].

The hadronization and parton shower of the parton-level processes are simulated using PYTHIA (v8.244) [93], with NNPDF 2.3 LO [94] PDF sets and the A14 set of tuned parameters [95]. Subsequent decays of heavy-flavor hadrons are simulated by EVTGEN (v1.7.0) [96]. The detector response and object reconstruction is simulated by AtlFast-II (AFII). The simulated signal samples are listed in appendix A.

The MC samples are generated in three different subcampaigns. MC16a is used only for 2015 and 2016 data, while MC16d is for 2017 and MC16e for 2018. These subcampaigns reflect changes made in the ATLAS detector and pile-up profile of each data taking period. The number of LQ signal samples for each mass and subcampaign is summarized in table 3.2.

In the previous search for third-generation scalar LQ [63], a parameter space consisting of the mass of LQ ( $m(\text{LQ})$ ) and branching ratio to charged leptons ( $B(\text{LQ}_3^u \rightarrow b\tau)$  and  $B(\text{LQ}_3^d \rightarrow t\tau)$ ) was scanned. As the mass of the top quark cannot be neglected, the branching ratio  $B$  deviates from  $\beta$  defined in eq. (1.64) for the third-generation LQ. The desired branching ratio was obtained by reweighting the MC events generated with  $\beta = 0.5$ , without having to produce additional samples. This work studies the same parameter space and reweighting method. However, one thing to note is that the branching ratio to charged leptons is different for the vector LQ. This is discussed in section 5.2.

Denoting the theoretical branching ratio of the LQ into charged leptons by  $\hat{B}_{\text{cl}}$ , the number of charged leptons ( $n_{\text{cl}} = 0, 1, 2$ ) originating from a pair of leptoquarks obeys the following probability distribution:

$$P(n_{\text{cl}}, \hat{B}_{\text{cl}}) = \begin{cases} (1 - \hat{B}_{\text{cl}})^2, & \text{for } n_{\text{cl}} = 0 \\ 2\hat{B}_{\text{cl}}(1 - \hat{B}_{\text{cl}}), & \text{for } n_{\text{cl}} = 1 \\ \hat{B}_{\text{cl}}^2, & \text{for } n_{\text{cl}} = 2. \end{cases} \quad (3.1)$$

To obtain an arbitrary branching ratio  $B_{\text{cl}}$  instead of  $\hat{B}_{\text{cl}}$ , a weight of

$$w(B_{\text{cl}}) = \frac{P(n_{\text{cl}}, B_{\text{cl}})}{P(n_{\text{cl}}, \hat{B}_{\text{cl}})}$$

must be assigned to each event. From eq. (3.1) follows a convenient formula for reweighting:

$$w(B_{\text{cl}}) = \left(\frac{B_{\text{cl}}}{\hat{B}_{\text{cl}}}\right)^{n_{\text{cl}}} \times \left(\frac{1 - B_{\text{cl}}}{1 - \hat{B}_{\text{cl}}}\right)^{(2 - n_{\text{cl}})}. \quad (3.2)$$

$m_{\text{LQ}}[\text{GeV}]$	MC16a	MC16d	MC16e	$N_{\text{events}}$
300	90,000	120,000	150,000	360,000
400	80,000	100,000	120,000	300,000
500	230,000	290,000	370,000	890,000
600	80,000	100,000	120,000	300,000
700	80,000	100,000	120,000	300,000
800	80,000	100,000	120,000	300,000
900	180,000	230,000	290,000	700,000
1000	50,000	70,000	90,000	210,000
1100	50,000	70,000	90,000	210,000
1200	50,000	70,000	90,000	210,000
1300	140,000	180,000	230,000	550,000
1400	10,000	20,000	20,000	50,000
1450	10,000	20,000	20,000	50,000
1500	10,000	20,000	20,000	50,000
1550	10,000	20,000	20,000	50,000
1600	10,000	10,000	10,000	30,000
1650	10,000	10,000	10,000	30,000
1700	50,000	70,000	80,000	200,000
1750	10,000	10,000	10,000	30,000
1800	10,000	10,000	10,000	30,000
1850	10,000	10,000	10,000	30,000
1900	10,000	10,000	10,000	30,000
1950	10,000	10,000	10,000	30,000
2000	10,000	10,000	10,000	30,000
2050	10,000	10,000	10,000	30,000
2100	10,000	10,000	10,000	30,000
2150	10,000	10,000	10,000	30,000
2200	10,000	10,000	10,000	30,000
2250	10,000	10,000	10,000	30,000
2300	10,000	10,000	10,000	30,000
2400	10,000	10,000	10,000	30,000
2500	10,000	10,000	10,000	30,000

Table 3.2: List of LQ masses used for the generation of vector LQ samples with  $N_{\text{events}}$  corresponding to the total number of generated events summed over all MC16 subcampaigns. All samples have been generated with  $g_U = 3.0$  and  $\beta_L^{33} = 1$ .

### 3.3 Standard Model Backgrounds

For pair production of third-generation leptoquarks, the most dominant background process is pair production of top quarks, denoted by  $t\bar{t}$ . Single top quark production also gives a significant contribution. Other background processes with smaller contributions include top-pair production associated with a vector boson or a Higgs boson.

The background processes are summarized in table 3.3, with corresponding MC generators and order of QCD computations.

Physics process	Generator	Parton shower	Tune	Cross section	PDF (generator)	PDF (PS)
$t\bar{t}$	POWHEG-Box v2 [97–100]	PYTHIA 8.230 [93]	A14 [95]	NNLO+NNLL [101]	NNPDF3.0NLO [90]	NNPDF2.3LO [94]
Single top	POWHEG-Box v2 [98–100, 102]	PYTHIA 8.230	A14	NLO+NNLL [103–106]	NNPDF3.0NLO	NNPDF2.3LO
$V + jets$ ( $V = W, Z$ )	SHERPA 2.2.1 [107]	SHERPA 2.2.1	SHERPA default	NNLO [108]	NNPDF3.0NLO [90]	NNPDF3.0NNLO
Diboson $VV$ ( $V = W, Z$ )	SHERPA 2.2.1 or 2.2.2 [107]	SHERPA 2.2.1 or 2.2.2	SHERPA default	NLO [109–111]	NNPDF3.0NNLO	NNPDF3.0NNLO
Triboson $VVV$ ( $V = W, Z$ )	SHERPA 2.2.1	SHERPA 2.2.1	SHERPA default	NLO [109–111]	NNPDF3.0NNLO	NNPDF3.0NNLO
$t\bar{t} + V$ ( $V = W, Z$ )	MADGRAPH5_AMC@NLO 2.3.3 [88]	PYTHIA 8.210 [93]	A14	NLO [88, 112]	NNPDF3.0NLO	NNPDF2.3LO
$t\bar{t} + H$	POWHEG-Box v2 [99, 100, 113]	PYTHIA 8.230	A14	NLO [88, 112]	NNPDF3.0NLO	NNPDF2.3LO
$t\bar{t} + WW$	MADGRAPH5_AMC@NLO 2.2.2 [88]	PYTHIA 8.186 [93]	A14	NLO [88]	NNPDF2.3LO	NNPDF2.3LO
$t\bar{t} + WZ$	MADGRAPH5_AMC@NLO 2.3.3	PYTHIA 8.212 [93]	A14	NLO [88]	NNPDF3.0NLO	NNPDF2.3LO
$tWZ$	MADGRAPH5_AMC@NLO 2.3.3	PYTHIA 8.212	A14	NLO [88]	NNPDF3.0NLO	NNPDF2.3LO
$tZ, t\bar{t}t, t\bar{t}\bar{t}$	MADGRAPH5_AMC@NLO 2.3.3	PYTHIA 8.230	A14	NLO [88]	NNPDF3.1NLO [90]	NNPDF2.3LO
Vector $LQ_3$ ( $\mathbb{1Q}_3^3$ )	MADGRAPH5_AMC@NLO 2.8.1	PYTHIA 8.244	A14	LO	NNPDF3.0NLO	NNPDF2.3LO

Table 3.3: Simulated background and signal samples with the corresponding matrix element and parton shower (PS) generators. Also, the cross-section order in  $\alpha_s$  used to normalize the event yield and the parton distribution function (PDF) sets used in the generator and PS simulation are given.



Searches for physics beyond the Standard Model at colliders are challenging because it is not possible to tell if a specific event recorded by the detector came from the investigated ‘signal’ process or a ‘background’ process that has a similar signature. Therefore it is common to count events that pass certain criteria, compare the observed numbers with simulated events and determine whether there is a statistically significant excess of events over the background expectation. The following sections are devoted to the strategies used in the analysis.

## 4.1 Cut-Based Analysis

The parameter space consisting of signatures such as kinematic variables (e.g.  $p_T$ ,  $E_T^{\text{miss}}$ ) and number of identified objects can be divided into several regions with different purposes. A signal region (SR) is a part of the parameter space designed to contain a significant amount of signal events. In contrary, a control region (CR) is situated in a different part of the parameter space where the signal process yields are very low compared to background expectation. In many cases, there is a discrepancy between simulated backgrounds and data in the CR, due to mismodelling of the background processes. Since this leads to systematic uncertainties, simulated background processes are normalized to match the data in the CR. The validation region (VR) lies between the CR and SR and is used to validate the extrapolation of the normalized background prediction. The normalization procedure will be discussed in section 4.3.

This work uses the same cut selections as the stop-stau and scalar LQ search [64]. The configuration of the regions has been optimized for maximal sensitivity using both the stop-stau and the scalar-LQ scenario. The significance was estimated using the following formula [114]:

$$Z_A = \left[ 2 \left( (s + b) \ln \left[ \frac{(s + b)(b + \sigma_b^2)}{b^2 + (s + b)\sigma_b^2} \right] - \frac{b^2}{\sigma_b^2} \ln \left[ 1 + \frac{\sigma_b^2 s}{b(b + \sigma_b^2)} \right] \right) \right]^{1/2} \quad (4.1)$$

where  $s$  and  $b$  are the expected signal and background yields with total background uncertainty  $\sigma_b$ . The analysis has two channels: the di-tau channel targeting low mass splitting ( $\Delta m = m_{\tilde{\tau}} - m_{\tilde{\tau}}$ ) and the single-tau channel targeting high mass splitting and scalar LQ. The preselection criteria for the di-tau and single-tau channels are summarized in table 4.1.

Di-tau preselection	Single-tau preselection
$E_T^{\text{miss}}$ -trigger fired and $E_T^{\text{miss}} > 250$ GeV	
No light leptons ( $e/\mu$ )	
At least two jets	
At least one $b$ -tagged jet	
At least two taus	Exactly one tau
	At least two $b$ -tagged jets

Table 4.1: Preselection cuts for the di-tau and single-tau channel. The cuts above the line are common to both channels and referred to as “common preselection”.

Several variables other than  $E_T^{\text{miss}}$  and  $p_T$  are used to define the regions. In general, the invariant mass of two particles is defined as

$$m(1, 2) = \sqrt{m_1^2 + m_2^2 + 2(E_1 E_2 - \mathbf{p}_1 \cdot \mathbf{p}_2)} \quad (4.2)$$

which becomes

$$m(1, 2) \approx \sqrt{2E_1 E_2 (1 - \cos(\Delta\phi(1, 2)))} \quad (4.3)$$

in the relativistic limit, where  $\Delta\phi(1, 2)$  is the angle between the two particles. If there are invisible particles in the final states, the *transverse mass* can be defined:

$$m_T(\mathbf{p}_T, \mathbf{E}_T^{\text{miss}}) \equiv \sqrt{2p_T E_T^{\text{miss}} (1 - \cos \Delta\phi(\mathbf{p}_T, \mathbf{E}_T^{\text{miss}}))}, \quad (4.4)$$

which resembles eq. (4.3) but considering only transverse components and replacing particles 1 and 2 with the visible particle and missing energy. The key feature of  $m_T$  is that it has a kinematic endpoint at the mass of the mother particle when it decays semi-invisibly, i.e. into a visible daughter and an invisible daughter. For example, when a  $W$  boson decays into a charged lepton ( $l$ ) and a neutrino ( $\nu$ ),

$$\begin{aligned} m_W &= \sqrt{m_l^2 + m_\nu^2 + 2(E_T(l)E_T(\nu) \cosh(\Delta Y) - \mathbf{p}_T(l) \cdot \mathbf{p}_T(\nu))} \\ &\geq \sqrt{2(p_T(l)E_T^{\text{miss}} - \mathbf{p}_T(l) \cdot \mathbf{E}_T^{\text{miss}})} \\ &= m_T(\mathbf{p}_T(l), \mathbf{E}_T^{\text{miss}}) \end{aligned} \quad (4.5)$$

where  $E_T \equiv \sqrt{p_T^2 + m^2}$  and  $\Delta Y$  is the difference in rapidity between the charged lepton and the neutrino [115]. This property of  $m_T$  was used in the search for the  $W$  boson by the UA1 collaboration at the SPS, setting a lower bound on its mass consistent with theoretical predictions [45]. In searches for new particles, applying an  $m_T$ -cut well above the mass of the  $W$  boson suppresses SM backgrounds with such semi-invisible decays.

However, in many scenarios including the stop-stau and leptoquarks produced in pairs, there are two or more semi-invisibly decaying particles. In such cases,  $\mathbf{E}_T^{\text{miss}}$  contains contributions from two or more invisible particles which cannot be distinguished. Another variable called the *stransverse mass* is hence defined [115, 116]:

$$m_{T2}(\mathbf{p}_T^1, \mathbf{p}_T^2, \mathbf{E}_T^{\text{miss}}) \equiv \min_{\mathbf{q}_T^a + \mathbf{q}_T^b = \mathbf{E}_T^{\text{miss}}} \left( \max \left[ m_T(\mathbf{p}_T^1, \mathbf{q}_T^a), m_T(\mathbf{p}_T^2, \mathbf{q}_T^b) \right] \right), \quad (4.6)$$

where  $\mathbf{p}_T^1$  and  $\mathbf{p}_T^2$  are the transverse momenta of the two visible particles. If the transverse momenta of the two invisible particles ( $\mathbf{q}_T^a$  and  $\mathbf{q}_T^b$ ) were known as well, the transverse masses

Variable	CR $t\bar{t}$ (2 real $\tau$ )	CR $t\bar{t}$ (1 real $\tau$ )	VR $t\bar{t}$ (2 real $\tau$ )	VR $t\bar{t}$ (1 real $\tau$ )	SR
$E_T^{\text{miss}}$	–	–	–	–	> 280 GeV
$OS(\tau_1, \tau_2)$	1	–	1	–	1
$m_{T2}(\tau_1, \tau_2)$	< 35 GeV	< 35 GeV	[35, 70] GeV	[35, 70] GeV	> 70 GeV
$m(\tau_1, \tau_2)$	> 50 GeV	> 50 GeV	–	–	–
$m_T(\tau_1)$	> 50 GeV	< 50 GeV	> 70 GeV	< 70 GeV	–

Table 4.2: Definitions of the  $t\bar{t}$  control and validation regions in the di-tau channel as well as the SR definition. Here,  $\tau_{1(2)}$  refers to the leading (subleading) tau candidate. A dash signifies that no requirement on the given variable is applied, while brackets indicate an allowed range for the variable. These cuts follow after the di-tau preselection cuts given in table 4.1.

could be still constrained by the mass of the semi-invisibly decaying mother particles:

$$m_{\text{mother}} \geq \max \left[ m_T(\mathbf{p}_T^1, \mathbf{q}_T^a), m_T(\mathbf{p}_T^2, \mathbf{q}_T^b) \right]. \quad (4.7)$$

Since only the sum of the two momenta ( $\mathbf{q}_T^a + \mathbf{q}_T^b = \mathbf{E}_T^{\text{miss}}$ ) can be known in reality, the mass of the mother particle can only be constrained by the minimum of the quantity in eq. (4.7):

$$m_{\text{mother}} \geq \min_{\mathbf{q}_T^a + \mathbf{q}_T^b = \mathbf{E}_T^{\text{miss}}} \left( \max \left[ m_T(\mathbf{p}_T^1, \mathbf{q}_T^a), m_T(\mathbf{p}_T^2, \mathbf{q}_T^b) \right] \right). \quad (4.8)$$

Thanks to eq. (4.8),  $m_{T2}$  can be a good discriminating variable to suppress SM background processes with semi-invisible decays. Since the semi-invisibly decaying particles to be searched for are much heavier than SM examples like the  $W$  boson, applying an  $m_{T2}$  cut well above its mass can effectively reject such backgrounds. However, even an  $m_{T2}$  cut below the  $W$  boson’s mass effectively reduces backgrounds.

The di-tau channel consists of two CRs, two VRs and one SR. One CR is designed to contain a large number of  $t\bar{t}$  events where both  $W$  bosons originating from the top quarks decay into tau leptons. This region is denoted by ‘CR  $t\bar{t}$  (2 real  $\tau$ )’, with a corresponding VR denoted by ‘VR  $t\bar{t}$  (2 real  $\tau$ )’. These regions require the two tau lepton candidates have opposite electric charges. Another CR is designed to contain  $t\bar{t}$  events where only one of the  $W$  bosons decays into a tau lepton and the other decays hadronically. The hadronic jets can be misidentified as hadronically decaying tau leptons and satisfy the preselection criteria for the di-tau channel. This region is denoted by ‘CR  $t\bar{t}$  (1 real  $\tau$ )’, with a corresponding VR denoted by ‘VR  $t\bar{t}$  (1 real  $\tau$ )’. The SR in the di-tau channel is not used in the leptoquark interpretation. However, the two CRs are used in exclusion fits which will be discussed in section 4.3. The cuts defining the di-tau channel are summarized in table 4.2.

The single-tau channel consists of two CRs, two VRs and two SRs with different purposes. One CR is designed to contain a large number of  $t\bar{t}$  backgrounds where only one tau lepton from the  $W$  boson is identified. This can be the case where only one of the  $W$  bosons decays into a tau lepton, or both  $W$  bosons decay into tau leptons but only one is correctly identified. This region is denoted by ‘CR  $t\bar{t}$  (1 real  $\tau$ )’, with a corresponding VR denoted by ‘VR  $t\bar{t}$  (1 real  $\tau$ )’. Another CR is designed to contain an enhanced number of single-top backgrounds. This region is denoted by ‘CR single top’, with a corresponding VR denoted by ‘VR single top’. As the single-tau channel requires two  $b$ -tagged jets in the preselection, the sum of their  $m_T$  can be defined and used as a discriminating variable:

$$\sum m_T(b_1, b_2) = m_T(b_1) + m_T(b_2). \quad (4.9)$$

For a similar reason, the variable  $s_T$  can be defined as the scalar sum of  $p_T$  of the hadronic tau and the two jets:

$$s_T = p_T(\tau) + p_T(j_1) + p_T(j_2). \quad (4.10)$$

Variable	CR $t\bar{t}$ (1 real $\tau$ )	CR single top	VR $t\bar{t}$ (1 real $\tau$ )	VR single top	SR
$E_T^{\text{miss}}$	> 280 GeV	> 280 GeV	> 280 GeV	> 280 GeV	> 280 GeV
$s_T$	[500, 600] GeV	–	> 600 GeV	–	> 800(600) GeV
$\sum m_T(b_1, b_2)$	[600, 700] GeV	> 800 GeV	[600, 700] GeV	> 800 GeV	> 700 GeV
$m_T(\tau)$	–	< 50 GeV	–	[50, 150] GeV	> 300(150) GeV
$p_T(\tau)$	–	> 80 GeV	–	> 80 GeV	(binned)

Table 4.3: Definitions of the  $t\bar{t}$  (1 real  $\tau$ ) and single-top control and validation regions in the single-tau channel as well as the SR definition. Here,  $b_{1(2)}$  refers to the leading (subleading)  $b$ -jet candidate. A dash signifies that no requirement on the given variable is applied, while brackets indicate an allowed range for the variable. These cuts follow after the single-tau preselection cuts given in table 4.1. Additionally, cuts for the multi-bin SR are enclosed by the parentheses. In the multi-bin SR, the binning in  $p_T(\tau)$  is [50, 100] GeV, [100, 200] GeV and > 200 GeV.

The single-tau channel has two SRs. In addition to the one-bin SR, another SR with looser cuts and three separate bins is defined. This is the ‘multi-bin SR’ used for exclusion fits which will be discussed in section 4.3. The cuts defining the single-tau channel are summarized in table 4.3.

The validity of this configuration for the vector LQ signal model will be discussed in sections 5.3 and 5.4.

## 4.2 The $CL_s$ Method

To quantitatively determine statistical significance of a discrepancy between MC simulation and data, a common way is to do a hypothesis test. In searches for new particles or phenomena, there are two hypotheses. One is that there is no new particle or phenomena in the observed events, denoted by  $H_b$ . Another hypothesis is that some of the observed events are due to new particles or phenomena, denoted by  $H_{s+b}$ . In this work, hypothesis test is done using the  $CL_s$  method [117, 118], which was devised in searches for the Higgs boson at the Large Electron-Positron Collider (LEP) [119].

The simplest case is counting events in a single bin, where  $n_{\text{obs}}$  events are observed. Setting  $H_b$  as the null hypothesis, the probability that  $n_{\text{obs}}$  or more events happen is

$$p_b = \sum_{n > n_{\text{obs}}} \mathcal{P}(n|H_b)$$

where  $\mathcal{P}(n|H_b)$  is the probability distribution under the condition that null hypothesis  $H_b$  is true. If  $p_b$  is sufficiently small, the probability that the excess of events is due to statistical fluctuation is small and the alternative hypothesis  $H_{s+b}$  is favored, rejecting  $H_b$ . This can be expressed using significance  $Z$ , defined as

$$Z = \Phi^{-1}(1 - p_b)$$

where  $\Phi^{-1}$  is the inverse of the cumulative Gaussian distribution. Conventionally,  $Z \geq 3$  is interpreted as ‘evidence’ and  $Z \geq 5$  as ‘discovery’ in particle physics.

Likewise, setting  $H_{s+b}$  as the null hypothesis, the probability that  $n_{\text{obs}}$  or less events happen is

$$p_{s+b} = \sum_{n \leq n_{\text{obs}}} \mathcal{P}(n|H_{s+b})$$

If  $p_{s+b}$  is sufficiently small, the probability that there was any contribution from the signal is small and the alternative hypothesis  $H_b$  is favored, rejecting  $H_{s+b}$ .

In this simple example,

$$\text{CL}_s = \frac{p_{s+b}}{1 - p_b}. \quad (4.11)$$

can be interpreted as an approximation of confidence level in case of a signal-only experiment, which does not exist in most cases. In exclusion, where  $H_{s+b}$  is the null hypothesis,  $\text{CL}_s$  reduces the false-exclusion rate.

In actual searches, the *likelihood* is defined as the product of Poisson distributions [120]:

$$\begin{aligned} L(\mathbf{n}, \boldsymbol{\theta}^0 | \mu_{\text{sig}}, \mathbf{b}, \boldsymbol{\theta}) &= P_{\text{SR}} \times P_{\text{CR}} \times C_{\text{sys}} \\ &= P(n_S | \lambda_S(\mu_{\text{sig}}, \mathbf{b}, \boldsymbol{\theta})) \times \prod_{i \in \text{CR}} P(n_i | \lambda_i(\mu_{\text{sig}}, \mathbf{b}, \boldsymbol{\theta})) \times C_{\text{sys}}(\boldsymbol{\theta}^0, \boldsymbol{\theta}). \end{aligned} \quad (4.12)$$

In eq. (4.12),  $P_{\text{SR}}$  is the probability distribution of event counts  $n_S$  in the SR(s) where  $\lambda_S$  is the Poisson expectation value depending on background predictions  $\mathbf{b}$  and nuisance parameters  $\boldsymbol{\theta}$ . Likewise,  $P_{\text{CR}}$  is the product of Poisson distributions of event counts  $n_i$  in each CR  $i$ , where  $\lambda_i$  is the Poisson expectation value. The last factor  $C_{\text{sys}}$  is the probability distribution of nuisance parameters where the systematic uncertainties are included. The nominal values of the nuisance parameters are  $\boldsymbol{\theta}^0$ . The parameter  $\mu_{\text{sig}}$  is called the *signal strength* which equals to 0 in absence of signal and 1 for nominal value of the signal model.

The *profile log likelihood ratio* is defined as

$$q_{\mu_{\text{sig}}} = -2 \ln \left( \frac{L(\mu_{\text{sig}}, \hat{\boldsymbol{\theta}})}{L(\hat{\mu}_{\text{sig}}, \hat{\boldsymbol{\theta}})} \right) \quad (4.13)$$

where  $\hat{\mu}_{\text{sig}}$  and  $\hat{\boldsymbol{\theta}}$  maximize the likelihood  $L$  and  $\hat{\boldsymbol{\theta}}$  maximizes the likelihood for a specific value of  $\mu_{\text{sig}}$ . This is the test statistic used in actual hypothesis tests, where the  $\text{CL}_s$  values are computed using the probability distribution of  $q_{\mu_{\text{sig}}}$ .

### 4.3 Discovery and Exclusion Fits

In this analysis, hypothesis tests are done by the HistFitter framework [120]. The normalization of simulation is usually called *fits* and categorized into the following three types.

- **Background-only fit:** only the simulated backgrounds are normalized in the CRs to match the data. This is extrapolated to the VRs and SRs. Until this step, the data in the SRs stays *blinded* to avoid biasing the analysis. Once a good agreement with the data in the VRs is checked, the SRs are then *unblinded*.
- **Model-independent signal fit:** also known as the *discovery fit*, this fit is used to check if there is a significant excess of events in the SR. In this case, backgrounds and dummy signals are used in the CRs and a one-bin SR. The p-values and  $\text{CL}_s$  values are obtained under the background-only hypothesis  $H_b$ . As no significant excess was found [64], only the model-dependent fit is used in this thesis to set limits on the vector LQ signal model.
- **Model-dependent signal fit:** also known as the *exclusion fit*, this fit uses both the background and signal predictions in the CRs and (possibly multi-bin) SRs. The p-values and  $\text{CL}_s$  values are obtained under the signal+background hypothesis  $H_{s+b}$ . Conventionally, signal points with  $\text{CL}_s$  values under 0.05 are excluded.

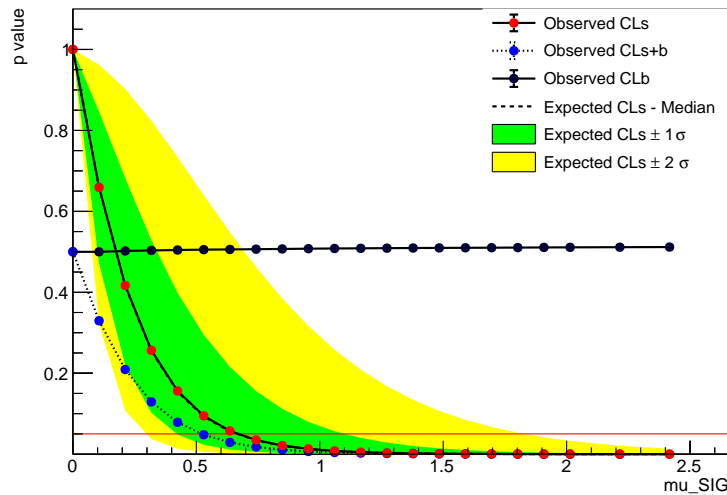


Figure 4.1: An example of upper limit scan in the multi-bin SR, for  $U_1$  vector LQ with  $m(\text{LQ}) = 1.7 \text{ TeV}$  and  $B(\text{LQ} \rightarrow b\tau) = 0.5$  in the Yang-Mills case. The p-value is represented by the  $\text{CL}_s$  value which varies depending on the signal strength ( $\mu_{\text{SIG}}$ ).

In exclusion fits, simulated background yields can be used instead of the actual data in the SRs, in which case the exclusion limit is called the *expected limit*. Another limit set using the actually observed event yields is called the *observed limit*.

## 4.4 Upper Limits

While running an exclusion fit, HistFitter [120] can scan a range of the signal strength parameter ( $\mu_{\text{sig}}$ ). The  $\text{CL}_s$  value decreases when  $\mu_{\text{sig}}$  increases and a point where  $\text{CL}_s$  falls below 0.05 can be found. The  $\mu_{\text{sig}}$  value at this point is called the upper limit of 95% confidence level, which means the signal strength above this value is excluded. An example of the upper limit scan is shown in fig. 4.1. By scaling the upper limit by the production cross section of the corresponding signal, upper limits can be set on the cross section. The results of the upper limit scan are shown in appendix C.3.

Although the scalar and vector leptoquarks can yield the same final states, their theoretical differences make it worthwhile to check in which experimental aspects they differ. The production cross section of the vector LQ first needs to be compared with the scalar LQ, since it is a key factor in limit-setting. As the analysis scans the branching ratio into charged leptons ( $B(\text{LQ} \rightarrow b\tau)$ ) by reweighting each simulated event, the decay width and branching ratio of the vector LQ also need to be checked. To confirm the reliability of the reinterpretation of the scalar LQ search, kinematics and signal acceptance are checked at truth-level, i.e. using only MC generator information.

## 5.1 Production Cross Section

As dominant processes in pair production of leptoquarks are gluon-gluon fusion and quark-antiquark annihilation, differences in these partonic processes lead to different cross sections in proton-proton collisions. For scalar leptoquarks, the leading order cross section follows generic formulae for scalar bosons interacting via QCD [65, 121, 122]:

$$\sigma(gg \rightarrow \text{LQ}_S \overline{\text{LQ}}_S) = \frac{\pi\alpha_s^2}{96\hat{s}} \left\{ \beta (41 - 31\beta^2) - (17 - 18\beta^2 + \beta^4) \ln \frac{1+\beta}{1-\beta} \right\} \quad (5.1)$$

$$\sigma(q\bar{q} \rightarrow \text{LQ}_S \overline{\text{LQ}}_S) = \frac{2\pi\alpha_s^2}{27\hat{s}} \beta^3, \quad (5.2)$$

where  $\hat{s}$  is the Mandelstam variable defined as

$$\hat{s} = \begin{cases} (p_{g_1} + p_{g_2})^2 = (p_{\text{LQ}} + p_{\overline{\text{LQ}}})^2, & \text{in } g_1 g_2 \rightarrow \text{LQ} \overline{\text{LQ}} \\ (p_q + p_{\bar{q}})^2 = (p_{\text{LQ}} + p_{\overline{\text{LQ}}})^2, & \text{in } q\bar{q} \rightarrow \text{LQ} \overline{\text{LQ}} \end{cases}$$

in the parton-level diagrams. The parameter  $\beta$  is defined as

$$\beta \equiv \sqrt{1 - \frac{4m_{\text{LQ}}^2}{\hat{s}}}, \quad (5.3)$$

which is not to be confused with eq. (1.64). Vector leptoquarks have additional parameters that determine whether they are gauge bosons or strongly interacting composite bosons. For the  $U_1$  LQ,  $\kappa_U$  and  $\tilde{\kappa}_U$  are such parameters. Assuming only QCD processes contribute, cross sections can be computed generically for all vector leptoquarks in terms of  $\kappa$ , which is  $\kappa_U$  in the case of  $U_1$  [65]:

$$\begin{aligned}
& \sigma(gg \rightarrow \text{LQ}_V \overline{\text{LQ}}_V) \\
&= \frac{\pi \alpha_s^2}{96 m_{\text{LQ}}^2} \left[ \beta \left( \frac{523}{4} - 90\beta^2 + \frac{93}{4}\beta^4 \right) - \frac{3}{4} (65 - 83\beta^2 + 19\beta^4 - \beta^6) \ln \frac{1+\beta}{1-\beta} \right. \\
&\quad + \kappa \left\{ -4\beta (41 - 9\beta^2) - \frac{87}{2} (1 - \beta^2) \ln \frac{1+\beta}{1-\beta} \right\} \\
&\quad + \kappa^2 \left\{ \beta (75 - 9\beta^2) + \frac{7}{4} \beta \frac{\hat{s}}{m_{\text{LQ}}^2} - \frac{1}{4} (1 - 61\beta^2) \ln \frac{1+\beta}{1-\beta} \right\} \\
&\quad + \kappa^3 \left\{ -9\beta - \frac{7}{4} \beta \frac{\hat{s}}{m_{\text{LQ}}^2} - \left( \frac{103}{8} + \frac{3}{8}\beta^2 \right) \ln \frac{1+\beta}{1-\beta} \right\} \\
&\quad \left. + \kappa^4 \left\{ \frac{41}{24} \beta + \frac{11}{12} \beta \frac{\hat{s}}{m_{\text{LQ}}^2} + \left( \frac{7}{4} + \frac{1}{8}\beta^2 \right) \ln \frac{1+\beta}{1-\beta} \right\} \right], \tag{5.4}
\end{aligned}$$

$$\begin{aligned}
& \sigma(q\bar{q} \rightarrow \text{LQ}_V \overline{\text{LQ}}_V) \\
&= \frac{4\pi \alpha_s^2}{9 m_{\text{LQ}}^2} \beta^3 \left\{ \frac{1}{24} \frac{\hat{s}}{m_{\text{LQ}}^2} + \frac{23 - 3\beta^2}{24} + \kappa \left( -\frac{1}{12} \frac{\hat{s}}{m_{\text{LQ}}^2} - \frac{5}{6} \right) + \kappa^2 \left( \frac{1}{24} \frac{\hat{s}}{m_{\text{LQ}}^2} + \frac{1}{6} \right) \right\}. \tag{5.5}
\end{aligned}$$

The cross section in proton-proton collisions at the center-of-mass energy  $\sqrt{s} = 13$  TeV is shown in fig. 5.1. The vector LQ in the minimal coupling case shows cross sections larger than the scalar LQ in order of 10. The Yang-Mills case shows enhanced cross sections which are a few times larger than in the minimal coupling case.

## 5.2 Decay Width and Branching Ratio

Once produced, leptoquarks decay into a lepton and a quark. The general formula for decay width of a scalar LQ is

$$\begin{aligned}
\Gamma(\text{LQ}_S \rightarrow ql) &= |y_{ql}|^2 \frac{\sqrt{m_{\text{LQ}}^4 + m_q^4 + m_l^4 - 2(m_{\text{LQ}}^2 m_q^2 + m_{\text{LQ}}^2 m_l^2 + m_q^2 m_l^2)}}{16\pi m_{\text{LQ}}^3} \\
&\quad \times (m_{\text{LQ}}^2 - m_q^2 - m_l^2), \tag{5.6}
\end{aligned}$$

where  $q$  and  $l$  are the quark and lepton the LQ couples to and  $y_{ql}$  denotes the Yukawa coupling. In the limit where the fermion masses become negligible, the decay width becomes  $\Gamma \approx \frac{|y|^2}{16\pi} m_{\text{LQ}}$ . However, this is not a good approximation for third generation leptoquarks due to the top quark mass. Using the Yukawa coupling constants given in eq. (1.64) and setting the  $b$  quark and all leptons massless, the decay width of the up-type scalar LQ becomes

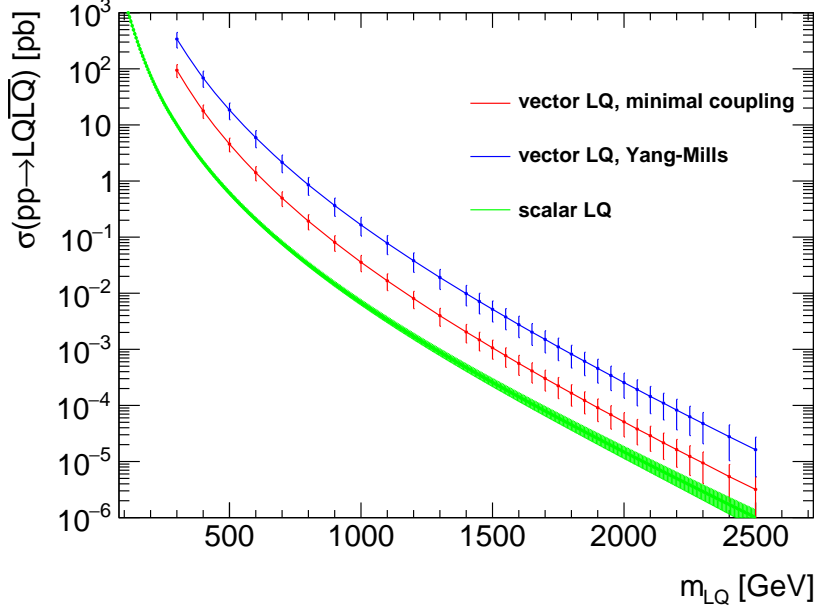


Figure 5.1: Cross section of pair production of scalar and vector leptoquarks in proton-proton collisions at the center-of-mass energy of  $\sqrt{s} = 13$  TeV. The cross section of scalar leptoquark is computed at NNLO<sub>approx</sub> + NNLL. The cross section of vector leptoquark is computed at LO. The error bars indicate theoretical uncertainties, which will be discussed in section 6.1.

$$\Gamma(\text{LQ}_3^u \rightarrow t\nu_\tau) = \frac{\lambda^2(1-\beta)}{16\pi m_{\text{LQ}}^3} (m_{\text{LQ}}^2 - m_t^2)^2, \quad (5.7)$$

$$\Gamma(\text{LQ}_3^u \rightarrow b\tau) = \frac{\lambda^2\beta}{16\pi m_{\text{LQ}}^3} m_{\text{LQ}}^4. \quad (5.8)$$

Using eqs. (5.7) and (5.8) and setting  $\beta = 0.5$ , the branching ratio  $B(\text{LQ}_3^u \rightarrow b\tau)$  becomes

$$B(\text{LQ}_3^u \rightarrow b\tau) = \frac{m_{\text{LQ}}^4}{(m_{\text{LQ}}^2 - m_t^2)^2 + m_{\text{LQ}}^4}. \quad (5.9)$$

The formula is different for vector leptoquarks:

$$\begin{aligned} \Gamma(\text{LQ}_V \rightarrow ql) = & |y_{ql}|^2 \frac{\sqrt{m_{\text{LQ}}^4 + m_q^4 + m_l^4 - 2(m_{\text{LQ}}^2 m_q^2 + m_{\text{LQ}}^2 m_l^2 + m_q^2 m_l^2)}}{48\pi m_{\text{LQ}}^3} \\ & \times \frac{2m_{\text{LQ}}^4 - m_q^4 - m_l^4 - m_{\text{LQ}}^2 m_q^2 - m_{\text{LQ}}^2 m_l^2 + 2m_q^2 m_l^2}{m_{\text{LQ}}^2} \end{aligned} \quad (5.10)$$

In the limit where the fermion masses become negligible, the decay width becomes  $\Gamma \approx \frac{|y|^2}{24\pi} m_{\text{LQ}}$ . The reason of the difference between eqs. (5.6) and (5.10) is discussed in appendix B. For the benchmark model of  $U_1$  vector LQ used in this thesis, the fermion coupling terms

in eq. (1.65) can be explicitly expanded:

$$\begin{aligned}\mathcal{L}_{\text{int}} &= \frac{gU}{\sqrt{2}} [U_1^\mu (\beta_L^{ij} \bar{q}_L^i \gamma_\mu l_L^j + \beta_R^{ij} \bar{d}_R^i \gamma_\mu e_R^j) + \text{h.c.}] \\ &= \frac{gU}{\sqrt{2}} [U_1^\mu \bar{q}_L^3 \gamma_\mu l_L^3 + \text{h.c.}] \\ &= \frac{gU}{\sqrt{2}} [V_{13} U_1^\mu \bar{u}_L \gamma_\mu \nu_{\tau L} + V_{23} U_1^\mu \bar{c}_L \gamma_\mu \nu_{\tau L} + V_{33} U_1^\mu \bar{t}_L \gamma_\mu \nu_{\tau L} + U_1^\mu \bar{b}_L \gamma_\mu \tau_L + \text{h.c.}].\end{aligned}$$

Thus the individual couplings corresponding to  $y_{ql}$  in eq. (5.10) are

$$y_{b\tau} = \frac{gU}{\sqrt{2}}, \quad y_{t\nu_\tau} = \frac{gU}{\sqrt{2}} V_{33}, \quad y_{c\nu_\tau} = \frac{gU}{\sqrt{2}} V_{23}, \quad y_{u\nu_\tau} = \frac{gU}{\sqrt{2}} V_{13}.$$

Setting all fermions but the top quark massless, eq. (5.10) is simplified to eqs. (5.11) to (5.14):

$$\Gamma(\text{LQ}_3^v \rightarrow t\nu_\tau) = \frac{g_U^2}{2} |V_{33}|^2 \frac{(m_{\text{LQ}}^2 - m_t^2)^2 \left(1 + \frac{m_t^2}{2m_{\text{LQ}}^2}\right)}{24\pi m_{\text{LQ}}^3} \quad (5.11)$$

$$\Gamma(\text{LQ}_3^v \rightarrow c\nu_\tau) = \frac{g_U^2}{2} |V_{23}|^2 \frac{m_{\text{LQ}}^4}{24\pi m_{\text{LQ}}^3} \quad (5.12)$$

$$\Gamma(\text{LQ}_3^v \rightarrow u\nu_\tau) = \frac{g_U^2}{2} |V_{13}|^2 \frac{m_{\text{LQ}}^4}{24\pi m_{\text{LQ}}^3} \quad (5.13)$$

$$\Gamma(\text{LQ}_3^v \rightarrow b\tau) = \frac{g_U^2}{2} \frac{m_{\text{LQ}}^4}{24\pi m_{\text{LQ}}^3}, \quad (5.14)$$

where the values of the CKM matrix elements are

$$V_{13} = 0.00134 - 0.00346i, \quad V_{23} = 0.0397, \quad V_{33} = 0.9992.$$

Thus the branching ratio into charged lepton becomes

$$B(\text{LQ}_3^v \rightarrow b\tau) = \frac{m_{\text{LQ}}^4}{|V_{33}|^2 (m_{\text{LQ}}^2 - m_t^2)^2 \left(1 + \frac{m_t^2}{2m_{\text{LQ}}^2}\right) + |V_{13}|^2 m_{\text{LQ}}^4 + |V_{23}|^2 m_{\text{LQ}}^4 + m_{\text{LQ}}^4}. \quad (5.15)$$

Plotting eqs. (5.9) and (5.15), the branching ratio of vector LQ deviates from scalar LQ as fig. 5.2 shows. The cross-generational branching ratio  $B(\text{LQ}_3^v \rightarrow c\nu_\tau)$  is negligible.

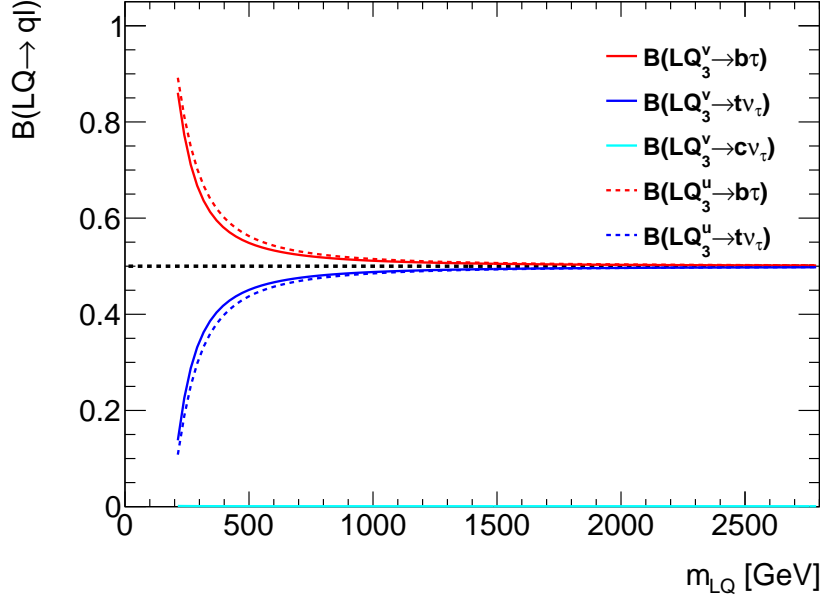


Figure 5.2: Branching ratio of scalar and vector leptoquark into charged or uncharged leptons with respect to  $m_{LQ}$ .

In actual MC simulations, it is possible to restrict the decays using MADSPIN commands such that the leptoquarks decay only into the third generation fermions without crossing generations. This simplifies eq. (5.15) to

$$B(LQ_3^v \rightarrow b\tau) = \frac{m_{LQ}^4}{|V_{33}|^2 (m_{LQ}^2 - m_t^2)^2 \left(1 + \frac{m_t^2}{2m_{LQ}^2}\right) + m_{LQ}^4}. \quad (5.16)$$

Using eq. (5.16) instead of eq. (5.15), the branching ratio is plotted in fig. 5.3 in comparison with the scalar LQ.

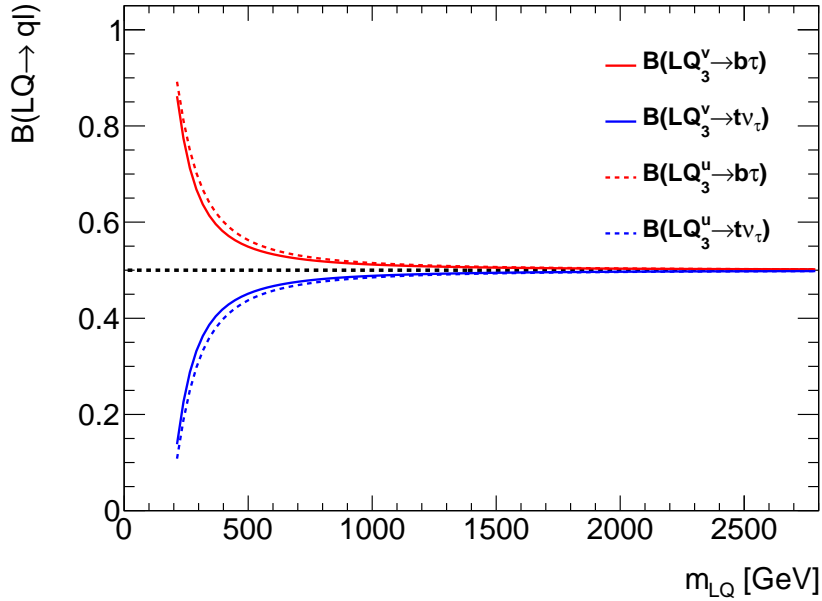


Figure 5.3: Branching ratio of scalar and vector leptoquark into charged or uncharged leptons. Cross-generational decays of the vector LQ are manually suppressed with MADSPIN commands and the branching ratio follows eq. (5.16).

### 5.3 Kinematics

For vector-LQ interpretation of the scalar LQ search, kinematics of vector LQ needs to be checked in comparison with the scalar LQ. The comparison is at truth-level, i.e. using only MC generator information stored in Les Houches Event Files (LHE) generated by MADGRAPH5 (v2.7.3). The momentum distribution of partons in the protons is interpolated by LHAPDF [89], using NNPDF 2.3 [94] parton distribution functions (PDF) at leading order (LO) in QCD. The specific PDF set used here is NNPDF23\_nlo\_as\_0119, with  $\alpha_s(m_Z) = 0.119$ . Renormalization and factorization scales are set to  $\mu_R = \mu_F = m_Z$  in this comparison. For vector LQ, both Yang-Mills case ( $\kappa_U = \tilde{\kappa}_U = 0$ ) and minimal coupling case ( $\kappa_U = \tilde{\kappa}_U = 1$ ) are investigated.

Kinematic distributions of simulated LQ pair productions are shown in fig. 5.4. In general, vector LQ has higher  $p_T$  than scalar LQ in pair production (fig. 5.4a). Especially, minimal coupling case shows higher  $p_T$  compared to Yang-Mills case. The  $p_T$  difference is less pronounced at higher LQ masses. To see differences in angular distribution, rapidity ( $Y$ ) and pseudorapidity ( $\eta$ ) are checked. In terms of rapidity which is a Lorentz-invariant quantity, vector LQs are produced more forward, resulting in slightly broader distribution (fig. 5.4b). The difference between minimal coupling case and Yang-Mills case is very small. Comparison of pseudorapidity gives a similar result (fig. 5.4c).

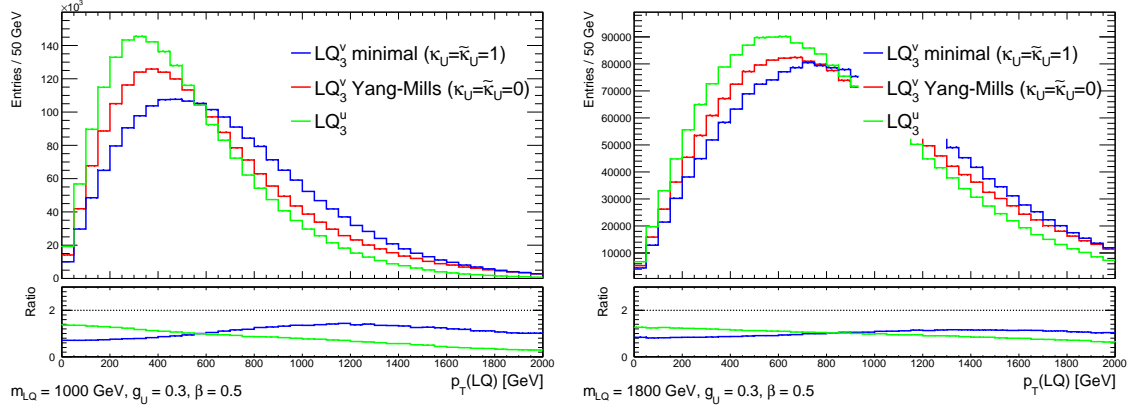
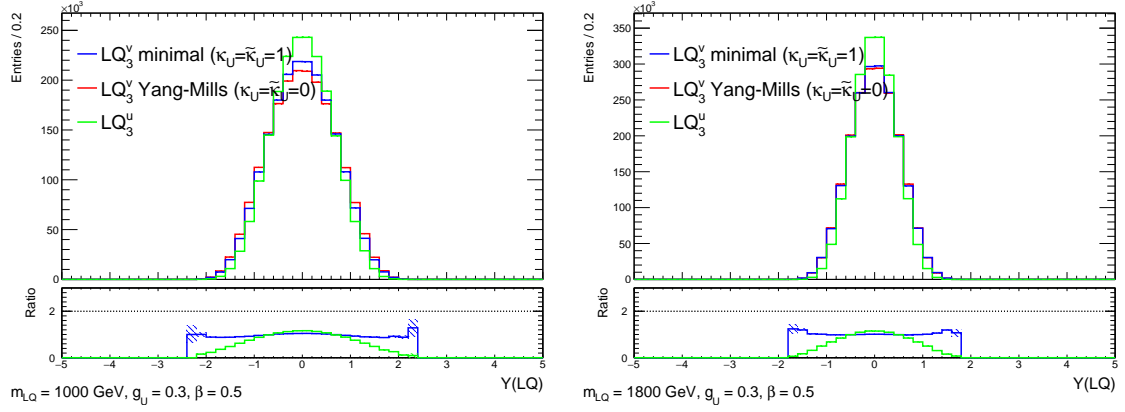
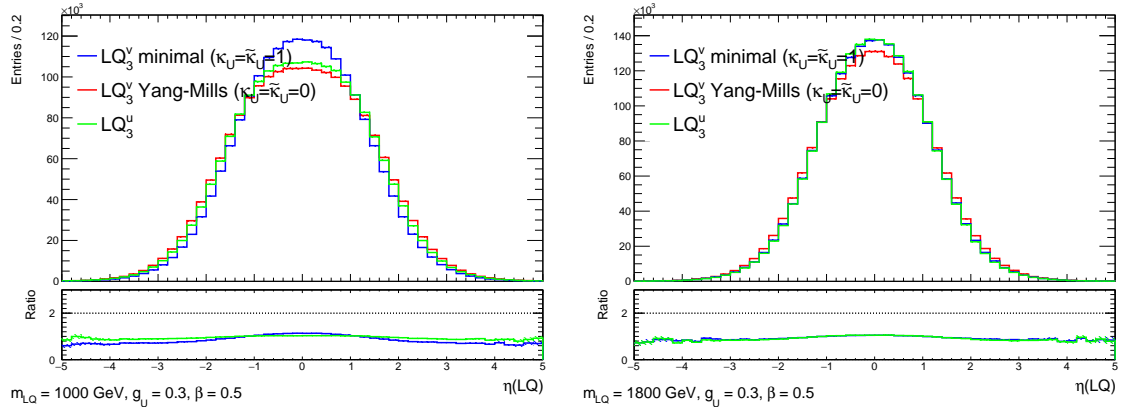
(a)  $p_T(\text{LQ})$ (b) Rapidity ( $Y$ )(c) Pseudorapidity ( $\eta$ )

Figure 5.4: Comparison of kinematic variables of LQ between scalar and vector LQ, at  $m(\text{LQ}) = 1.0 \text{ TeV}$  (left) and  $m(\text{LQ}) = 1.8 \text{ TeV}$  (right). While differences in angular distributions ( $Y$  and  $\eta$ ) are very small,  $p_T$  of LQ shows relatively clear differences.

The possible decay products of the third-generation LQ are the  $b$  and  $t$  quarks, the tau lepton and the tau neutrino. Since the top quark promptly decays into a  $b$  quark and a  $W$  boson,  $b$  quarks are either direct decay products of the LQ or subsequent decay products of the top quarks. For the same reason, tau leptons in the final states are either direct decay products of the LQ or subsequent decay products of the  $W$  bosons.

The  $p_T$  distribution of the tau leptons and  $b$  quarks are shown in figs. 5.5a and 5.5b. As the vector LQ tends to have higher  $p_T$  than the scalar LQ, tau leptons and  $b$  quarks show similar tendencies. However, one notable difference between the scalar and vector LQ is the shape of distribution in the low- $p_T$  bins. This difference becomes clear when looking specifically into the tau leptons and  $b$  quarks originating from the top quarks (figs. 5.5c and 5.5d). Considering MADSPIN simulates the decay of the LQs preserving spin correlations, it needs to be investigated what happens in the subsequent decays of the top quarks.

The SM predicts that about 68% of these  $W$  bosons are longitudinally polarized, while 31% and 1% are left- and right-handed respectively [123]. This prediction agrees with the measurement by the ATLAS collaboration [124]. When a scalar LQ decays into a top quark and an antineutrino, the top quark is right-handed in the LQ rest frame since the antineutrino is right-handed. Taking the helicity of the  $b$  quark into account, 68% of the  $W$  bosons have a momentum component parallel to the top quark, while 31% have an antiparallel component. On the other hand, when a vector LQ decays into a top quark and an antineutrino, the top quark is left-handed in the LQ rest frame since the antineutrino is right-handed. In contrary to the scalar LQ case, 68% of the  $W$  bosons have an antiparallel momentum component, while 31% have a parallel component. This leads to differences in the angular distribution of the  $W$  bosons. This can be clearly demonstrated by comparing the distribution of angles between the momentum of the top quark in the LQ rest frame and its decay products ( $b$ ,  $W$ ) in the top quark's rest frame. The average angle between the top quark and the  $W$  boson ( $\theta(t, W)$ ) is larger for the vector LQ (fig. 5.5e). The average angle between the top quark and the  $b$  quark ( $\theta(t, b)$ ) is larger for the scalar LQ (fig. 5.5f).

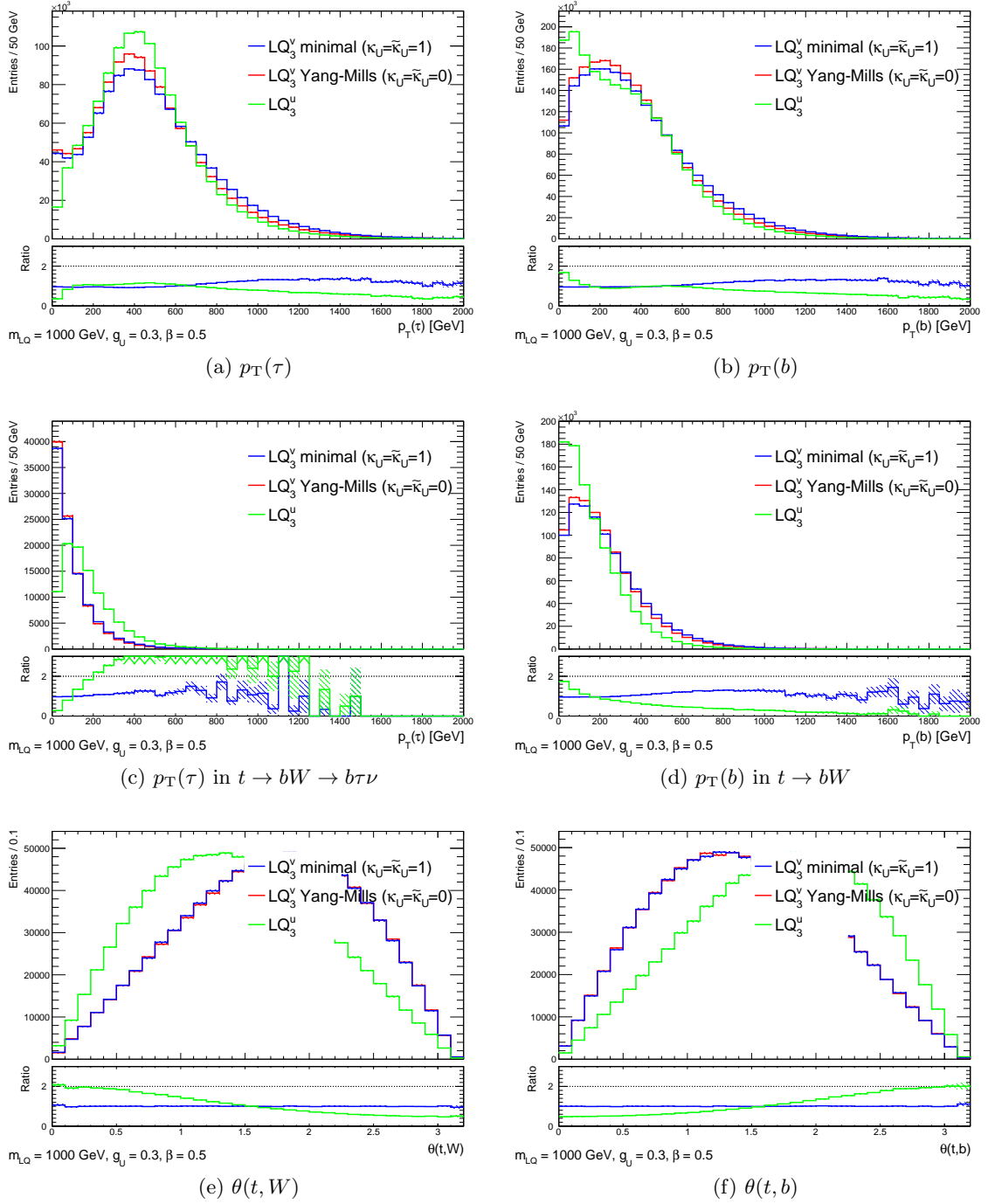


Figure 5.5: Comparison of decay products (tau leptons and  $b$  quarks) of scalar and vector LQ, at  $m(\text{LQ}) = 1.0$  TeV. The top plots show  $p_T$  distributions, including decay products of the subsequent top quark decays. The middle plots show  $p_T$  distributions of the decay products of the top quarks specifically. The bottom plots show the angles between the top quark's momentum in the LQ rest frame and the decay products' momenta in the top quark's rest frame.

Angular distribution of tau leptons originating either from LQ or top quark are shown in fig. 5.6. As the differences in figs. 5.4b and 5.4c are small, differences in  $Y(\tau)$  and  $\eta(\tau)$  are also small.

Since the comparison is done at truth-level, invariant mass of the decay products of the LQ can be compared even when the neutrino is present in the final state. The invariant mass  $m_{ll}$  where  $l$  is either the tau lepton or the tau neutrino, shows that the result is consistent with differences in  $p_T(\text{LQ})$  (fig. 5.7).

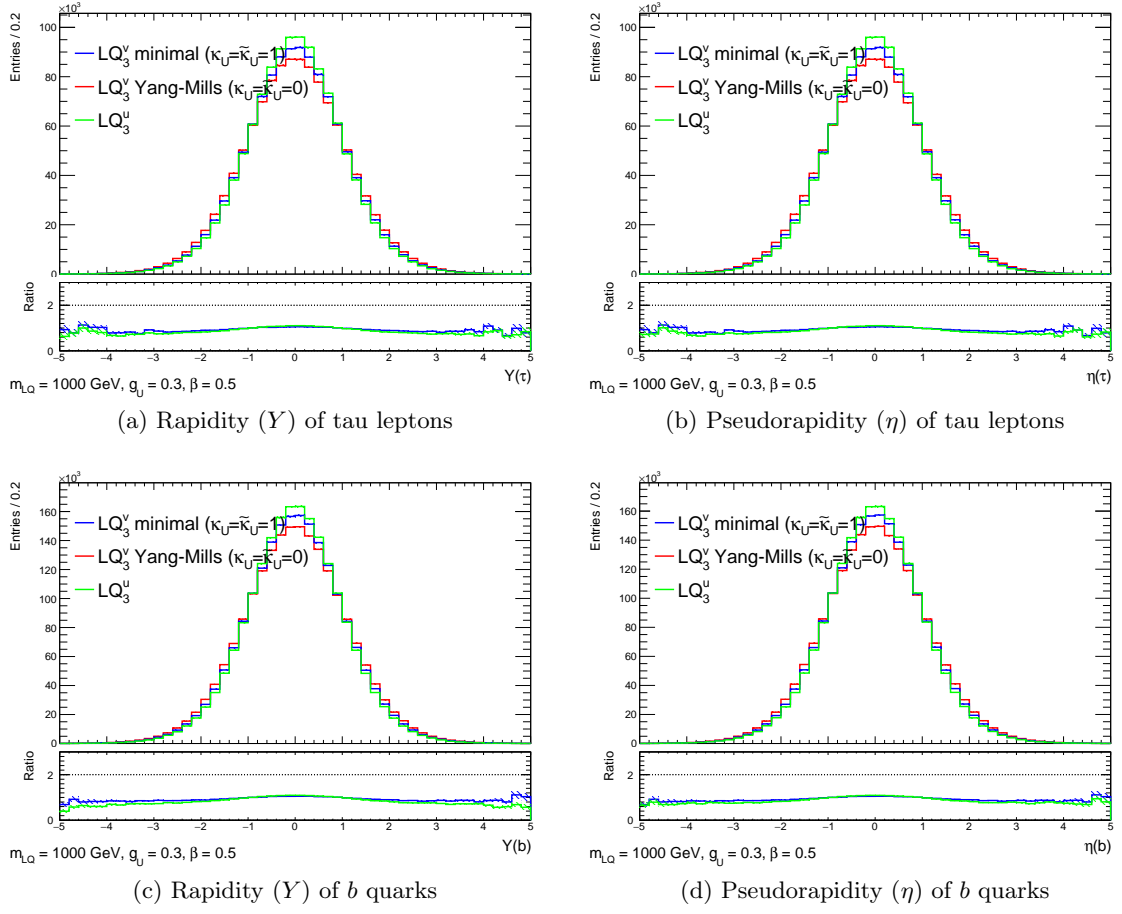


Figure 5.6: Angular distributions of the decay products (tau leptons and  $b$  quarks) of the LQs, at  $m(\text{LQ}) = 1.0$  TeV.

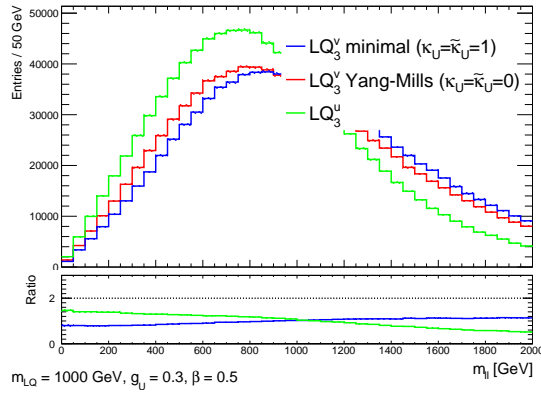


Figure 5.7: Comparison of  $m_{ll}$  ( $l = \tau, \nu_\tau$ ) between scalar LQ and vector LQ at  $m(\text{LQ}) = 1.0$  TeV.

## 5.4 Comparison in the SR

The SimpleAnalysis framework [125] provides tools for truth-level analyses, including ‘smearing’ which mimics the detector responses. Using private TRUTH3 samples with 100,000 events, variables defining the signal regions are compared (fig. 5.8). Only the common preselection cuts of the di-tau and single-tau channels have been applied. For all of these variables, the vector LQ tends to show slightly higher values than the scalar LQ. Since these variables are based on  $p_T$  of the identified objects or  $E_T^{\text{miss}}$ , these differences follow the tendencies in  $p_T$  of the LQ.

SimpleAnalysis can compute acceptance values in each region defined in the analysis, where the acceptance is defined as the fraction of events that pass the cuts. Here, a provisional version of the one-bin discovery SR was used, which has a slightly tighter  $p_T$ -cut ( $p_T > 300$  GeV). To see the difference between the scalar and vector LQ scenarios, cuts defining the SR are applied one-by-one (table 5.1). The minimal coupling case of the vector LQ shows the highest acceptance, followed by the Yang-Mills case and the up-type scalar LQ. This can be again accounted for by the  $p_T$  of LQ, since most of the cuts are related to  $p_T$  of the identified particles and  $E_T^{\text{miss}}$ , and the minimal coupling case showed the highest  $p_T(\text{LQ})$ .

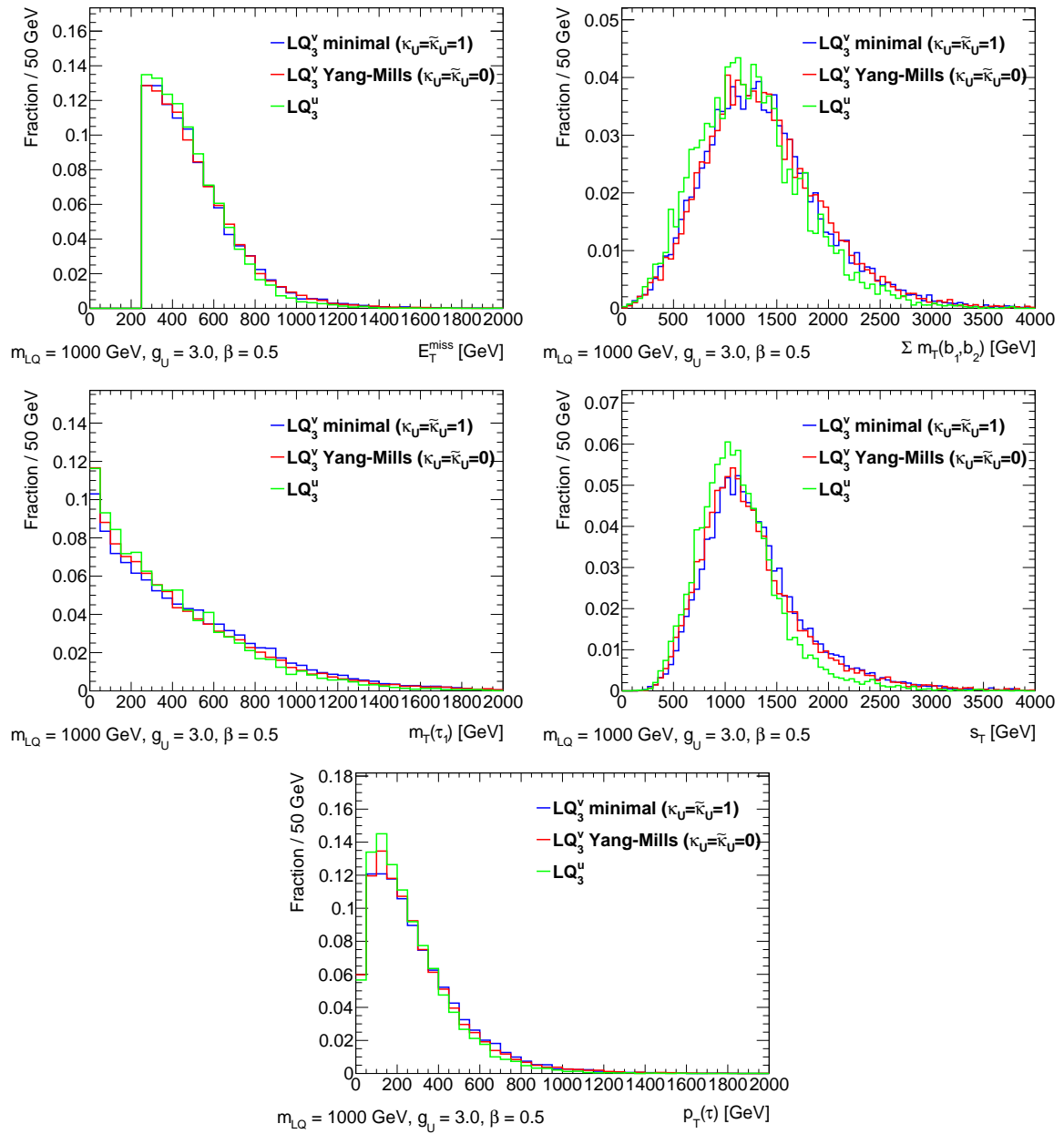


Figure 5.8: Distributions of variables defining the single-tau SRs.

	Preselection	$E_T^{\text{miss}} > 300 \text{ GeV}$	$\sum m_T(b_1, b_2) > 700 \text{ GeV}$	$m_T(\tau) > 300 \text{ GeV}$	$s_T > 800 \text{ GeV}$
$m(\text{LQ}) = 1.0 \text{ TeV}$					
$\text{LQ}_3^{\text{u}}$	0.218	0.153	0.134	0.086	0.079
	$\pm 0.002$	$\pm 0.002$	$\pm 0.002$	$\pm 0.002$	$\pm 0.001$
$\text{LQ}_3^{\text{v}} \text{ (YM)}$	0.234	0.163	0.151	0.101	0.095
	$\pm 0.002$	$\pm 0.001$	$\pm 0.001$	$\pm 0.001$	$\pm 0.001$
$\text{LQ}_3^{\text{v}} \text{ (MC)}$	0.241	0.167	0.154	0.108	0.102
	$\pm 0.002$	$\pm 0.001$	$\pm 0.001$	$\pm 0.001$	$\pm 0.001$
$m(\text{LQ}) = 1.4 \text{ TeV}$					
$\text{LQ}_3^{\text{u}}$	0.227	0.190	0.180	0.131	0.128
	$\pm 0.002$	$\pm 0.002$	$\pm 0.002$	$\pm 0.002$	$\pm 0.002$
$\text{LQ}_3^{\text{v}} \text{ (YM)}$	0.242	0.200	0.192	0.143	0.141
	$\pm 0.002$	$\pm 0.001$	$\pm 0.001$	$\pm 0.001$	$\pm 0.001$
$\text{LQ}_3^{\text{v}} \text{ (MC)}$	0.245	0.203	0.195	0.149	0.146
	$\pm 0.002$	$\pm 0.001$	$\pm 0.001$	$\pm 0.001$	$\pm 0.001$
$m(\text{LQ}) = 1.8 \text{ TeV}$					
$\text{LQ}_3^{\text{u}}$	0.232	0.207	0.199	0.157	0.156
	$\pm 0.002$	$\pm 0.002$	$\pm 0.002$	$\pm 0.002$	$\pm 0.002$
$\text{LQ}_3^{\text{v}} \text{ (YM)}$	0.242	0.215	0.210	0.170	0.168
	$\pm 0.002$	$\pm 0.001$	$\pm 0.001$	$\pm 0.001$	$\pm 0.001$
$\text{LQ}_3^{\text{v}} \text{ (MC)}$	0.245	0.218	0.212	0.173	0.171
	$\pm 0.002$	$\pm 0.001$	$\pm 0.001$	$\pm 0.001$	$\pm 0.001$

Table 5.1: Cutflows and acceptance values in the provisional one-bin SR in the single-tau channel for LQ signal models, with statistical uncertainties. ‘YM’ and ‘MC’ indicate the Yang-Mills case and minimal coupling case of the vector LQ, respectively. Cuts in the first row are applied one-by-one, from left to right.

## 6.1 Uncertainties in Production Cross Section

To estimate theoretical uncertainties in the production cross section of leptoquarks, recommendations by the Physics Modelling Group (PMG) of the ATLAS collaboration [126] are followed. The Leptoquarks Cluster of the ATLAS collaboration recommends using the following uncertainties [127]:

- PDF uncertainties: as the parton distribution functions (PDF) are determined experimentally, they intrinsically include experimental uncertainties. The PDFs are interpolated to functional forms in the actual computations and this adds further uncertainties.
- $\alpha_s$  uncertainty: as the value of the strong coupling  $\alpha_s$  is determined experimentally, the uncertainty in this parameter must be taken into account. Conventionally,  $\alpha_s$  used in each PDF set is represented by its value evaluated at the mass of the  $Z$ -boson ( $\alpha_s(m_Z)$ ).
- Scale uncertainties: in Monte Carlo simulations, the renormalization scale ( $\mu_R$ ) and the factorization scale ( $\mu_F$ ) are conventionally set to the mass of the LQ. As they affect the production cross section, uncertainties originating from variations of these parameters need to be taken into account.

The PMG recommends using prescriptions by the PDF4LHC group [128] to evaluate the PDF and  $\alpha_s$  uncertainties. In the computation, `NNPDF30_nlo_as_0118` is used as the nominal PDF set. As this is a Monte Carlo PDF set, the PDF uncertainty is

$$\delta^{\text{PDF}} \sigma = \sqrt{\frac{1}{N_{\text{mem}} - 1} \sum_{i=1}^{N_{\text{mem}}} (\sigma^{(i)} - \langle \sigma \rangle)^2} \quad (6.1)$$

where  $N_{\text{mem}} = 100$  is the number of replicas in the set and  $\langle \sigma \rangle$  is the mean cross section:

$$\langle \sigma \rangle = \frac{1}{N_{\text{mem}}} \sum_{i=1}^{N_{\text{mem}}} \sigma^{(i)}. \quad (6.2)$$

The  $\alpha_s$  uncertainty is computed using `NNPDF30_nlo_as_0117` and `NNPDF30_nlo_as_0119` (corresponding to  $\alpha_s(m_Z) = 0.117$  and  $\alpha_s(m_Z) = 0.119$  respectively) as alternative PDF sets:

$$\delta^{\alpha_s} \sigma = \frac{\sigma(\alpha_s = 0.119) - \sigma(\alpha_s = 0.117)}{2}. \quad (6.3)$$

The PDF and  $\alpha_s$  uncertainties, which are symmetric by definition, are then combined in quadrature:

$$\delta^{\text{PDF}+\alpha_s}\sigma = \sqrt{(\delta^{\text{PDF}}\sigma)^2 + (\delta^{\alpha_s}\sigma)^2}. \quad (6.4)$$

To evaluate scale uncertainties,  $\mu_R$  and  $\mu_F$  are varied by factor of 2. This yields nine combinations in total:

$$\mu_R = \{0.5, 1, 2.0\} \cdot m_{\text{LQ}}, \quad \mu_F = \{0.5, 1, 2.0\} \cdot m_{\text{LQ}}. \quad (6.5)$$

Out of the nine combinations, two combinations

$$\left\{ \begin{array}{l} \mu_R = \frac{1}{2}m_{\text{LQ}} \\ \mu_F = 2m_{\text{LQ}} \end{array} \right\}, \quad \left\{ \begin{array}{l} \mu_R = 2m_{\text{LQ}} \\ \mu_F = \frac{1}{2}m_{\text{LQ}} \end{array} \right\} \quad (6.6)$$

are excluded. By taking the envelope of the cross sections using the 7-point combinations, relative uncertainties in the cross section can be obtained. These uncertainties are in general asymmetric.

The PDF+ $\alpha_s$  uncertainties are again combined in quadrature:

$$\delta^\pm\sigma = \sqrt{(\delta^{\text{PDF}+\alpha_s}\sigma)^2 + (\delta^{\text{scale}\pm}\sigma)^2}. \quad (6.7)$$

The cross section and relative uncertainties are summarized in tables [6.1](#) and [6.2](#).

type	$m(\text{LQ}_3^v)$ [GeV]	cross section [pb]	scale [%]		PDF+ $\alpha_s$ [%]	relative uncertainties [%]	
min	300	$9.4408 \cdot 10^{+1}$	+25.783	-17.829	3.9584	+26.085	-18.264
min	400	$1.7844 \cdot 10^{+1}$	+26.452	-18.245	5.0424	+26.928	-18.929
min	500	$4.5569 \cdot 10^{+0}$	+26.967	-18.603	5.9697	+27.620	-19.537
min	600	$1.4056 \cdot 10^{+0}$	+27.623	-19.048	6.9850	+28.492	-20.289
min	700	$4.9690 \cdot 10^{-1}$	+28.245	-19.480	7.8372	+29.312	-20.997
min	800	$1.9286 \cdot 10^{-1}$	+28.937	-19.937	9.0932	+30.332	-21.913
min	900	$8.0880 \cdot 10^{-2}$	+29.515	-20.325	9.8545	+31.117	-22.588
min	1000	$3.5659 \cdot 10^{-2}$	+30.241	-20.786	10.794	+32.109	-23.422
min	1100	$1.6647 \cdot 10^{-2}$	+30.837	-21.181	12.119	+33.133	-24.403
min	1200	$8.0461 \cdot 10^{-3}$	+31.463	-21.589	13.151	+34.101	-25.279
min	1300	$3.9740 \cdot 10^{-3}$	+32.163	-22.029	14.262	+35.183	-26.243
min	1400	$2.0364 \cdot 10^{-3}$	+32.730	-22.389	15.565	+36.243	-27.268
min	1450	$1.4738 \cdot 10^{-3}$	+33.044	-22.580	15.808	+36.630	-27.564
min	1500	$1.0622 \cdot 10^{-3}$	+33.400	-22.795	16.825	+37.398	-28.332
min	1550	$7.7058 \cdot 10^{-4}$	+33.703	-22.983	17.812	+38.121	-29.078
min	1600	$5.6119 \cdot 10^{-4}$	+34.066	-23.198	18.830	+38.924	-29.878
min	1650	$4.1260 \cdot 10^{-4}$	+34.311	-23.351	19.180	+39.308	-30.218
min	1700	$3.0228 \cdot 10^{-4}$	+34.665	-23.568	20.747	+40.399	-31.399
min	1750	$2.2331 \cdot 10^{-4}$	+34.926	-23.721	21.164	+40.838	-31.790
min	1800	$1.6557 \cdot 10^{-4}$	+35.156	-23.867	22.127	+41.540	-32.546
min	1850	$1.2280 \cdot 10^{-4}$	+35.483	-24.045	23.595	+42.612	-33.688
min	1900	$9.0981 \cdot 10^{-5}$	+35.774	-24.242	24.689	+43.466	-34.600
min	1950	$6.8297 \cdot 10^{-5}$	+35.954	-24.345	26.628	+44.740	-36.080
min	2000	$5.0885 \cdot 10^{-5}$	+36.314	-24.553	28.301	+46.039	-37.467
min	2050	$3.7987 \cdot 10^{-5}$	+36.437	-24.632	31.130	+47.924	-39.696
min	2100	$2.8842 \cdot 10^{-5}$	+36.661	-24.786	30.196	+47.496	-39.066
min	2150	$2.1543 \cdot 10^{-5}$	+36.880	-24.908	33.153	+49.591	-41.467
min	2200	$1.6317 \cdot 10^{-5}$	+37.053	-25.022	36.085	+51.721	-43.912
min	2250	$1.2373 \cdot 10^{-5}$	+37.247	-25.152	39.752	+54.476	-47.041
min	2300	$9.4279 \cdot 10^{-6}$	+37.313	-25.200	43.010	+56.939	-49.848
min	2400	$5.3893 \cdot 10^{-6}$	+37.567	-25.384	52.045	+64.187	-57.905
min	2500	$3.1852 \cdot 10^{-6}$	+37.735	-25.507	57.059	+68.408	-62.500

Table 6.1: Cross sections and their uncertainties for pair production of vector leptoquarks. ‘min’ denotes the minimal coupling case.

type	$m(\text{LQ}_3^v)$ [GeV]	cross section [pb]	scale [%]		PDF+ $\alpha_s$ [%]	relative uncertainties [%]	
YM	300	$3.3970 \cdot 10^{+2}$	+30.772	-21.628	2.7784	+30.897	-21.806
YM	400	$6.8769 \cdot 10^{+1}$	+31.889	-22.229	3.4228	+32.073	-22.491
YM	500	$1.8463 \cdot 10^{+1}$	+32.753	-22.708	4.0681	+33.005	-23.070
YM	600	$5.9234 \cdot 10^{+0}$	+33.466	-23.094	4.8711	+33.819	-23.602
YM	700	$2.1542 \cdot 10^{+0}$	+34.149	-23.479	5.6966	+34.621	-24.160
YM	800	$8.5507 \cdot 10^{-1}$	+34.624	-23.748	6.4625	+35.222	-24.611
YM	900	$3.6537 \cdot 10^{-1}$	+35.147	-24.047	7.3704	+35.911	-25.151
YM	1000	$1.6483 \cdot 10^{-1}$	+35.689	-24.341	8.1368	+36.605	-25.665
YM	1100	$7.7747 \cdot 10^{-2}$	+36.152	-24.595	8.9668	+37.247	-26.179
YM	1200	$3.7974 \cdot 10^{-2}$	+36.667	-24.873	10.524	+38.147	-27.008
YM	1300	$1.9083 \cdot 10^{-2}$	+37.183	-25.150	11.468	+38.911	-27.641
YM	1400	$9.8516 \cdot 10^{-3}$	+37.651	-25.392	12.455	+39.657	-28.282
YM	1450	$7.1243 \cdot 10^{-3}$	+37.824	-25.494	13.375	+40.119	-28.789
YM	1500	$5.1735 \cdot 10^{-3}$	+38.092	-25.634	14.546	+40.775	-29.474
YM	1550	$3.7790 \cdot 10^{-3}$	+38.271	-25.722	14.712	+41.001	-29.632
YM	1600	$2.7529 \cdot 10^{-3}$	+38.499	-25.841	15.359	+41.450	-30.061
YM	1650	$2.0259 \cdot 10^{-3}$	+38.600	-25.900	16.714	+42.063	-30.825
YM	1700	$1.5026 \cdot 10^{-3}$	+38.875	-26.031	17.409	+42.595	-31.315
YM	1750	$1.1058 \cdot 10^{-3}$	+39.038	-26.124	18.517	+43.207	-32.021
YM	1800	$8.2188 \cdot 10^{-4}$	+39.216	-26.208	19.275	+43.696	-32.533
YM	1850	$6.1264 \cdot 10^{-4}$	+39.398	-26.300	21.206	+44.743	-33.784
YM	1900	$4.5739 \cdot 10^{-4}$	+39.538	-26.373	22.438	+45.461	-34.626
YM	1950	$3.4237 \cdot 10^{-4}$	+39.627	-26.420	23.899	+46.276	-35.626
YM	2000	$2.5529 \cdot 10^{-4}$	+39.727	-26.463	25.883	+47.415	-37.017
YM	2050	$1.9229 \cdot 10^{-4}$	+39.894	-26.551	28.472	+49.012	-38.931
YM	2100	$1.4462 \cdot 10^{-4}$	+39.771	-26.496	31.465	+50.713	-41.135
YM	2150	$1.0998 \cdot 10^{-4}$	+39.812	-26.515	30.336	+50.052	-40.290
YM	2200	$8.2638 \cdot 10^{-5}$	+39.801	-26.506	39.007	+55.729	-47.160
YM	2250	$6.2760 \cdot 10^{-5}$	+39.891	-26.566	36.137	+53.826	-44.851
YM	2300	$4.7736 \cdot 10^{-5}$	+40.051	-26.646	40.029	+56.625	-48.087
YM	2400	$2.7688 \cdot 10^{-5}$	+40.071	-26.653	48.164	+62.653	-55.046
YM	2500	$1.6261 \cdot 10^{-5}$	+39.817	-26.552	54.308	+67.341	-60.452

Table 6.2: Cross sections and their uncertainties for pair production of vector leptoquarks. ‘YM’ denotes the Yang-Mills case.

## 6.2 Uncertainties in Acceptance

Another aspect of theoretical uncertainties is their impacts on the shape of variables used in the analysis. Since the change in the shape of the discriminating variables affects the acceptance values in the regions, these are checked using SimpleAnalysis and TRUTH3 samples. As in section 6.1, PDF+ $\alpha_s$  uncertainties and scale uncertainties are taken into account. Following the PDF4LHC recommendation [128], the PDF uncertainty is evaluated by the standard deviation of acceptance using replicas:

$$\delta^{\text{PDF}} a = \sqrt{\frac{1}{N_{\text{mem}} - 1} \sum_{i=1}^{N_{\text{mem}}} (a^{(i)} - \langle a \rangle)^2} \quad (6.8)$$

where the mean value of acceptance is defined as

$$\langle a \rangle = \frac{1}{N_{\text{mem}}} \sum_{i=1}^{N_{\text{mem}}} a^{(i)}. \quad (6.9)$$

While using  $\alpha_s(m_Z^2) = 0.118$  as the nominal value, its uncertainty is evaluated using two adjacent values:

$$\delta^{\alpha_s} a = \frac{a(\alpha_s = 0.119) - a(\alpha_s = 0.117)}{2}. \quad (6.10)$$

The PDF and  $\alpha_s$  uncertainties are then combined in quadrature:

$$\delta^{\text{PDF}+\alpha_s} a = \sqrt{(\delta^{\text{PDF}} a)^2 + (\delta^{\alpha_s} a)^2}. \quad (6.11)$$

Uncertainties related to renormalization and factorization scales can be evaluated using seven combinations of their values:

$$\mu_R = \{0.5, 1, 2.0\} \cdot m_{\text{LQ}}, \quad \mu_F = \{0.5, 1, 2.0\} \cdot m_{\text{LQ}} \quad (6.12)$$

excluding two combinations

$$\left\{ \begin{array}{l} \mu_R = \frac{1}{2} m_{\text{LQ}} \\ \mu_F = 2 m_{\text{LQ}} \end{array} \right\}, \quad \left\{ \begin{array}{l} \mu_R = 2 m_{\text{LQ}} \\ \mu_F = \frac{1}{2} m_{\text{LQ}} \end{array} \right\}$$

The scale uncertainty is then evaluated by taking envelope of the seven combinations. Additionally, uncertainties in parton shower and hadronization must be taken into account. Radiation uncertainty (Var3c), which is a variation of strong coupling in the initial state radiation [126], is evaluated using two additional TRUTH3 samples with ‘Var3Up’ and ‘Var3Down’, comparing their acceptance values with the nominal value. The results are summarized in table 6.3, which shows the conservative flat 20% uncertainty can be used for all signal points.

	SR (disc.)	SR (excl.)
<b><math>LQ_V^{\min}</math>, <math>m_{LQ} = 1200</math> GeV</b>		
PDF+ $\alpha_S$	$\pm 1.15$	$\pm 0.79$
Scale	+0.26  - 0.25	+0.66  - 0.63
Radiation (Var3c)	+6.10  + 0.96	+6.80  + 3.63
<b><math>LQ_V^{\min}</math>, <math>m_{LQ} = 1400</math> GeV</b>		
PDF+ $\alpha_S$	$\pm 2.69$	$\pm 1.90$
Scale	+0.41  - 0.43	+0.58  - 0.58
Radiation (Var3c)	-1.60  + 1.27	-0.85  + 0.53
<b><math>LQ_V^{\min}</math>, <math>m_{LQ} = 1600</math> GeV</b>		
PDF+ $\alpha_S$	$\pm 2.40$	$\pm 1.50$
Scale	+0.59  - 0.57	+0.63  - 0.59
Radiation (Var3c)	+1.23  - 1.26	+2.46  - 0.71
<b><math>LQ_V^{\min}</math>, <math>m_{LQ} = 1800</math> GeV</b>		
PDF+ $\alpha_S$	$\pm 5.24$	$\pm 4.38$
Scale	+0.38  - 0.37	+0.35  - 0.33
Radiation (Var3c)	+3.88  + 2.94	+4.01  + 1.57
<b><math>LQ_V^{\min}</math>, <math>m_{LQ} = 2000</math> GeV</b>		
PDF+ $\alpha_S$	$\pm 2.58$	$\pm 2.07$
Scale	+0.29  - 0.32	+0.27  - 0.27
Radiation (Var3c)	-1.88  - 0.41	-1.24  - 0.50
<b><math>LQ_V^{\min}</math>, <math>m_{LQ} = 2200</math> GeV</b>		
PDF+ $\alpha_S$	$\pm 2.43$	$\pm 2.69$
Scale	+0.38  - 0.40	+0.31  - 0.29
Radiation (Var3c)	-0.58  - 0.38	+0.19  - 0.07
<b><math>LQ_V^{YM}</math>, <math>m_{LQ} = 1200</math> GeV</b>		
PDF+ $\alpha_S$	$\pm 4.75$	$\pm 2.56$
Scale	+0.74  - 0.86	+0.52  - 0.59
Radiation (Var3c)	+5.20  + 2.72	+1.77  + 3.10
<b><math>LQ_V^{YM}</math>, <math>m_{LQ} = 1400</math> GeV</b>		
PDF+ $\alpha_S$	$\pm 3.27$	$\pm 3.17$
Scale	+0.47  - 0.55	+0.20  - 0.24
Radiation (Var3c)	+3.28  + 0.29	+2.54  + 0.23
<b><math>LQ_V^{YM}</math>, <math>m_{LQ} = 1600</math> GeV</b>		
PDF+ $\alpha_S$	$\pm 2.89$	$\pm 2.02$
Scale	+0.76  - 0.80	+0.52  - 0.55
Radiation (Var3c)	+0.87  - 1.91	+0.71  - 2.16
<b><math>LQ_V^{YM}</math>, <math>m_{LQ} = 1800</math> GeV</b>		
PDF+ $\alpha_S$	$\pm 4.41$	$\pm 3.43$
Scale	+0.64  - 0.72	+0.49  - 0.53
Radiation (Var3c)	+0.03  + 0.53	-0.43  - 0.30
<b><math>LQ_V^{YM}</math>, <math>m_{LQ} = 2000</math> GeV</b>		
PDF+ $\alpha_S$	$\pm 5.03$	$\pm 4.53$
Scale	+0.37  - 0.43	+0.31  - 0.34
Radiation (Var3c)	-1.98  - 2.37	-3.19  - 3.17
<b><math>LQ_V^{YM}</math>, <math>m_{LQ} = 2200</math> GeV</b>		
PDF+ $\alpha_S$	$\pm 5.92$	$\pm 4.00$
Scale	+0.24  - 0.28	+0.06  - 0.07
Radiation (Var3c)	-0.26  - 0.81	-0.19  - 0.39

Table 6.3: Relative uncertainties of theory systematics for several vector LQ signal points in the single-tau SRs in percent. For symmetric uncertainties one single value is given, while for asymmetric uncertainties the variations are separated by a vertical bar, where the former denominates the up and the latter the down variation.

## 7.1 Signal Contamination

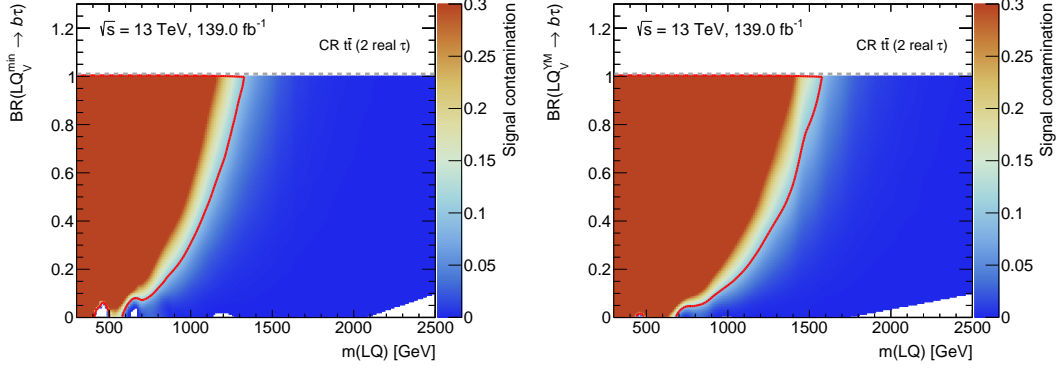
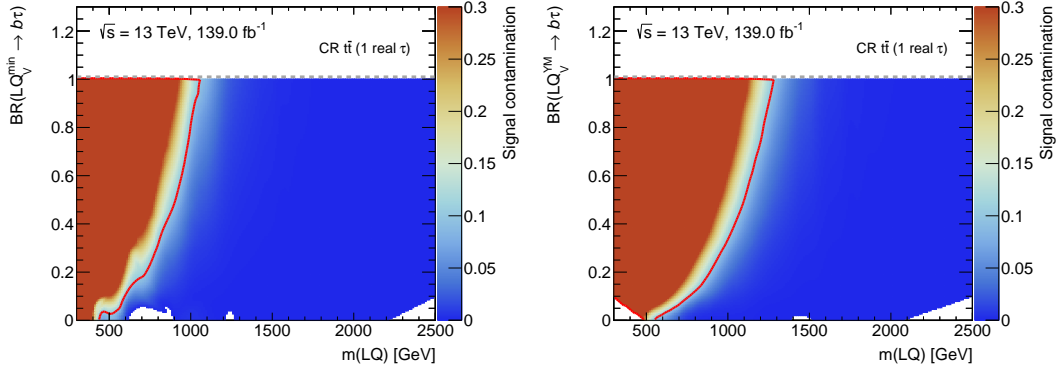
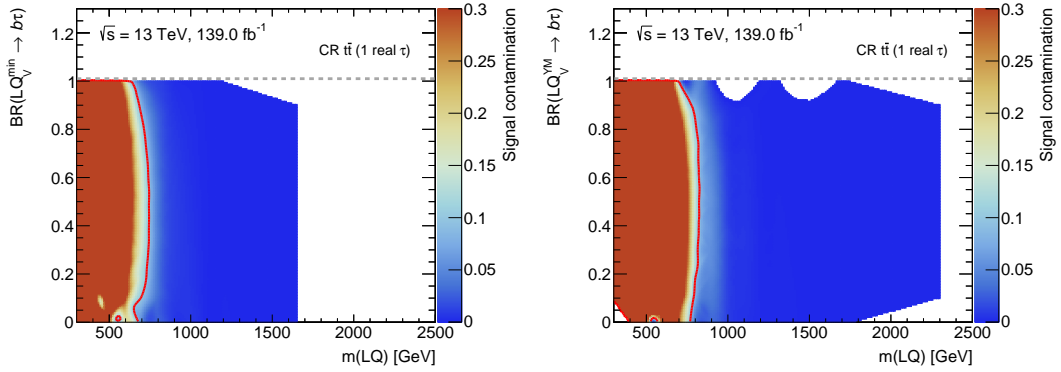
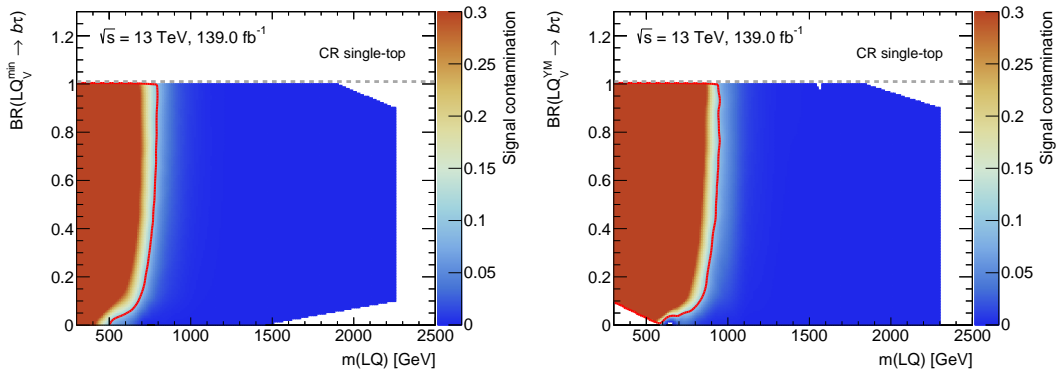
In background-only and exclusion fits, there is a potential risk that the normalization is biased by assuming the CRs and VRs to be free of any signal contribution. The number of signal events divided by the total background yields in a certain region is called the *signal contamination*. Since there has been no previous search for vector LQ for the ATLAS collaboration, signal contamination in the CRs and VRs needs to be checked. In the CRs in the di-tau channel, signal contamination is larger than 10% in a wide range of LQ masses, especially at high  $B(\text{LQ} \rightarrow b\tau)$ . The CRs in the single-tau channel are less affected by the signal contamination. In the  $t\bar{t}$  (1 real  $\tau$ ) CR, signal contamination exceeds 10% at masses up to around 750 GeV and 800 GeV for minimal coupling and Yang-Mills cases. In the single-top CR, masses up to around 800 GeV and 1000 GeV are affected for minimal coupling and Yang-Mills cases (fig. 7.1). In the VRs, the range of masses affected by the signal contamination is extended beyond 1000 GeV in the Yang-Mills case (fig. 7.2).

However, the exclusion fit takes the signal contributions into account in all regions including the CRs. Large signal contribution in the CRs may cause failures in hypothesis tests, but signal points with such a problem can be manually excluded by upper limit scans. Indeed, the upper limits on cross sections shown in fig. C.12 are far below the simulated cross sections shown in fig. 5.1 and tables 6.1 and 6.2.

Additionally, the exclusion of signal points with high signal contamination can be justified by checking the normalization factors. The normalization factors from the background-only fit in the CRs are shown in table 7.1. As neither of the factors is larger than 1, the signal yields would be very small even if the signal existed in the CRs and VRs, unless the simulated backgrounds were abnormally overestimated for some reason.

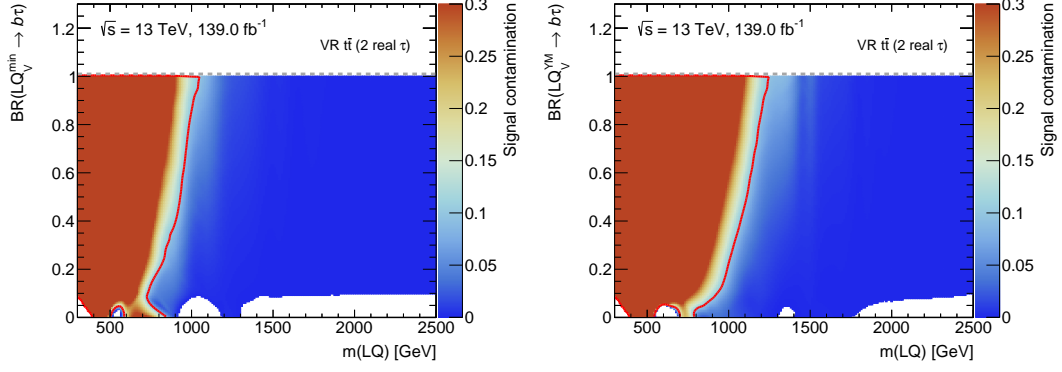
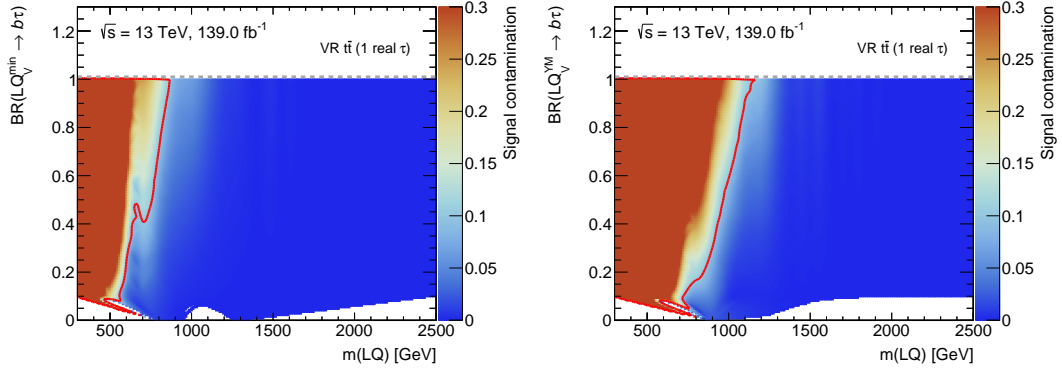
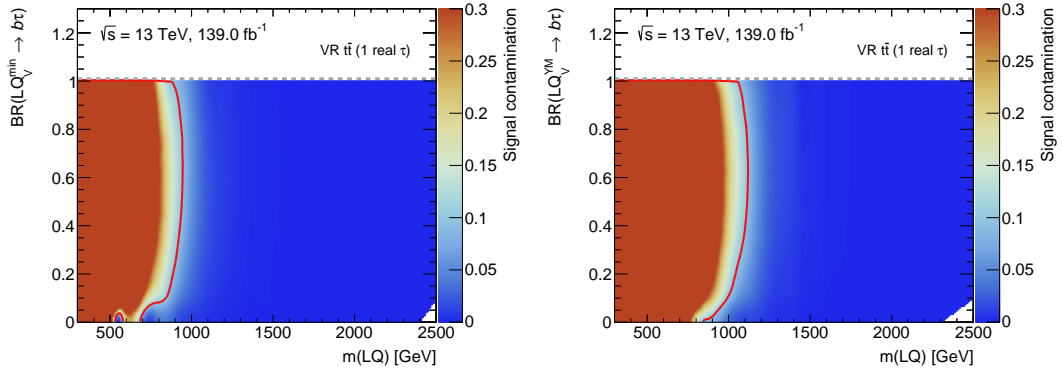
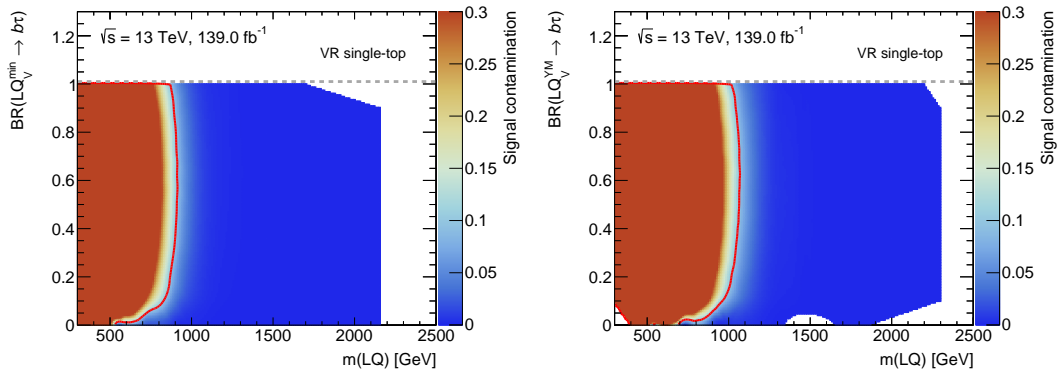
Normalization factor	Fitted value
$\mu_{t\bar{t}}$ (2 real $\tau$ )	$0.93^{+0.32}_{-0.23}$
$\mu_{t\bar{t}}$ (1 real $\tau$ )	$0.84^{+0.21}_{-0.17}$
$\mu_{\text{single-top}}$	$0.18^{+0.19}_{-0.16}$

Table 7.1: Values for the normalization factors from the background-only fit using the full set of systematic uncertainties [64].

(a) CR  $t\bar{t}$  (2 real  $\tau$ ) (di-tau)(b) CR  $t\bar{t}$  (1 real  $\tau$ ) (di-tau)(c) CR  $t\bar{t}$  (1 real  $\tau$ ) (single-tau)

(d) CR single-top (single-tau)

Figure 7.1: Signal contamination in each CR for minimal coupling (left) and Yang-Mills (right) case. Red contours indicate signal contamination of 10%.

(a) VR  $t\bar{t}$  (2 real  $\tau$ ) (di-tau)(b) VR  $t\bar{t}$  (1 real  $\tau$ ) (di-tau)(c) VR  $t\bar{t}$  (1 real  $\tau$ ) (single-tau)

(d) VR single-top (single-tau)

Figure 7.2: Signal contamination in each VR for minimal coupling (left) and Yang-Mills (right) case. Red contours indicate signal contamination of 10%.

## 7.2 Kinematic Distributions in the Signal Regions

Since the analysis is not optimized for the vector LQ, it is further checked if the configuration of the regions was also good for the vector LQ. In fig. 7.3, the variables used to define the regions are compared between the signal models, all at reco-level using the official MC samples. In the one-bin (discovery) SR, normalized distributions of  $s_T$ ,  $\sum m_T$  ( $b_{1,2}$ ) and  $m_T(\tau)$  are compared between up- and down-type scalar LQ and vector LQ in minimal coupling and Yang-Mills cases, all at  $m(\text{LQ}) = 1.2 \text{ TeV}$ . As the difference exceeds 50% for none of the variables, it also captures the characteristic kinematics of the vector LQ. Merging the three bins of the multi-bin (exclusion) SR, nominal distribution (pre-fit) of  $p_T(\tau)$  is compared between the signal and the backgrounds. The mass points of the signal models are chosen near the exclusion limit of each scenario, which will be shown in section 7.3. Since the Asimov significance ( $Z_A$ ) defined in eq. (4.1) does not show much difference between the signal models, the multi-bin SR is expected to have a similarly good acceptance for the vector-LQ interpretation.

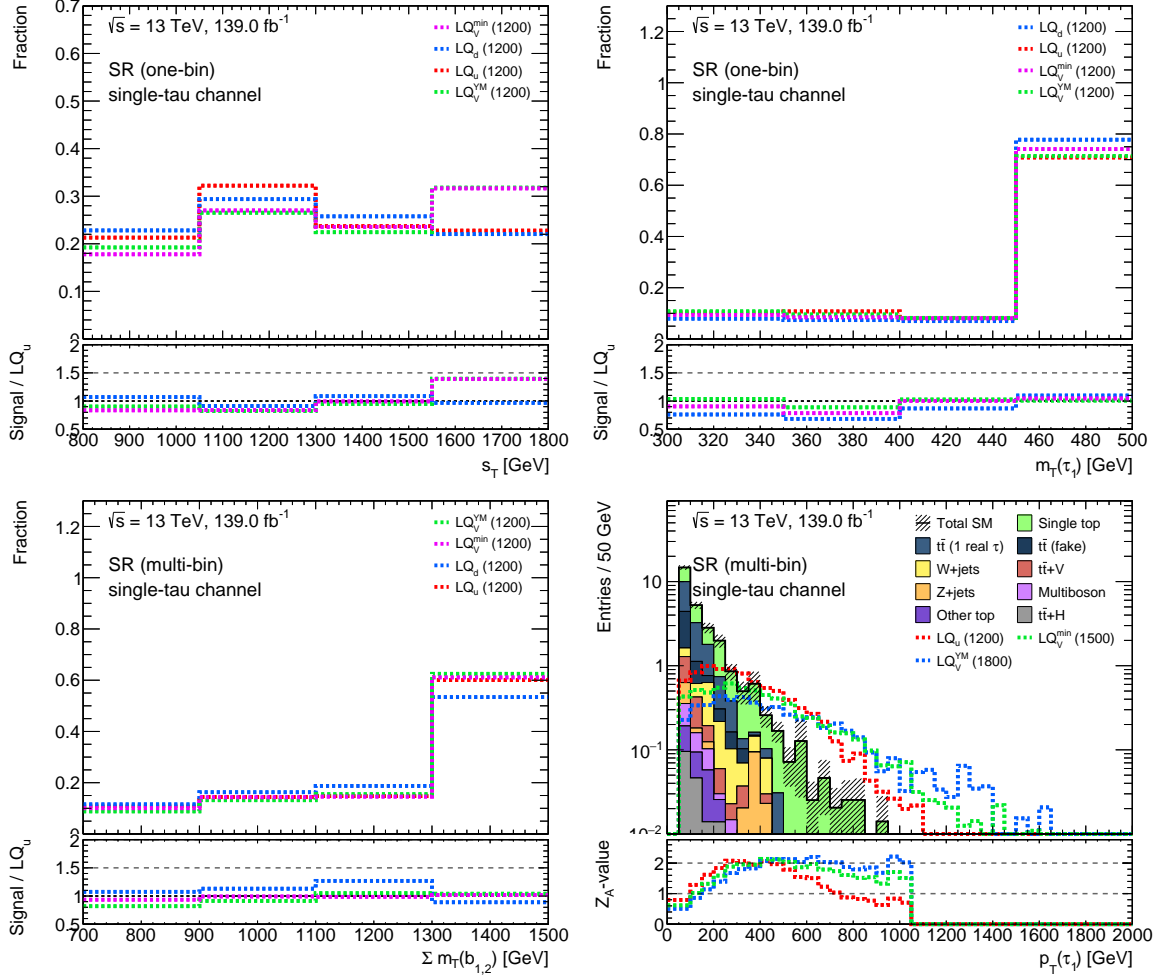


Figure 7.3: Normalized distributions of the leptoquark signals for  $s_T$  and  $m_T(\tau)$  in the single-tau one-bin SR (top) and  $\Sigma m_T(b_{1,2})$  in the single-tau  $p_T(\tau)$ -binned SR (bottom left), and distributions of leptoquark signals and background as function of  $p_T(\tau)$  in the single-tau binned SR (bottom right). The dotted lines indicate  $LQ_3^{u/d}$  and  $LQ_3^v$ . The ratio to  $LQ_3^u$  is also included except for  $p_T(\tau)$  where the significance is shown. For the  $s_T$ ,  $m_T(\tau)$  and  $\Sigma m_T(b_{1,2})$ ,  $LQ_3^{u/d}$  and  $LQ_3^v$  are compared at the same mass and the rightmost bin includes overflow. For  $p_T(\tau)$ ,  $LQ_3^{u/d}$  and  $LQ_3^v$  are compared near respective exclusion limits.

### 7.3 Exclusion Limits

The full Run-2 data taken by the ATLAS detector has shown no significant excess of events over the background expectation in the signal region [64]. Using the  $CL_s$  method described in section 4.2, limits can be set on the vector LQ in minimal coupling and Yang-Mills cases, at 95% confidence level. In the minimal coupling case, the  $U_1$  vector LQ is excluded up to around  $m(\text{LQ}) = 1.5 \text{ TeV}$  for intermediate branching ratios as shown in fig. 7.4a. As the Yang-Mills case yields larger production cross sections, the exclusion limit is increased up to around  $m(\text{LQ}) = 1.8 \text{ TeV}$  for intermediate branching ratios, as shown in fig. 7.4b. The  $CL_s$  values of the scanned signal points are listed in appendix C.2.

The analysis shows relatively low sensitivity when  $B(\text{LQ} \rightarrow b\tau)$  is small, which was the same in the scalar LQ case. For the  $U_1$  vector LQ, however, this is not a serious problem, since the theory already assumes equal couplings to charged leptons and neutrinos. Scanning over the signal strength parameter  $\mu_{\text{sig}}$  as explained in section 4.4, upper limit on the production cross section can be set on each signal point. Choosing mass points near the exclusion limits and  $B(\text{LQ} \rightarrow b\tau) = 0.5$  which is close to theoretically preferred values, the results are shown in fig. 7.5. For this value of branching ratio, the exclusion limit is between 1.75 TeV and 1.8 TeV for the Yang-Mills case and between 1.5 TeV and 1.55 TeV for the minimal coupling case. Upper limits scaled by the cross sections are summarized in appendix C.3.

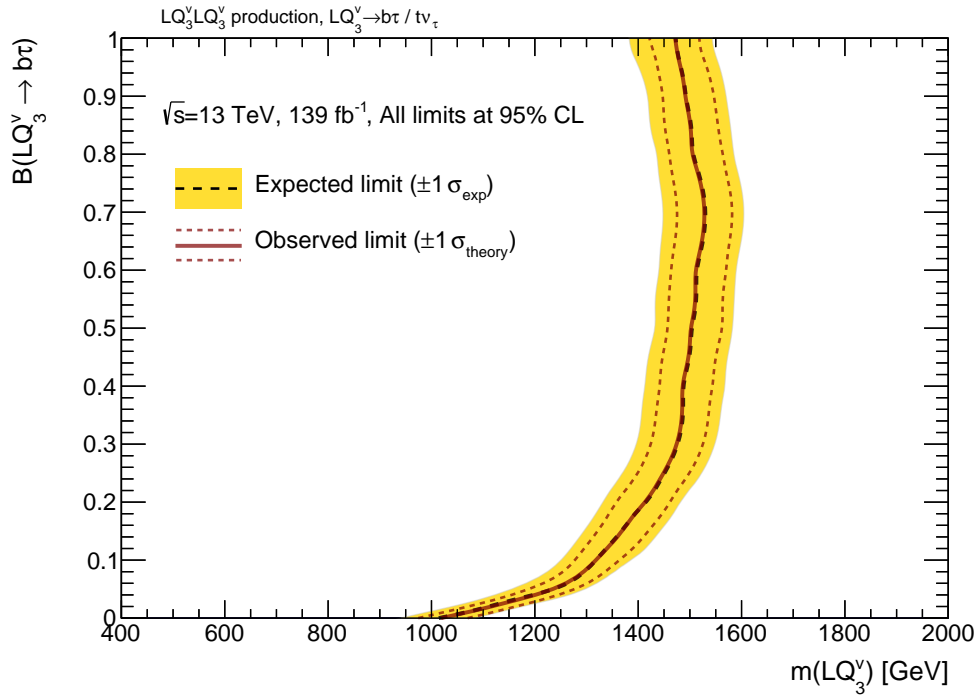
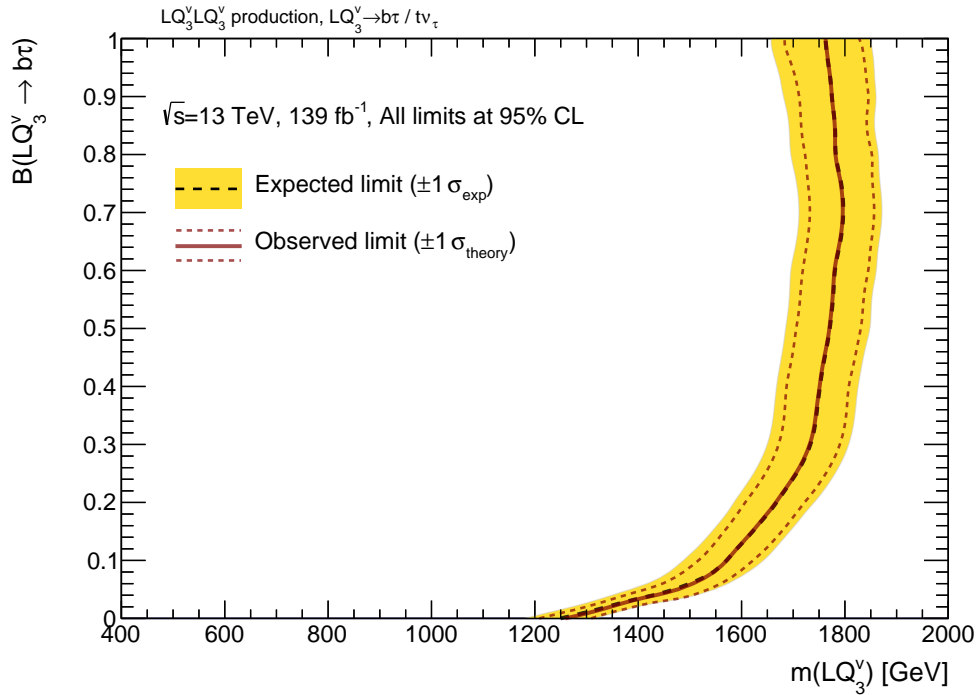
(a)  $LQ_3^y$  (minimal coupling)(b)  $LQ_3^y$  (Yang-Mills)

Figure 7.4: Expected and Observed limits for  $LQ_3^y$ , following the  $CL_s$  prescription. The black dashed lines indicate expected limits, while yellow bands indicate uncertainties. The red solid lines indicate observed limits, with red dashed lines indicating uncertainties.

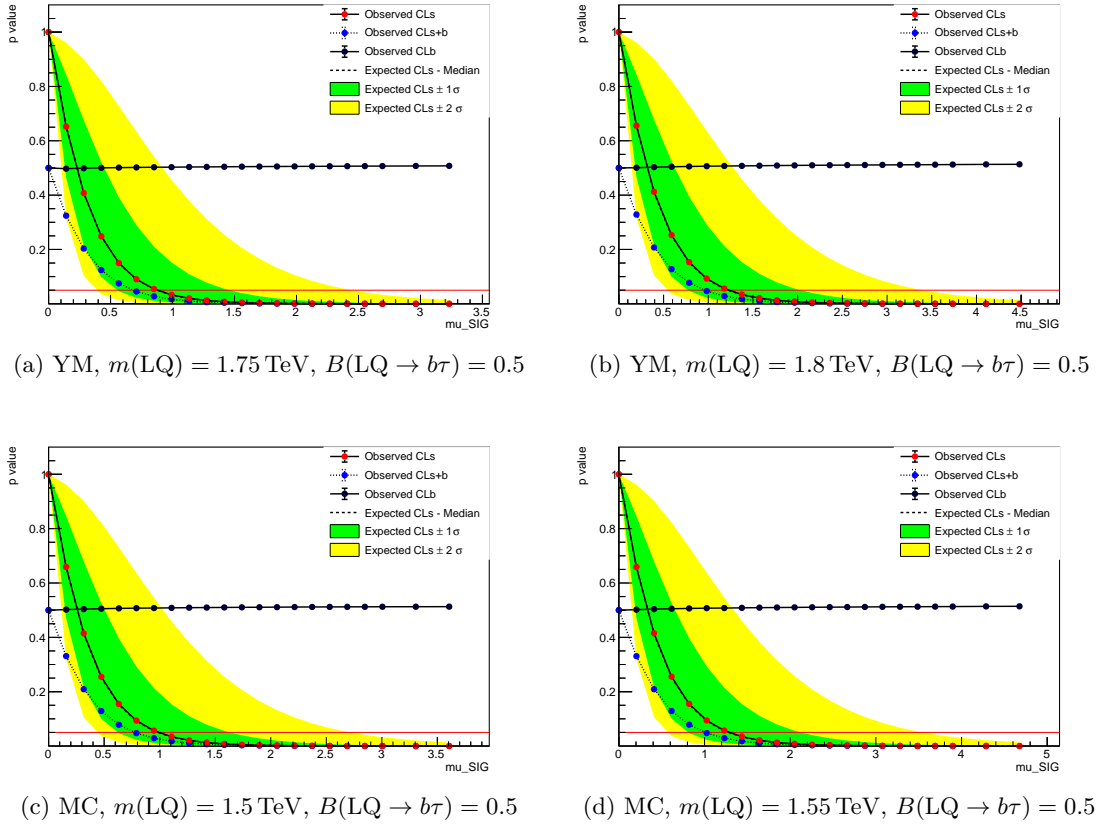


Figure 7.5: Upper limit scans for the  $U_1$  vector LQ near exclusion limits, with  $B(\text{LQ} \rightarrow b\tau) = 0.5$ . For this value of branching ratio, the exclusion limit is between 1.75 TeV and 1.8 TeV for the Yang-Mills case (YM) and between 1.5 TeV and 1.55 TeV for the minimal coupling (MC) case. The red lines indicate  $\text{CL}_s = 0.05$  which is conventionally chosen as the criterion for exclusion.

Vector leptoquark interpretation of the search for top squarks decaying via tau sleptons is presented. The analysis designed for the stop-stau and scalar LQ scenarios has shown a good sensitivity to vector LQs as well. The  $U_1$  vector LQ is excluded up to  $m(\text{LQ}) = 1.5 \text{ TeV}$  in minimal coupling case and  $m(\text{LQ}) = 1.8 \text{ TeV}$  in Yang-Mills case, both for intermediate branching ratio. Still, large range of masses remain to be excluded. For the  $U_1$  vector LQ to be able to explain all of the B-anomalies, its mass must be below  $12.5 \text{ TeV}$  [17].

Therefore there are several outlooks worth pointing out. For example, the analysis was not optimized for the vector LQ and there might be a space for further optimizations. In the di-tau CRs and VRs, a wide range of masses were affected by signal contamination. It needs to be investigated if the signal contamination can be reduced.

For simplicity, the vector LQ is assumed to couple only with left-chiral SM fermions in this thesis. In general, however, it is possible to make the LQ non-chiral by setting  $\beta_R^{33}$  comparable to  $\beta_L^{33}$ . This scenario can provide advantages in explanations for B-anomalies [15, 60]. Since the CMS searches [67, 129] have not addressed this possibility either, this case still remains unexplored.

The global coupling strength of the vector LQ was set to  $g_U = 3.0$ , while the corresponding parameter for scalar LQ has been set to  $\lambda = 0.3$ . The latter case can be certainly said to be a ‘small coupling’ case where the pair production is not affected. It needs to be checked if the former case significantly deviates from the small coupling cases and how the sensitivity further changes depending on the coupling.

Another open topic is the order of the QCD computations used in simulations. The uncertainties in production cross section of vector leptoquarks were relatively larger compared to the scalar LQ, as the simulation was at leading order. Once higher order computations become available, this would help setting more precise limits by reducing scale ( $\mu_R$  and  $\mu_F$ ) uncertainties.



- [1] H. Georgi and S. L. Glashow. “Unity of All Elementary Particle Forces”. In: *Phys. Rev. Lett.* 32 (1974), pp. 438–441. DOI: [10.1103/PhysRevLett.32.438](https://doi.org/10.1103/PhysRevLett.32.438).
- [2] J. C. Pati and A. Salam. “Lepton Number as the Fourth Color”. In: *Phys. Rev. D* 10 (1974). [Erratum: *Phys.Rev.D* 11, 703–703 (1975)], pp. 275–289. DOI: [10.1103/PhysRevD.10.275](https://doi.org/10.1103/PhysRevD.10.275).
- [3] G. Senjanovic and A. Sokorac. “Light Leptoquarks in SO(10)”. In: *Z. Phys. C* 20 (1983), p. 255. DOI: [10.1007/BF01574858](https://doi.org/10.1007/BF01574858).
- [4] S. Dimopoulos and L. Susskind. “Mass Without Scalars”. In: *Nucl. Phys. B* 155 (1979). Ed. by A. Zichichi, pp. 237–252. DOI: [10.1016/0550-3213\(79\)90364-X](https://doi.org/10.1016/0550-3213(79)90364-X).
- [5] S. Dimopoulos. “Technicolored Signatures”. In: *Nucl. Phys. B* 168 (1980). Ed. by A. Zichichi, pp. 69–92. DOI: [10.1016/0550-3213\(80\)90277-1](https://doi.org/10.1016/0550-3213(80)90277-1).
- [6] BaBar, J. P. Lees et al. “Measurement of an Excess of  $\bar{B} \rightarrow D^{(*)}\tau^{-}\bar{\nu}_{\tau}$  Decays and Implications for Charged Higgs Bosons”. In: *Phys. Rev. D* 88.7 (2013), p. 072012. DOI: [10.1103/PhysRevD.88.072012](https://doi.org/10.1103/PhysRevD.88.072012). arXiv: [1303.0571](https://arxiv.org/abs/1303.0571) [[hep-ex](#)].
- [7] Belle, M. Huschle et al. “Measurement of the branching ratio of  $\bar{B} \rightarrow D^{(*)}\tau^{-}\bar{\nu}_{\tau}$  relative to  $\bar{B} \rightarrow D^{(*)}\ell^{-}\bar{\nu}_{\ell}$  decays with hadronic tagging at Belle”. In: *Phys. Rev. D* 92.7 (2015), p. 072014. DOI: [10.1103/PhysRevD.92.072014](https://doi.org/10.1103/PhysRevD.92.072014). arXiv: [1507.03233](https://arxiv.org/abs/1507.03233) [[hep-ex](#)].
- [8] LHCb, R. Aaij et al. “Measurement of the ratio of branching fractions  $\mathcal{B}(\bar{B}^0 \rightarrow D^{*+}\tau^{-}\bar{\nu}_{\tau})/\mathcal{B}(\bar{B}^0 \rightarrow D^{*+}\mu^{-}\bar{\nu}_{\mu})$ ”. In: *Phys. Rev. Lett.* 115.11 (2015). [Erratum: *Phys.Rev.Lett.* 115, 159901 (2015)], p. 111803. DOI: [10.1103/PhysRevLett.115.111803](https://doi.org/10.1103/PhysRevLett.115.111803). arXiv: [1506.08614](https://arxiv.org/abs/1506.08614) [[hep-ex](#)].
- [9] Belle, S. Hirose et al. “Measurement of the  $\tau$  lepton polarization and  $R(D^{*})$  in the decay  $\bar{B} \rightarrow D^{*}\tau^{-}\bar{\nu}_{\tau}$ ”. In: *Phys. Rev. Lett.* 118.21 (2017), p. 211801. DOI: [10.1103/PhysRevLett.118.211801](https://doi.org/10.1103/PhysRevLett.118.211801). arXiv: [1612.00529](https://arxiv.org/abs/1612.00529) [[hep-ex](#)].
- [10] LHCb, R. Aaij et al. “Test of Lepton Flavor Universality by the measurement of the  $B^0 \rightarrow D^{*-}\tau^{+}\nu_{\tau}$  branching fraction using three-prong  $\tau$  decays”. In: *Phys. Rev. D* 97.7 (2018), p. 072013. DOI: [10.1103/PhysRevD.97.072013](https://doi.org/10.1103/PhysRevD.97.072013). arXiv: [1711.02505](https://arxiv.org/abs/1711.02505) [[hep-ex](#)].
- [11] LHCb, R. Aaij et al. “Test of lepton universality using  $B^{+} \rightarrow K^{+}\ell^{+}\ell^{-}$  decays”. In: *Phys. Rev. Lett.* 113 (2014), p. 151601. DOI: [10.1103/PhysRevLett.113.151601](https://doi.org/10.1103/PhysRevLett.113.151601). arXiv: [1406.6482](https://arxiv.org/abs/1406.6482) [[hep-ex](#)].
- [12] LHCb, R. Aaij et al. “Test of lepton universality with  $B^0 \rightarrow K^{*0}\ell^{+}\ell^{-}$  decays”. In: *JHEP* 08 (2017), p. 055. DOI: [10.1007/JHEP08\(2017\)055](https://doi.org/10.1007/JHEP08(2017)055). arXiv: [1705.05802](https://arxiv.org/abs/1705.05802) [[hep-ex](#)].

- [13] LHCb, R. Aaij et al. “Test of lepton universality in beauty-quark decays”. In: (Mar. 2021). arXiv: [2103.11769](https://arxiv.org/abs/2103.11769) [[hep-ex](#)].
- [14] W. Buchmüller, R. Rückl, and D. Wyler. “Leptoquarks in Lepton - Quark Collisions”. In: *Phys. Lett. B* 191 (1987). [Erratum: *Phys.Lett.B* 448, 320–320 (1999)], pp. 442–448. DOI: [10.1016/0370-2693\(87\)90637-X](https://doi.org/10.1016/0370-2693(87)90637-X).
- [15] M. J. Baker et al. “High- $p_T$  signatures in vector-leptoquark models”. In: *Eur. Phys. J. C* 79.4 (2019), p. 334. DOI: [10.1140/epjc/s10052-019-6853-x](https://doi.org/10.1140/epjc/s10052-019-6853-x). arXiv: [1901.10480](https://arxiv.org/abs/1901.10480) [[hep-ph](#)].
- [16] R. Barbieri et al. “Anomalies in  $B$ -decays and  $U(2)$  flavour symmetry”. In: *Eur. Phys. J. C* 76.2 (2016), p. 67. DOI: [10.1140/epjc/s10052-016-3905-3](https://doi.org/10.1140/epjc/s10052-016-3905-3). arXiv: [1512.01560](https://arxiv.org/abs/1512.01560) [[hep-ph](#)].
- [17] A. Angelescu et al. “Closing the window on single leptoquark solutions to the  $B$ -physics anomalies”. In: *JHEP* 10 (2018), p. 183. DOI: [10.1007/JHEP10\(2018\)183](https://doi.org/10.1007/JHEP10(2018)183). arXiv: [1808.08179](https://arxiv.org/abs/1808.08179) [[hep-ph](#)].
- [18] D. Griffiths. *Introduction to elementary particles*. 2008. ISBN: 978-3-527-40601-2.
- [19] D. H. Perkins. *Introduction to high energy physics*. Cambridge University Press, 2000. ISBN: 978-0-521-62196-0.
- [20] M. E. Peskin and D. V. Schroeder. *An Introduction to quantum field theory*. Reading, USA: Addison-Wesley, 1995. ISBN: 978-0-201-50397-5.
- [21] W. Hollik. “Quantum field theory and the Standard Model”. In: *2009 European School of High-Energy Physics*. Dec. 2010. arXiv: [1012.3883](https://arxiv.org/abs/1012.3883) [[hep-ph](#)].
- [22] C.-N. Yang and R. L. Mills. “Conservation of Isotopic Spin and Isotopic Gauge Invariance”. In: *Phys. Rev.* 96 (1954). Ed. by J.-P. Hsu and D. Fine, pp. 191–195. DOI: [10.1103/PhysRev.96.191](https://doi.org/10.1103/PhysRev.96.191).
- [23] M. Gell-Mann. “The Eightfold Way: A Theory of strong interaction symmetry”. In: (Mar. 1961). DOI: [10.2172/4008239](https://doi.org/10.2172/4008239).
- [24] Y. Ne’eman. “Derivation of strong interactions from a gauge invariance”. In: *Nucl. Phys.* 26 (1961). Ed. by R. Ruffini and Y. Verbin, pp. 222–229. DOI: [10.1016/0029-5582\(61\)90134-1](https://doi.org/10.1016/0029-5582(61)90134-1).
- [25] M. Gell-Mann. “A Schematic Model of Baryons and Mesons”. In: *Phys. Lett.* 8 (1964), pp. 214–215. DOI: [10.1016/S0031-9163\(64\)92001-3](https://doi.org/10.1016/S0031-9163(64)92001-3).
- [26] G. Zweig. “An  $SU(3)$  model for strong interaction symmetry and its breaking. Version 1”. In: (Jan. 1964).
- [27] G. Zweig. “An  $SU(3)$  model for strong interaction symmetry and its breaking. Version 2”. In: *DEVELOPMENTS IN THE QUARK THEORY OF HADRONS. VOL. 1. 1964 - 1978*. Ed. by D. B. Lichtenberg and S. P. Rosen. Feb. 1964.
- [28] O. W. Greenberg. “Spin and Unitary Spin Independence in a Paraquark Model of Baryons and Mesons”. In: *Phys. Rev. Lett.* 13 (1964), pp. 598–602. DOI: [10.1103/PhysRevLett.13.598](https://doi.org/10.1103/PhysRevLett.13.598).
- [29] F. Englert and R. Brout. “Broken Symmetry and the Mass of Gauge Vector Mesons”. In: *Phys. Rev. Lett.* 13 (1964). Ed. by J. C. Taylor, pp. 321–323. DOI: [10.1103/PhysRevLett.13.321](https://doi.org/10.1103/PhysRevLett.13.321).
- [30] P. W. Higgs. “Broken Symmetries and the Masses of Gauge Bosons”. In: *Phys. Rev. Lett.* 13 (1964). Ed. by J. C. Taylor, pp. 508–509. DOI: [10.1103/PhysRevLett.13.508](https://doi.org/10.1103/PhysRevLett.13.508).
- [31] G. S. Guralnik, C. R. Hagen, and T. W. B. Kibble. “Global Conservation Laws and Massless Particles”. In: *Phys. Rev. Lett.* 13 (1964). Ed. by J. C. Taylor, pp. 585–587. DOI: [10.1103/PhysRevLett.13.585](https://doi.org/10.1103/PhysRevLett.13.585).

- [32] J. Goldstone. “Field Theories with Superconductor Solutions”. In: *Nuovo Cim.* 19 (1961), pp. 154–164. DOI: [10.1007/BF02812722](https://doi.org/10.1007/BF02812722).
- [33] S. Weinberg. “A Model of Leptons”. In: *Phys. Rev. Lett.* 19 (1967), pp. 1264–1266. DOI: [10.1103/PhysRevLett.19.1264](https://doi.org/10.1103/PhysRevLett.19.1264).
- [34] S. L. Glashow. “Partial Symmetries of Weak Interactions”. In: *Nucl. Phys.* 22 (1961), pp. 579–588. DOI: [10.1016/0029-5582\(61\)90469-2](https://doi.org/10.1016/0029-5582(61)90469-2).
- [35] C. S. Wu et al. “Experimental Test of Parity Conservation in  $\beta$  Decay”. In: *Phys. Rev.* 105 (1957), pp. 1413–1414. DOI: [10.1103/PhysRev.105.1413](https://doi.org/10.1103/PhysRev.105.1413).
- [36] J. D. Bjorken and S. L. Glashow. “Elementary Particles and SU(4)”. In: *Phys. Lett.* 11 (1964), pp. 255–257. DOI: [10.1016/0031-9163\(64\)90433-0](https://doi.org/10.1016/0031-9163(64)90433-0).
- [37] S. L. Glashow, J. Iliopoulos, and L. Maiani. “Weak Interactions with Lepton-Hadron Symmetry”. In: *Phys. Rev. D* 2 (1970), pp. 1285–1292. DOI: [10.1103/PhysRevD.2.1285](https://doi.org/10.1103/PhysRevD.2.1285).
- [38] E598, J. J. Aubert et al. “Experimental Observation of a Heavy Particle  $J$ ”. In: *Phys. Rev. Lett.* 33 (1974), pp. 1404–1406. DOI: [10.1103/PhysRevLett.33.1404](https://doi.org/10.1103/PhysRevLett.33.1404).
- [39] SLAC-SP-017, J. E. Augustin et al. “Discovery of a Narrow Resonance in  $e^+e^-$  Annihilation”. In: *Phys. Rev. Lett.* 33 (1974), pp. 1406–1408. DOI: [10.1103/PhysRevLett.33.1406](https://doi.org/10.1103/PhysRevLett.33.1406).
- [40] M. Kobayashi and T. Maskawa. “CP Violation in the Renormalizable Theory of Weak Interaction”. In: *Prog. Theor. Phys.* 49 (1973), pp. 652–657. DOI: [10.1143/PTP.49.652](https://doi.org/10.1143/PTP.49.652).
- [41] S. W. Herb et al. “Observation of a Dimuon Resonance at 9.5-GeV in 400-GeV Proton-Nucleus Collisions”. In: *Phys. Rev. Lett.* 39 (1977), pp. 252–255. DOI: [10.1103/PhysRevLett.39.252](https://doi.org/10.1103/PhysRevLett.39.252).
- [42] CDF, F. Abe et al. “Observation of top quark production in  $\bar{p}p$  collisions”. In: *Phys. Rev. Lett.* 74 (1995), pp. 2626–2631. DOI: [10.1103/PhysRevLett.74.2626](https://doi.org/10.1103/PhysRevLett.74.2626). arXiv: [hep-ex/9503002](https://arxiv.org/abs/hep-ex/9503002).
- [43] D0, S. Abachi et al. “Observation of the top quark”. In: *Phys. Rev. Lett.* 74 (1995), pp. 2632–2637. DOI: [10.1103/PhysRevLett.74.2632](https://doi.org/10.1103/PhysRevLett.74.2632). arXiv: [hep-ex/9503003](https://arxiv.org/abs/hep-ex/9503003).
- [44] M. L. Perl et al. “Evidence for Anomalous Lepton Production in  $e^+e^-$  Annihilation”. In: *Phys. Rev. Lett.* 35 (1975), pp. 1489–1492. DOI: [10.1103/PhysRevLett.35.1489](https://doi.org/10.1103/PhysRevLett.35.1489).
- [45] UA1, G. Arnison et al. “Experimental Observation of Isolated Large Transverse Energy Electrons with Associated Missing Energy at  $\sqrt{s} = 540$  GeV”. In: *Phys. Lett. B* 122 (1983), pp. 103–116. DOI: [10.1016/0370-2693\(83\)91177-2](https://doi.org/10.1016/0370-2693(83)91177-2).
- [46] UA1, G. Arnison et al. “Experimental Observation of Lepton Pairs of Invariant Mass Around 95-GeV/c<sup>2</sup> at the CERN SPS Collider”. In: *Phys. Lett. B* 126 (1983), pp. 398–410. DOI: [10.1016/0370-2693\(83\)90188-0](https://doi.org/10.1016/0370-2693(83)90188-0).
- [47] C. Berger et al. “Jet analysis of the (9.46) decay into charged hadrons”. In: *Physics Letters B* 82 (1979), pp. 449–455.
- [48] TASSO, R. Brandelik et al. “Evidence for Planar Events in  $e^+e^-$  Annihilation at High-Energies”. In: *Phys. Lett. B* 86 (1979), pp. 243–249. DOI: [10.1016/0370-2693\(79\)90830-X](https://doi.org/10.1016/0370-2693(79)90830-X).
- [49] ATLAS, G. Aad et al. “Observation of a new particle in the search for the Standard Model Higgs boson with the ATLAS detector at the LHC”. In: *Phys. Lett. B* 716 (2012), pp. 1–29. DOI: [10.1016/j.physletb.2012.08.020](https://doi.org/10.1016/j.physletb.2012.08.020). arXiv: [1207.7214](https://arxiv.org/abs/1207.7214) [[hep-ex](https://arxiv.org/abs/1207.7214)].

- [50] CMS, S. Chatrchyan et al. “Observation of a New Boson at a Mass of 125 GeV with the CMS Experiment at the LHC”. In: *Phys. Lett. B* 716 (2012), pp. 30–61. DOI: [10.1016/j.physletb.2012.08.021](https://doi.org/10.1016/j.physletb.2012.08.021). arXiv: [1207.7235 \[hep-ex\]](https://arxiv.org/abs/1207.7235).
- [51] URL: [https://commons.wikimedia.org/wiki/File:Standard\\_Model\\_of\\_Elementary\\_Particles.svg](https://commons.wikimedia.org/wiki/File:Standard_Model_of_Elementary_Particles.svg) (visited on 04/30/2021).
- [52] R. N. Mohapatra and G. Senjanovic. “Neutrino Mass and Spontaneous Parity Nonconservation”. In: *Phys. Rev. Lett.* 44 (1980), p. 912. DOI: [10.1103/PhysRevLett.44.912](https://doi.org/10.1103/PhysRevLett.44.912).
- [53] Muon g-2, B. Abi et al. “Measurement of the Positive Muon Anomalous Magnetic Moment to 0.46 ppm”. In: *Phys. Rev. Lett.* 126.14 (2021), p. 141801. DOI: [10.1103/PhysRevLett.126.141801](https://doi.org/10.1103/PhysRevLett.126.141801). arXiv: [2104.03281 \[hep-ex\]](https://arxiv.org/abs/2104.03281).
- [54] S. P. Martin. “A Supersymmetry primer”. In: *Adv. Ser. Direct. High Energy Phys.* 18 (1998). Ed. by G. L. Kane, pp. 1–98. DOI: [10.1142/9789812839657\\_0001](https://doi.org/10.1142/9789812839657_0001). arXiv: [hep-ph/9709356](https://arxiv.org/abs/hep-ph/9709356).
- [55] W. de Boer. “Grand unified theories and supersymmetry in particle physics and cosmology”. In: *Prog. Part. Nucl. Phys.* 33 (1994), pp. 201–302. DOI: [10.1016/0146-6410\(94\)90045-0](https://doi.org/10.1016/0146-6410(94)90045-0). arXiv: [hep-ph/9402266](https://arxiv.org/abs/hep-ph/9402266).
- [56] B. Schrempp and F. Schrempp. “LIGHT LEPTOQUARKS”. In: *Phys. Lett. B* 153 (1985), pp. 101–107. DOI: [10.1016/0370-2693\(85\)91450-9](https://doi.org/10.1016/0370-2693(85)91450-9).
- [57] L. F. Abbott and E. Farhi. “Are the weak interactions strong?” In: *Physics Letters B* 101.1-2 (Apr. 1981), pp. 69–72. DOI: [10.1016/0370-2693\(81\)90492-5](https://doi.org/10.1016/0370-2693(81)90492-5).
- [58] G. Altarelli. “HERA data and leptoquarks in supersymmetry”. In: *Nucl. Phys. B Proc. Suppl.* 62 (1998). Ed. by A. Zichichi, pp. 3–12. DOI: [10.1016/S0920-5632\(97\)00638-5](https://doi.org/10.1016/S0920-5632(97)00638-5). arXiv: [hep-ph/9708437](https://arxiv.org/abs/hep-ph/9708437).
- [59] URL: <https://hflav-eos.web.cern.ch/hflav-eos/semi/spring19/html/RDsDsstar/RDRDs.html> (visited on 05/05/2021).
- [60] C. Cornella, J. Fuentes-Martin, and G. Isidori. “Revisiting the vector leptoquark explanation of the B-physics anomalies”. In: *JHEP* 07 (2019), p. 168. DOI: [10.1007/JHEP07\(2019\)168](https://doi.org/10.1007/JHEP07(2019)168). arXiv: [1903.11517 \[hep-ph\]](https://arxiv.org/abs/1903.11517).
- [61] B. Diaz, M. Schmaltz, and Y.-M. Zhong. “The leptoquark Hunter’s guide: Pair production”. In: *JHEP* 10 (2017), p. 097. DOI: [10.1007/JHEP10\(2017\)097](https://doi.org/10.1007/JHEP10(2017)097). arXiv: [1706.05033 \[hep-ph\]](https://arxiv.org/abs/1706.05033).
- [62] T. Mandal, S. Mitra, and S. Seth. “Pair Production of Scalar Leptoquarks at the LHC to NLO Parton Shower Accuracy”. In: *Phys. Rev. D* 93.3 (2016), p. 035018. DOI: [10.1103/PhysRevD.93.035018](https://doi.org/10.1103/PhysRevD.93.035018). arXiv: [1506.07369 \[hep-ph\]](https://arxiv.org/abs/1506.07369).
- [63] ATLAS, M. Aaboud et al. “Searches for third-generation scalar leptoquarks in  $\sqrt{s} = 13$  TeV pp collisions with the ATLAS detector”. In: *JHEP* 06 (2019), p. 144. DOI: [10.1007/JHEP06\(2019\)144](https://doi.org/10.1007/JHEP06(2019)144). arXiv: [1902.08103 \[hep-ex\]](https://arxiv.org/abs/1902.08103).
- [64] ATLAS Collaboration. *Search for new phenomena in pp collisions in final states with tau leptons, b-jets, and missing transverse momentum with the ATLAS detector*. ATLAS-CONF-2021-008. Mar. 2021. URL: <http://cdsweb.cern.ch/record/2759282>.
- [65] J. Blümlein, E. Boos, and A. Kryukov. “Leptoquark pair production in hadronic interactions”. In: *Z. Phys. C* 76 (1997), pp. 137–153. DOI: [10.1007/s002880050538](https://doi.org/10.1007/s002880050538). arXiv: [hep-ph/9610408](https://arxiv.org/abs/hep-ph/9610408).
- [66] I. Doršner et al. “Physics of leptoquarks in precision experiments and at particle colliders”. In: *Phys. Rept.* 641 (2016), pp. 1–68. DOI: [10.1016/j.physrep.2016.06.001](https://doi.org/10.1016/j.physrep.2016.06.001). arXiv: [1603.04993 \[hep-ph\]](https://arxiv.org/abs/1603.04993).

- [67] CMS, A. M. Sirunyan et al. “Search for singly and pair-produced leptoquarks coupling to third-generation fermions in proton-proton collisions at  $\sqrt{s} = 13$  TeV”. In: (Dec. 2020). arXiv: [2012.04178](https://arxiv.org/abs/2012.04178) [[hep-ex](#)].
- [68] J. D. Jackson. *Classical Electrodynamics*. Wiley, 1998. ISBN: 978-0-471-30932-1.
- [69] URL: <https://cds.cern.ch/record/2197559> (visited on 05/07/2021).
- [70] ATLAS, G. Aad et al. “The ATLAS Experiment at the CERN Large Hadron Collider”. In: *JINST* 3 (2008), S08003. DOI: [10.1088/1748-0221/3/08/S08003](https://doi.org/10.1088/1748-0221/3/08/S08003).
- [71] URL: <https://cds.cern.ch/images/CERN-GE-0803012-01> (visited on 05/07/2021).
- [72] ATLAS, A. R. Martínez. “The Run-2 ATLAS Trigger System”. In: *J. Phys. Conf. Ser.* 762.1 (2016). Ed. by L. Salinas and C. Torres, p. 012003. DOI: [10.1088/1742-6596/762/1/012003](https://doi.org/10.1088/1742-6596/762/1/012003).
- [73] ATLAS, M. Aaboud et al. “Electron reconstruction and identification in the ATLAS experiment using the 2015 and 2016 LHC proton-proton collision data at  $\sqrt{s} = 13$  TeV”. In: *Eur. Phys. J. C* 79.8 (2019), p. 639. DOI: [10.1140/epjc/s10052-019-7140-6](https://doi.org/10.1140/epjc/s10052-019-7140-6). arXiv: [1902.04655](https://arxiv.org/abs/1902.04655) [[physics.ins-det](#)].
- [74] ATLAS, G. Aad et al. “Electron and photon performance measurements with the ATLAS detector using the 2015–2017 LHC proton-proton collision data”. In: *JINST* 14.12 (2019), P12006. DOI: [10.1088/1748-0221/14/12/P12006](https://doi.org/10.1088/1748-0221/14/12/P12006). arXiv: [1908.00005](https://arxiv.org/abs/1908.00005) [[hep-ex](#)].
- [75] ATLAS, G. Aad et al. “Muon reconstruction performance of the ATLAS detector in proton–proton collision data at  $\sqrt{s} = 13$  TeV”. In: *Eur. Phys. J. C* 76.5 (2016), p. 292. DOI: [10.1140/epjc/s10052-016-4120-y](https://doi.org/10.1140/epjc/s10052-016-4120-y). arXiv: [1603.05598](https://arxiv.org/abs/1603.05598) [[hep-ex](#)].
- [76] M. Cacciari, G. P. Salam, and G. Soyez. “The anti- $k_t$  jet clustering algorithm”. In: *JHEP* 04 (2008), p. 063. DOI: [10.1088/1126-6708/2008/04/063](https://doi.org/10.1088/1126-6708/2008/04/063). arXiv: [0802.1189](https://arxiv.org/abs/0802.1189) [[hep-ph](#)].
- [77] ATLAS Collaboration. *Selection of jets produced in 13 TeV proton–proton collisions with the ATLAS detector*. ATLAS-CONF-2015-029. 2015. URL: <https://cds.cern.ch/record/2037702>.
- [78] ATLAS Collaboration. *Tagging and suppression of pileup jets with the ATLAS detector*. ATLAS-CONF-2014-018. 2014. URL: <https://cds.cern.ch/record/1700870>.
- [79] ATLAS Collaboration. *Optimisation and performance studies of the ATLAS b-tagging algorithms for the 2017-18 LHC run*. ATL-PHYS-PUB-2017-013. 2017. URL: <https://cds.cern.ch/record/2273281>.
- [80] ATLAS, G. Aad et al. “Topological cell clustering in the ATLAS calorimeters and its performance in LHC Run 1”. In: *Eur. Phys. J. C* 77 (2017), p. 490. DOI: [10.1140/epjc/s10052-017-5004-5](https://doi.org/10.1140/epjc/s10052-017-5004-5). arXiv: [1603.02934](https://arxiv.org/abs/1603.02934) [[hep-ex](#)].
- [81] ATLAS, G. Aad et al. “Identification and energy calibration of hadronically decaying tau leptons with the ATLAS experiment in  $pp$  collisions at  $\sqrt{s}=8$  TeV”. In: *Eur. Phys. J. C* 75.7 (2015), p. 303. DOI: [10.1140/epjc/s10052-015-3500-z](https://doi.org/10.1140/epjc/s10052-015-3500-z). arXiv: [1412.7086](https://arxiv.org/abs/1412.7086) [[hep-ex](#)].
- [82] ATLAS Collaboration. *Measurement of the tau lepton reconstruction and identification performance in the ATLAS experiment using  $pp$  collisions at  $\sqrt{s} = 13$  TeV*. ATLAS-CONF-2017-029. 2017. URL: <https://cds.cern.ch/record/2261772>.
- [83] ATLAS Collaboration. *Identification of hadronic tau lepton decays using neural networks in the ATLAS experiment*. ATL-PHYS-PUB-2019-033. 2019. URL: <https://cds.cern.ch/record/2688062>.

- [84] ATLAS, G. Aad et al. “ATLAS data quality operations and performance for 2015–2018 data-taking”. In: *JINST* 15.04 (2020), P04003. DOI: [10.1088/1748-0221/15/04/P04003](https://doi.org/10.1088/1748-0221/15/04/P04003). arXiv: [1911.04632](https://arxiv.org/abs/1911.04632) [[physics.ins-det](#)].
- [85] A. Alloul et al. “FeynRules 2.0 - A complete toolbox for tree-level phenomenology”. In: *Comput. Phys. Commun.* 185 (2014), pp. 2250–2300. DOI: [10.1016/j.cpc.2014.04.012](https://doi.org/10.1016/j.cpc.2014.04.012). arXiv: [1310.1921](https://arxiv.org/abs/1310.1921) [[hep-ph](#)].
- [86] C. Degrande et al. “UFO - The Universal FeynRules Output”. In: *Comput. Phys. Commun.* 183 (2012), pp. 1201–1214. DOI: [10.1016/j.cpc.2012.01.022](https://doi.org/10.1016/j.cpc.2012.01.022). arXiv: [1108.2040](https://arxiv.org/abs/1108.2040) [[hep-ph](#)].
- [87] URL: <https://feynrules.irmp.ucl.ac.be/wiki/LeptoQuark> (visited on 05/10/2021).
- [88] J. Alwall et al. “The automated computation of tree-level and next-to-leading order differential cross sections, and their matching to parton shower simulations”. In: *JHEP* 07 (2014), p. 079. DOI: [10.1007/JHEP07\(2014\)079](https://doi.org/10.1007/JHEP07(2014)079). arXiv: [1405.0301](https://arxiv.org/abs/1405.0301) [[hep-ph](#)].
- [89] A. Buckley et al. “LHAPDF6: parton density access in the LHC precision era”. In: *Eur. Phys. J. C* 75 (2015), p. 132. DOI: [10.1140/epjc/s10052-015-3318-8](https://doi.org/10.1140/epjc/s10052-015-3318-8). arXiv: [1412.7420](https://arxiv.org/abs/1412.7420) [[hep-ph](#)].
- [90] NNPDF, R. D. Ball et al. “Parton distributions for the LHC Run II”. In: *JHEP* 04 (2015), p. 040. DOI: [10.1007/JHEP04\(2015\)040](https://doi.org/10.1007/JHEP04(2015)040). arXiv: [1410.8849](https://arxiv.org/abs/1410.8849) [[hep-ph](#)].
- [91] P. Artoisenet et al. “Automatic spin-entangled decays of heavy resonances in Monte Carlo simulations”. In: *JHEP* 03 (2013), p. 015. DOI: [10.1007/JHEP03\(2013\)015](https://doi.org/10.1007/JHEP03(2013)015). arXiv: [1212.3460](https://arxiv.org/abs/1212.3460) [[hep-ph](#)].
- [92] J. Alwall et al. “Computing decay rates for new physics theories with FeynRules and MadGraph 5\_aMC@NLO”. In: *Comput. Phys. Commun.* 197 (2015), pp. 312–323. DOI: [10.1016/j.cpc.2015.08.031](https://doi.org/10.1016/j.cpc.2015.08.031). arXiv: [1402.1178](https://arxiv.org/abs/1402.1178) [[hep-ph](#)].
- [93] T. Sjöstrand et al. “An introduction to PYTHIA 8.2”. In: *Comput. Phys. Commun.* 191 (2015), pp. 159–177. DOI: [10.1016/j.cpc.2015.01.024](https://doi.org/10.1016/j.cpc.2015.01.024). arXiv: [1410.3012](https://arxiv.org/abs/1410.3012) [[hep-ph](#)].
- [94] R. D. Ball et al. “Parton distributions with LHC data”. In: *Nucl. Phys. B* 867 (2013), pp. 244–289. DOI: [10.1016/j.nuclphysb.2012.10.003](https://doi.org/10.1016/j.nuclphysb.2012.10.003). arXiv: [1207.1303](https://arxiv.org/abs/1207.1303) [[hep-ph](#)].
- [95] ATLAS Collaboration. *ATLAS Pythia 8 tunes to 7 TeV data*. ATL-PHYS-PUB-2014-021. 2014. URL: <https://cds.cern.ch/record/1966419>.
- [96] D. J. Lange. “The EvtGen particle decay simulation package”. In: *Nucl. Instrum. Meth. A* 462 (2001). Ed. by S. Erhan, P. Schlein, and Y. Rozen, pp. 152–155. DOI: [10.1016/S0168-9002\(01\)00089-4](https://doi.org/10.1016/S0168-9002(01)00089-4).
- [97] S. Frixione, P. Nason, and G. Ridolfi. “A Positive-weight next-to-leading-order Monte Carlo for heavy flavour hadroproduction”. In: *JHEP* 09 (2007), p. 126. DOI: [10.1088/1126-6708/2007/09/126](https://doi.org/10.1088/1126-6708/2007/09/126). arXiv: [0707.3088](https://arxiv.org/abs/0707.3088) [[hep-ph](#)].
- [98] P. Nason. “A New method for combining NLO QCD with shower Monte Carlo algorithms”. In: *JHEP* 11 (2004), p. 040. DOI: [10.1088/1126-6708/2004/11/040](https://doi.org/10.1088/1126-6708/2004/11/040). arXiv: [hep-ph/0409146](https://arxiv.org/abs/hep-ph/0409146).
- [99] S. Frixione, P. Nason, and C. Oleari. “Matching NLO QCD computations with Parton Shower simulations: the POWHEG method”. In: *JHEP* 11 (2007), p. 070. DOI: [10.1088/1126-6708/2007/11/070](https://doi.org/10.1088/1126-6708/2007/11/070). arXiv: [0709.2092](https://arxiv.org/abs/0709.2092) [[hep-ph](#)].
- [100] S. Alioli et al. “A general framework for implementing NLO calculations in shower Monte Carlo programs: the POWHEG BOX”. In: *JHEP* 06 (2010), p. 043. DOI: [10.1007/JHEP06\(2010\)043](https://doi.org/10.1007/JHEP06(2010)043). arXiv: [1002.2581](https://arxiv.org/abs/1002.2581) [[hep-ph](#)].

- [101] M. Czakon and A. Mitov. “Top++: A Program for the Calculation of the Top-Pair Cross-Section at Hadron Colliders”. In: *Comput. Phys. Commun.* 185 (2014), p. 2930. DOI: [10.1016/j.cpc.2014.06.021](https://doi.org/10.1016/j.cpc.2014.06.021). arXiv: [1112.5675 \[hep-ph\]](https://arxiv.org/abs/1112.5675).
- [102] E. Re. “Single-top Wt-channel production matched with parton showers using the POWHEG method”. In: *Eur. Phys. J. C* 71 (2011), p. 1547. DOI: [10.1140/epjc/s10052-011-1547-z](https://doi.org/10.1140/epjc/s10052-011-1547-z). arXiv: [1009.2450 \[hep-ph\]](https://arxiv.org/abs/1009.2450).
- [103] M. Aliev et al. “HATHOR: HAdronic Top and Heavy quarks crOss section calculatoR”. In: *Comput. Phys. Commun.* 182 (2011), pp. 1034–1046. DOI: [10.1016/j.cpc.2010.12.040](https://doi.org/10.1016/j.cpc.2010.12.040). arXiv: [1007.1327 \[hep-ph\]](https://arxiv.org/abs/1007.1327).
- [104] P. Kant et al. “HatHor for single top-quark production: Updated predictions and uncertainty estimates for single top-quark production in hadronic collisions”. In: *Comput. Phys. Commun.* 191 (2015), pp. 74–89. DOI: [10.1016/j.cpc.2015.02.001](https://doi.org/10.1016/j.cpc.2015.02.001). arXiv: [1406.4403 \[hep-ph\]](https://arxiv.org/abs/1406.4403).
- [105] N. Kidonakis. “Two-loop soft anomalous dimensions for single top quark associated production with a  $W^-$  or  $H^-$ ”. In: *Phys. Rev. D* 82 (2010), p. 054018. DOI: [10.1103/PhysRevD.82.054018](https://doi.org/10.1103/PhysRevD.82.054018). arXiv: [1005.4451 \[hep-ph\]](https://arxiv.org/abs/1005.4451).
- [106] N. Kidonakis. “Top Quark Production”. In: *Helmholtz International Summer School on Physics of Heavy Quarks and Hadrons*. Nov. 2013. DOI: [10.3204/DESY-PROC-2013-03/Kidonakis](https://doi.org/10.3204/DESY-PROC-2013-03/Kidonakis). arXiv: [1311.0283 \[hep-ph\]](https://arxiv.org/abs/1311.0283).
- [107] Sherpa, E. Bothmann et al. “Event Generation with Sherpa 2.2”. In: *SciPost Phys.* 7.3 (2019), p. 034. DOI: [10.21468/SciPostPhys.7.3.034](https://doi.org/10.21468/SciPostPhys.7.3.034). arXiv: [1905.09127 \[hep-ph\]](https://arxiv.org/abs/1905.09127).
- [108] C. Anastasiou et al. “High precision QCD at hadron colliders: Electroweak gauge boson rapidity distributions at NNLO”. In: *Phys. Rev. D* 69 (2004), p. 094008. DOI: [10.1103/PhysRevD.69.094008](https://doi.org/10.1103/PhysRevD.69.094008). arXiv: [hep-ph/0312266](https://arxiv.org/abs/hep-ph/0312266).
- [109] T. Gleisberg and S. Hoeche. “Comix, a new matrix element generator”. In: *JHEP* 12 (2008), p. 039. DOI: [10.1088/1126-6708/2008/12/039](https://doi.org/10.1088/1126-6708/2008/12/039). arXiv: [0808.3674 \[hep-ph\]](https://arxiv.org/abs/0808.3674).
- [110] S. Schumann and F. Krauss. “A Parton shower algorithm based on Catani-Seymour dipole factorisation”. In: *JHEP* 03 (2008), p. 038. DOI: [10.1088/1126-6708/2008/03/038](https://doi.org/10.1088/1126-6708/2008/03/038). arXiv: [0709.1027 \[hep-ph\]](https://arxiv.org/abs/0709.1027).
- [111] ATLAS Collaboration. *Multi-Boson Simulation for 13 TeV ATLAS Analyses*. ATL-PHYS-PUB-2017-005. 2017. URL: <https://cds.cern.ch/record/2261933>.
- [112] ATLAS Collaboration. *Modelling of the  $t\bar{t}H$  and  $t\bar{t}V$  ( $V = W, Z$ ) processes for  $\sqrt{s} = 13$  TeV ATLAS analyses*. ATL-PHYS-PUB-2016-005. 2016. URL: <https://cds.cern.ch/record/2120826>.
- [113] H. B. Hartanto et al. “Higgs boson production in association with top quarks in the POWHEG BOX”. In: *Phys. Rev. D* 91.9 (2015), p. 094003. DOI: [10.1103/PhysRevD.91.094003](https://doi.org/10.1103/PhysRevD.91.094003). arXiv: [1501.04498 \[hep-ph\]](https://arxiv.org/abs/1501.04498).
- [114] W. Buttinger and M. Lefebvre. *Formulae for Estimating Significance*. Tech. rep. ATL-COM-GEN-2018-026. Geneva: CERN, Oct. 2018. URL: <https://cds.cern.ch/record/2643488>.
- [115] C. G. Lester and D. J. Summers. “Measuring masses of semiinvisibly decaying particles pair produced at hadron colliders”. In: *Phys. Lett. B* 463 (1999), pp. 99–103. DOI: [10.1016/S0370-2693\(99\)00945-4](https://doi.org/10.1016/S0370-2693(99)00945-4). arXiv: [hep-ph/9906349](https://arxiv.org/abs/hep-ph/9906349).
- [116] C. G. Lester and B. Nachman. “Bisection-based asymmetric  $M_{T2}$  computation: a higher precision calculator than existing symmetric methods”. In: *JHEP* 03 (2015), p. 100. DOI: [10.1007/JHEP03\(2015\)100](https://doi.org/10.1007/JHEP03(2015)100). arXiv: [1411.4312 \[hep-ph\]](https://arxiv.org/abs/1411.4312).

- [117] A. L. Read. “Modified frequentist analysis of search results (The CL(s) method)”. In: *Workshop on Confidence Limits*. Aug. 2000.
- [118] A. L. Read. “Presentation of search results: The CL(s) technique”. In: *J. Phys. G* 28 (2002). Ed. by M. R. Whalley and L. Lyons, pp. 2693–2704. DOI: [10.1088/0954-3899/28/10/313](https://doi.org/10.1088/0954-3899/28/10/313).
- [119] S. Dittmaier and M. Schumacher. “The Higgs Boson in the Standard Model - From LEP to LHC: Expectations, Searches, and Discovery of a Candidate”. In: *Prog. Part. Nucl. Phys.* 70 (2013), pp. 1–54. DOI: [10.1016/j.pnpnp.2013.02.001](https://doi.org/10.1016/j.pnpnp.2013.02.001). arXiv: [1211.4828](https://arxiv.org/abs/1211.4828) [hep-ph].
- [120] M. Baak et al. “HistFitter software framework for statistical data analysis”. In: *Eur. Phys. J. C* 75 (2015), p. 153. DOI: [10.1140/epjc/s10052-015-3327-7](https://doi.org/10.1140/epjc/s10052-015-3327-7). arXiv: [1410.1280](https://arxiv.org/abs/1410.1280) [hep-ex].
- [121] J. A. Grifols and A. Mendez. “Pair Production of Colored Hypermesons at Very High-energy”. In: *Phys. Rev. D* 26 (1982), p. 324. DOI: [10.1103/PhysRevD.26.324](https://doi.org/10.1103/PhysRevD.26.324).
- [122] S. Dawson, E. Eichten, and C. Quigg. “Search for Supersymmetric Particles in Hadron - Hadron Collisions”. In: *Phys. Rev. D* 31 (1985), p. 1581. DOI: [10.1103/PhysRevD.31.1581](https://doi.org/10.1103/PhysRevD.31.1581).
- [123] A. Czarnecki, J. G. Korner, and J. H. Piclum. “Helicity fractions of W bosons from top quark decays at NNLO in QCD”. In: *Phys. Rev. D* 81 (2010), p. 111503. DOI: [10.1103/PhysRevD.81.111503](https://doi.org/10.1103/PhysRevD.81.111503). arXiv: [1005.2625](https://arxiv.org/abs/1005.2625) [hep-ph].
- [124] ATLAS, G. Aad et al. “Measurement of the W boson polarization in top quark decays with the ATLAS detector”. In: *JHEP* 06 (2012), p. 088. DOI: [10.1007/JHEP06\(2012\)088](https://doi.org/10.1007/JHEP06(2012)088). arXiv: [1205.2484](https://arxiv.org/abs/1205.2484) [hep-ex].
- [125] G. H. Stark et al. *SimpleAnalysis: Truth-level Analysis Framework*. Tech. rep. Geneva: CERN, Apr. 2021. URL: <https://cds.cern.ch/record/2764422>.
- [126] ATLAS TWiki. *PMG Systematic Uncertainty Recipes*. 2019. URL: <https://twiki.cern.ch/twiki/bin/view/AtlasProtected/PmgSystematicUncertaintyRecipes> (visited on 04/28/2021).
- [127] ATLAS TWiki. *Leptoquarks Cluster*. 2020. URL: <https://twiki.cern.ch/twiki/bin/viewauth/AtlasProtected/LeptoquarksCluster> (visited on 04/28/2020).
- [128] J. Butterworth et al. “PDF4LHC recommendations for LHC Run II”. In: *J. Phys. G* 43 (2016), p. 023001. DOI: [10.1088/0954-3899/43/2/023001](https://doi.org/10.1088/0954-3899/43/2/023001). arXiv: [1510.03865](https://arxiv.org/abs/1510.03865) [hep-ph].
- [129] CMS, A. M. Sirunyan et al. “Constraints on models of scalar and vector leptoquarks decaying to a quark and a neutrino at  $\sqrt{s} = 13$  TeV”. In: *Phys. Rev. D* 98.3 (2018), p. 032005. DOI: [10.1103/PhysRevD.98.032005](https://doi.org/10.1103/PhysRevD.98.032005). arXiv: [1805.10228](https://arxiv.org/abs/1805.10228) [hep-ex].

## APPENDIX A

### LIST OF SIGNAL SAMPLES

The signal MC samples used in this thesis are listed in tables [A.1](#) and [A.2](#). The tables show the Dataset ID (DSID) of each signal, the type of the vector LQ (minimal coupling or Yang-Mills), the mass of the LQ and the sample's name. The sample names are referred to as 'physicsShort' in the ATLAS software framework, where the MC generator information and the physical process are summarized. For example, 'MGPY8EG' means that these samples were generated using MADGRAPH5, PYTHIA 8 and EVTGEN. The remaining parts represent the pair production of the  $U_1$  leptoquarks in the minimal coupling or Yang-Mills case, with  $\beta_L^{33} = 1.0$  and the LQ mass given in the last part. The tables also include the pair production cross sections and uncertainties computed as described in section [6.1](#), as well as theoretical branching ratios into charged leptons computed using eq. [\(5.16\)](#).

DSID	type	mass [GeV]	physicsShort	$\sigma$ [pb]	rel. unc. [%]	$\hat{B}_{cl}$
502723	min	300	MGPY8EG_U1_Pair_min_bL33_1p0_M300	94.408289	+26.1 -18.3	0.656231
502724	min	400	MGPY8EG_U1_Pair_min_bL33_1p0_M400	17.843761	+26.9 -18.9	0.579828
502725	min	500	MGPY8EG_U1_Pair_min_bL33_1p0_M500	4.556913	+27.6 -19.5	0.548845
502726	min	600	MGPY8EG_U1_Pair_min_bL33_1p0_M600	1.405636	+28.5 -20.3	0.533160
502727	min	700	MGPY8EG_U1_Pair_min_bL33_1p0_M700	0.496898	+29.3 -21.0	0.524084
502728	min	800	MGPY8EG_U1_Pair_min_bL33_1p0_M800	0.192855	+30.3 -21.9	0.518343
502729	min	900	MGPY8EG_U1_Pair_min_bL33_1p0_M900	0.080880	+31.1 -22.6	0.514475
502730	min	1000	MGPY8EG_U1_Pair_min_bL33_1p0_M1000	0.035659	+32.1 -23.4	0.511742
502731	min	1100	MGPY8EG_U1_Pair_min_bL33_1p0_M1100	0.016647	+33.1 -24.4	0.509738
502732	min	1200	MGPY8EG_U1_Pair_min_bL33_1p0_M1200	0.008046	+34.1 -25.3	0.508224
502733	min	1300	MGPY8EG_U1_Pair_min_bL33_1p0_M1300	0.003974	+35.2 -26.2	0.507051
502734	min	1400	MGPY8EG_U1_Pair_min_bL33_1p0_M1400	0.002036	+36.2 -27.3	0.506125
502735	min	1450	MGPY8EG_U1_Pair_min_bL33_1p0_M1450	0.001474	+36.6 -27.6	0.505733
502736	min	1500	MGPY8EG_U1_Pair_min_bL33_1p0_M1500	0.001062	+37.4 -28.3	0.505380
502737	min	1550	MGPY8EG_U1_Pair_min_bL33_1p0_M1550	0.000771	+38.1 -29.1	0.505061
502738	min	1600	MGPY8EG_U1_Pair_min_bL33_1p0_M1600	0.000561	+38.9 -29.9	0.504771
502739	min	1650	MGPY8EG_U1_Pair_min_bL33_1p0_M1650	0.000413	+39.3 -30.2	0.504508
502740	min	1700	MGPY8EG_U1_Pair_min_bL33_1p0_M1700	0.000302	+40.4 -31.4	0.504268
502741	min	1750	MGPY8EG_U1_Pair_min_bL33_1p0_M1750	0.000223	+40.8 -31.8	0.504049
502742	min	1800	MGPY8EG_U1_Pair_min_bL33_1p0_M1800	0.000166	+41.5 -32.5	0.503848
502743	min	1850	MGPY8EG_U1_Pair_min_bL33_1p0_M1850	0.000123	+42.6 -33.7	0.503663
502744	min	1900	MGPY8EG_U1_Pair_min_bL33_1p0_M1900	0.000091	+43.5 -34.6	0.503492
502745	min	1950	MGPY8EG_U1_Pair_min_bL33_1p0_M1950	0.000068	+44.7 -36.1	0.503335
502746	min	2000	MGPY8EG_U1_Pair_min_bL33_1p0_M2000	0.000051	+46.0 -37.5	0.503189
502747	min	2050	MGPY8EG_U1_Pair_min_bL33_1p0_M2050	0.000038	+47.9 -39.7	0.503054
502748	min	2100	MGPY8EG_U1_Pair_min_bL33_1p0_M2100	0.000029	+47.5 -39.1	0.502928
502749	min	2150	MGPY8EG_U1_Pair_min_bL33_1p0_M2150	0.000022	+49.6 -41.5	0.502812
502750	min	2200	MGPY8EG_U1_Pair_min_bL33_1p0_M2200	0.000016	+51.7 -43.9	0.502703
502751	min	2250	MGPY8EG_U1_Pair_min_bL33_1p0_M2250	0.000012	+54.5 -47.0	0.502601
502752	min	2300	MGPY8EG_U1_Pair_min_bL33_1p0_M2300	0.000009	+56.9 -49.8	0.502506
502753	min	2400	MGPY8EG_U1_Pair_min_bL33_1p0_M2400	0.000005	+64.2 -57.9	0.502334
502754	min	2500	MGPY8EG_U1_Pair_min_bL33_1p0_M2500	0.000003	+68.4 -62.5	0.502182

Table A.1: List of signal samples with DSID, type, mass, physicsShort, cross section, relative uncertainty and theoretical branching ratio to charged leptons. ‘min’ denotes the minimal coupling case.

DSID	type	mass [GeV]	physicsShort	$\sigma$ [pb]	rel. unc. [%]	$\hat{B}_{cl}$
502755	YM	300	MGPY8EG_U1_Pair_YM_bL33_1p0_M300	339.703233	+30.9 -21.8	0.656231
502756	YM	400	MGPY8EG_U1_Pair_YM_bL33_1p0_M400	68.768831	+32.1 -22.5	0.579828
502757	YM	500	MGPY8EG_U1_Pair_YM_bL33_1p0_M500	18.463368	+33.0 -23.1	0.548845
502758	YM	600	MGPY8EG_U1_Pair_YM_bL33_1p0_M600	5.923428	+33.8 -23.6	0.533160
502759	YM	700	MGPY8EG_U1_Pair_YM_bL33_1p0_M700	2.154186	+34.6 -24.2	0.524084
502760	YM	800	MGPY8EG_U1_Pair_YM_bL33_1p0_M800	0.855073	+35.2 -24.6	0.518343
502761	YM	900	MGPY8EG_U1_Pair_YM_bL33_1p0_M900	0.365366	+35.9 -25.2	0.514475
502762	YM	1000	MGPY8EG_U1_Pair_YM_bL33_1p0_M1000	0.164826	+36.6 -25.7	0.511742
502763	YM	1100	MGPY8EG_U1_Pair_YM_bL33_1p0_M1100	0.077747	+37.2 -26.2	0.509738
502764	YM	1200	MGPY8EG_U1_Pair_YM_bL33_1p0_M1200	0.037974	+38.1 -27.0	0.508224
502765	YM	1300	MGPY8EG_U1_Pair_YM_bL33_1p0_M1300	0.019083	+38.9 -27.6	0.507051
502766	YM	1400	MGPY8EG_U1_Pair_YM_bL33_1p0_M1400	0.009852	+39.7 -28.3	0.506125
502767	YM	1450	MGPY8EG_U1_Pair_YM_bL33_1p0_M1450	0.007124	+40.1 -28.8	0.505733
502768	YM	1500	MGPY8EG_U1_Pair_YM_bL33_1p0_M1500	0.005173	+40.8 -29.5	0.505380
502769	YM	1550	MGPY8EG_U1_Pair_YM_bL33_1p0_M1550	0.003779	+41.0 -29.6	0.505061
502770	YM	1600	MGPY8EG_U1_Pair_YM_bL33_1p0_M1600	0.002753	+41.4 -30.1	0.504771
502771	YM	1650	MGPY8EG_U1_Pair_YM_bL33_1p0_M1650	0.002026	+42.1 -30.8	0.504508
502772	YM	1700	MGPY8EG_U1_Pair_YM_bL33_1p0_M1700	0.001503	+42.6 -31.3	0.504268
502773	YM	1750	MGPY8EG_U1_Pair_YM_bL33_1p0_M1750	0.001106	+43.2 -32.0	0.504049
502774	YM	1800	MGPY8EG_U1_Pair_YM_bL33_1p0_M1800	0.000822	+43.7 -32.5	0.503848
502775	YM	1850	MGPY8EG_U1_Pair_YM_bL33_1p0_M1850	0.000613	+44.7 -33.8	0.503663
502776	YM	1900	MGPY8EG_U1_Pair_YM_bL33_1p0_M1900	0.000457	+45.5 -34.6	0.503492
502777	YM	1950	MGPY8EG_U1_Pair_YM_bL33_1p0_M1950	0.000342	+46.3 -35.6	0.503335
502778	YM	2000	MGPY8EG_U1_Pair_YM_bL33_1p0_M2000	0.000255	+47.4 -37.0	0.503189
502779	YM	2050	MGPY8EG_U1_Pair_YM_bL33_1p0_M2050	0.000192	+49.0 -38.9	0.503054
502780	YM	2100	MGPY8EG_U1_Pair_YM_bL33_1p0_M2100	0.000145	+50.7 -41.1	0.502928
502781	YM	2150	MGPY8EG_U1_Pair_YM_bL33_1p0_M2150	0.000110	+50.1 -40.3	0.502812
502782	YM	2200	MGPY8EG_U1_Pair_YM_bL33_1p0_M2200	0.000083	+55.7 -47.2	0.502703
502783	YM	2250	MGPY8EG_U1_Pair_YM_bL33_1p0_M2250	0.000063	+53.8 -44.9	0.502601
502784	YM	2300	MGPY8EG_U1_Pair_YM_bL33_1p0_M2300	0.000048	+56.6 -48.1	0.502506
502785	YM	2400	MGPY8EG_U1_Pair_YM_bL33_1p0_M2400	0.000028	+62.7 -55.0	0.502334
502786	YM	2500	MGPY8EG_U1_Pair_YM_bL33_1p0_M2500	0.000016	+67.3 -60.5	0.502182

Table A.2: List of signal samples with DSID, type, mass, physicsShort, cross section, relative uncertainty and theoretical branching ratio to charged leptons. ‘YM’ denotes the Yang-Mills case.



In this chapter, eqs. (5.6) and (5.10) are derived.

## B.1 Decay Width of Scalar Leptoquarks

To obtain the decay width formula, one should first write down the matrix element of the diagram. The Yukawa term of a scalar LQ coupling to a right-chiral quark  $q$  and a left-chiral lepton  $l$  is

$$\Delta\mathcal{L} = y_{ql}\phi\bar{q}_R l_L, \quad (\text{B.1})$$

where  $\phi$  denotes the scalar LQ. This term is analogous to the Yukawa coupling of the Higgs field in eq. (1.55). The LQ decays into a quark and an antilepton, as shown in fig. B.1.

The corresponding matrix element of this decay is

$$i\mathcal{M} = iy_{ql}\bar{u}(p_1) \left( \frac{1-\gamma_5}{2} \right) v(p_2) \quad (\text{B.2})$$

where  $p_1$  and  $p_2$  denote the four-momenta of the quark and the antilepton as shown in fig. B.1. Following the commonly used convention,  $\bar{u}$  and  $v$  represent the outgoing fermion (i.e. the quark) and the outgoing antifermion (i.e. the antilepton), respectively. For Dirac fermions the following completeness relations hold:

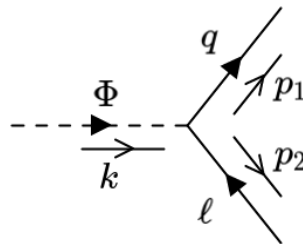


Figure B.1: Decay of a leptoquark into a quark and an antilepton. The LQ is denoted by  $\Phi$ .

$$\sum_{\text{spins}} u^s(p)\bar{u}^s(p) = \not{p} + m \quad (\text{B.3})$$

$$\sum_{\text{spins}} v^s(p)\bar{v}^s(p) = \not{p} - m. \quad (\text{B.4})$$

As the scalar LQ has only one spin state, it suffices to sum over all spins of the final state particles to obtain the unpolarized decay width. Using eqs. (B.3) and (B.4) and the trace technology, this can be simplified as follows:

$$\begin{aligned} \sum_{\text{spins}} |\mathcal{M}|^2 &= \sum_{s_1, s_2} |y_{ql}|^2 \left[ \bar{u}(p_1) \left( \frac{1 - \gamma_5}{2} \right) v(p_2) \right] \left[ \bar{u}(p_1) \left( \frac{1 - \gamma_5}{2} \right) v(p_2) \right]^* \\ &= \sum_{s_1, s_2} |y_{ql}|^2 \left[ \bar{u}(p_1) \left( \frac{1 - \gamma_5}{2} \right) v(p_2) \right] \left[ \bar{v}(p_2) \left( \frac{1 + \gamma_5}{2} \right) u(p_1) \right] \\ &= \sum_{s_1} |y_{ql}|^2 \bar{u}(p_1) \left( \frac{1 - \gamma_5}{2} \right) (\not{p}_2 - m_l) \left( \frac{1 + \gamma_5}{2} \right) u(p_1) \\ &= \sum_{s_1} |y_{ql}|^2 \text{Tr} \left[ \left( \frac{1 - \gamma_5}{2} \right) (\not{p}_2 - m_l) \left( \frac{1 + \gamma_5}{2} \right) u(p_1)\bar{u}(p_1) \right] \\ &= |y_{ql}|^2 \text{Tr} \left[ \left( \frac{1 - \gamma_5}{2} \right) (\not{p}_2 - m_l) \left( \frac{1 + \gamma_5}{2} \right) (\not{p}_1 + m_q) \right]. \end{aligned} \quad (\text{B.5})$$

Here,  $s_1$  and  $s_2$  denote the spin states of the quark and the antilepton respectively. Using the trace theorems [18, 20], the trace in eq. (B.5) becomes

$$\begin{aligned} &\text{Tr} \left[ \left( \frac{1 - \gamma_5}{2} \right) (\not{p}_2 - m_l) \left( \frac{1 + \gamma_5}{2} \right) (\not{p}_1 + m_q) \right] \\ &= \frac{1}{2} \text{Tr} (\not{p}_2 \not{p}_1) + \frac{m_q}{2} \text{Tr} \not{p}_2 + \frac{m_q}{2} \text{Tr} (\not{p}_2 \gamma_5) \\ &= 2(p_1 \cdot p_2). \end{aligned} \quad (\text{B.6})$$

Since eq. (B.6) is Lorentz-invariant, it suffices to compute the momenta in the LQ rest frame. In the LQ rest frame, the four-momenta of the LQ and its decay products are

$$\begin{aligned} k &= (m_{\text{LQ}}, 0, 0, 0) \\ p_1 &= (\sqrt{m_q^2 + p^2}, 0, 0, p) \\ p_2 &= (\sqrt{m_l^2 + p^2}, 0, 0, -p). \end{aligned}$$

By conservation of energy,

$$m_{\text{LQ}} = \sqrt{m_q^2 + p^2} + \sqrt{m_l^2 + p^2}.$$

Solving this equation for  $p$ ,

$$p^2 = \frac{m_{\text{LQ}}^4 + m_q^4 + m_l^4 - 2m_{\text{LQ}}^2 m_q^2 - 2m_{\text{LQ}}^2 m_l^2 - 2m_q^2 m_l^2}{4m_{\text{LQ}}^2}$$

and this yields useful results such as

$$k \cdot p_1 = m_{\text{LQ}} \sqrt{m_q^2 + p^2} = \frac{m_{\text{LQ}}^2 + m_q^2 - m_l^2}{2} \quad (\text{B.7})$$

$$k \cdot p_2 = m_{\text{LQ}} \sqrt{m_l^2 + p^2} = \frac{m_{\text{LQ}}^2 + m_l^2 - m_q^2}{2} \quad (\text{B.8})$$

$$\begin{aligned} p_1 \cdot p_2 &= \frac{k \cdot p_1}{m_{\text{LQ}}} \frac{k \cdot p_2}{m_{\text{LQ}}} + p^2 = \frac{2m_{\text{LQ}}^4 - 2m_{\text{LQ}}^2 m_q^2 - 2m_{\text{LQ}}^2 m_l^2}{4m_{\text{LQ}}^2} \\ &= \frac{m_{\text{LQ}}^2 - m_q^2 - m_l^2}{2} \end{aligned} \quad (\text{B.9})$$

which will be used in the next section as well.

In general, width for a two-body decay in the rest frame of the mother particle is

$$\begin{aligned} \Gamma(A \rightarrow BC) &= \frac{\sqrt{m_A^4 + m_B^4 + m_C^4 - 2m_A^2 m_B^2 - 2m_A^2 m_C^2 - 2m_B^2 m_C^2}}{16\pi S m_A^3} \\ &\quad \times |\mathcal{M}(A \rightarrow BC)|^2 \end{aligned} \quad (\text{B.10})$$

where  $S$  denotes the multiplicity of identical particles in the final state. For the decay of a leptoquark,  $S = 1$ . Inserting eq. (B.9) to eq. (B.10), the decay width of a scalar LQ is

$$\begin{aligned} \Gamma(\text{LQ} \rightarrow ql) &= |y_{ql}|^2 \frac{\sqrt{m_{\text{LQ}}^4 + m_q^4 + m_l^4 - 2m_{\text{LQ}}^2 m_q^2 - 2m_{\text{LQ}}^2 m_l^2 - 2m_q^2 m_l^2}}{16\pi m_{\text{LQ}}^3} \\ &\quad \times (m_{\text{LQ}}^2 - m_q^2 - m_l^2). \end{aligned}$$

For a scalar LQ coupling to a left-chiral quark and a right-chiral lepton, eq. (B.1) is replaced with

$$\Delta\mathcal{L} = y_{ql} \phi \bar{q}_L l_R,$$

and eq. (B.2) with

$$i\mathcal{M} = iy_{ql} \bar{u}(p_1) \left( \frac{1 + \gamma_5}{2} \right) v(p_2).$$

The spin summation in eq. (B.5) is replaced with

$$\sum_{\text{spins}} |\mathcal{M}|^2 = |y_{ql}|^2 \text{Tr} \left[ \left( \frac{1 + \gamma_5}{2} \right) (\not{p}_2 - m_l) \left( \frac{1 - \gamma_5}{2} \right) (\not{p}_1 + m_q) \right]$$

which can be shown to yield the same result. Therefore, the decay width does not depend on the chiral property of the scalar LQ.

## B.2 Decay Width of Vector Leptoquarks

For a vector LQ, the coupling term with a left-chiral quark and a left-chiral lepton is

$$\Delta\mathcal{L} = y_{ql} V_\mu \bar{q}_L \gamma^\mu l_L$$

where  $V$  denotes the vector LQ. This term is analogous to eqs. (1.50) and (1.51), neglecting the difference between quarks and leptons. In this case, the matrix element corresponding to fig. B.1 is

$$i\mathcal{M} = iy_{ql}\epsilon_\mu(k)\bar{u}(p_1)\gamma^\mu\left(\frac{1-\gamma_5}{2}\right)v(p_2)$$

where  $\epsilon_\mu$  is the polarization vector of the vector LQ and  $k$  is its four-momentum. As the vector LQ has three initial spin states, the unpolarized decay width requires averaging over all initial spin states as well as a summation over all final spin states. For massive vector bosons the following completeness relation holds:

$$\sum_{\text{spins}} \epsilon_\mu(k)\epsilon_\nu^\dagger(k) = -g_{\mu\nu} + \frac{k_\mu k_\nu}{m^2}, \quad (\text{B.11})$$

where  $k$  denotes the four-momentum of the vector boson. Using eqs. (B.3), (B.4) and (B.11), the unpolarized  $|\mathcal{M}|^2$  can be simplified as follows:

$$\begin{aligned} \frac{1}{3} \sum_{\text{spins}} |\mathcal{M}|^2 &= \sum_{s_1, s_2, r} \frac{|y_{ql}|^2}{3} \left[ \epsilon_\mu(k)\bar{u}(p_1)\gamma^\mu\left(\frac{1-\gamma_5}{2}\right)v(p_2) \right] \left[ \epsilon_\nu(k)\bar{u}(p_1)\gamma^\nu\left(\frac{1-\gamma_5}{2}\right)v(p_2) \right]^* \\ &= \sum_{s_1, s_2, r} \frac{|y_{ql}|^2}{3} \left[ \epsilon_\mu(k)\bar{u}(p_1)\gamma^\mu\left(\frac{1-\gamma_5}{2}\right)v(p_2) \right] \left[ \bar{v}(p_2)\left(\frac{1+\gamma_5}{2}\right)\gamma^\nu u(p_1)\epsilon_\nu(k)^\dagger \right] \\ &= \sum_{s_1, r} \frac{|y_{ql}|^2}{3} \left[ \epsilon_\mu(k)\bar{u}(p_1)\gamma^\mu\left(\frac{1-\gamma_5}{2}\right)(\not{p}_2 - m_l)\left(\frac{1+\gamma_5}{2}\right)\gamma^\nu u(p_1)\epsilon_\nu(k)^\dagger \right] \\ &= \sum_{s_1, r} \frac{|y_{ql}|^2}{3} \epsilon_\mu(k) \text{Tr} \left[ \gamma^\mu\left(\frac{1-\gamma_5}{2}\right)(\not{p}_2 - m_l)\left(\frac{1+\gamma_5}{2}\right)\gamma^\nu u(p_1)\bar{u}(p_1) \right] \epsilon_\nu(k)^\dagger \\ &= \sum_r \frac{|y_{ql}|^2}{3} \epsilon_\mu(k) \text{Tr} \left[ \gamma^\mu\left(\frac{1-\gamma_5}{2}\right)(\not{p}_2 - m_l)\left(\frac{1+\gamma_5}{2}\right)\gamma^\nu(\not{p}_1 + m_q) \right] \epsilon_\nu(k)^\dagger \\ &= \frac{|y_{ql}|^2}{3} \left( -g_{\mu\nu} + \frac{k_\mu k_\nu}{m_{\text{LQ}}^2} \right) \text{Tr} \left[ \gamma^\mu\left(\frac{1-\gamma_5}{2}\right)(\not{p}_2 - m_l)\left(\frac{1+\gamma_5}{2}\right)\gamma^\nu(\not{p}_1 + m_q) \right] \\ &= \frac{|y_{ql}|^2}{3} \left( -g_{\mu\nu} + \frac{k_\mu k_\nu}{m_{\text{LQ}}^2} \right) \text{Tr} \left[ \gamma^\mu\left(\frac{1-\gamma_5}{2}\right)(\not{p}_2 - m_l)\gamma^\nu\left(\frac{1-\gamma_5}{2}\right)(\not{p}_1 + m_q) \right], \end{aligned} \quad (\text{B.12})$$

where  $s_1$ ,  $s_2$  and  $r$  denote the spin states of the quark, the lepton and the vector LQ respectively. Rearranging the terms in the square bracket and using the trace theorems [18, 20], eq. (B.12) is further simplified:

$$\begin{aligned} \frac{1}{3} \sum_{\text{spins}} |\mathcal{M}|^2 &= \frac{|y_{ql}|^2}{3} \left( -g_{\mu\nu} + \frac{k_\mu k_\nu}{m_{\text{LQ}}^2} \right) 2(p_1^\mu p_2^\nu - g^{\mu\nu}(p_1 \cdot p_2) + p_2^\mu p_1^\nu) \\ &= \frac{2}{3} |y_{ql}|^2 \left( p_1 \cdot p_2 + 2 \frac{(k \cdot p_1)(k \cdot p_2)}{m_{\text{LQ}}^2} \right), \end{aligned} \quad (\text{B.13})$$

which is also Lorentz-invariant. Inserting eqs. (B.7) to (B.9) to eq. (B.13), The unpolarized  $|\mathcal{M}|^2$  is finally obtained:

$$\frac{1}{3} \sum_{\text{spins}} |\mathcal{M}|^2 = \frac{|y_{ql}|^2}{3} \frac{2m_{\text{LQ}}^4 - m_l^4 - m_q^4 + 2m_l^2 m_q^2 - m_{\text{LQ}}^2 m_l^2 - m_{\text{LQ}}^2 m_q^2}{m_{\text{LQ}}^2}. \quad (\text{B.14})$$

Inserting eq. (B.14) to eq. (B.10), the decay width of a vector LQ is

$$\begin{aligned} \Gamma(\text{LQ}_V \rightarrow ql) = & |y_{ql}|^2 \frac{\sqrt{m_{\text{LQ}}^4 + m_q^4 + m_l^4 - 2(m_{\text{LQ}}^2 m_q^2 + m_{\text{LQ}}^2 m_l^2 + m_q^2 m_l^2)}}{48\pi m_{\text{LQ}}^3} \\ & \times \frac{2m_{\text{LQ}}^4 - m_q^4 - m_l^4 - m_{\text{LQ}}^2 m_q^2 - m_{\text{LQ}}^2 m_l^2 + 2m_q^2 m_l^2}{m_{\text{LQ}}^2}. \end{aligned}$$

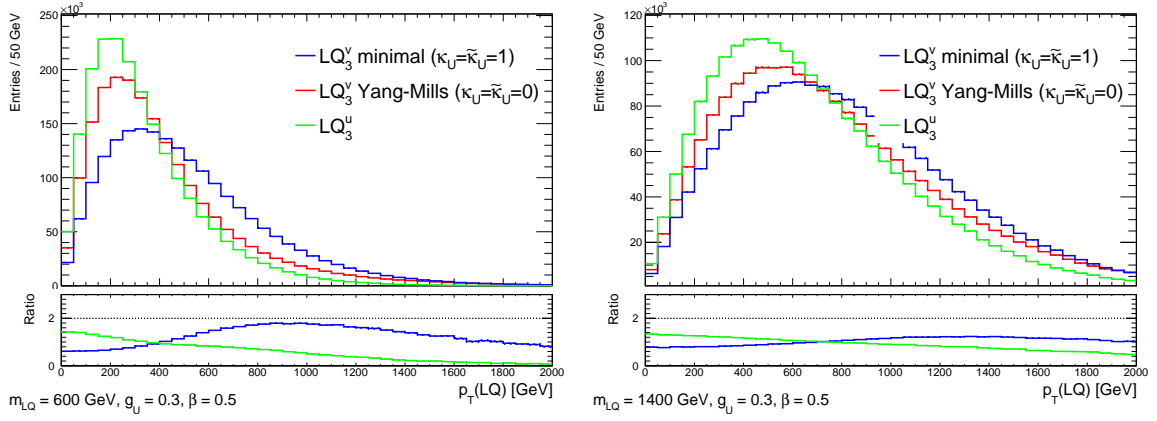
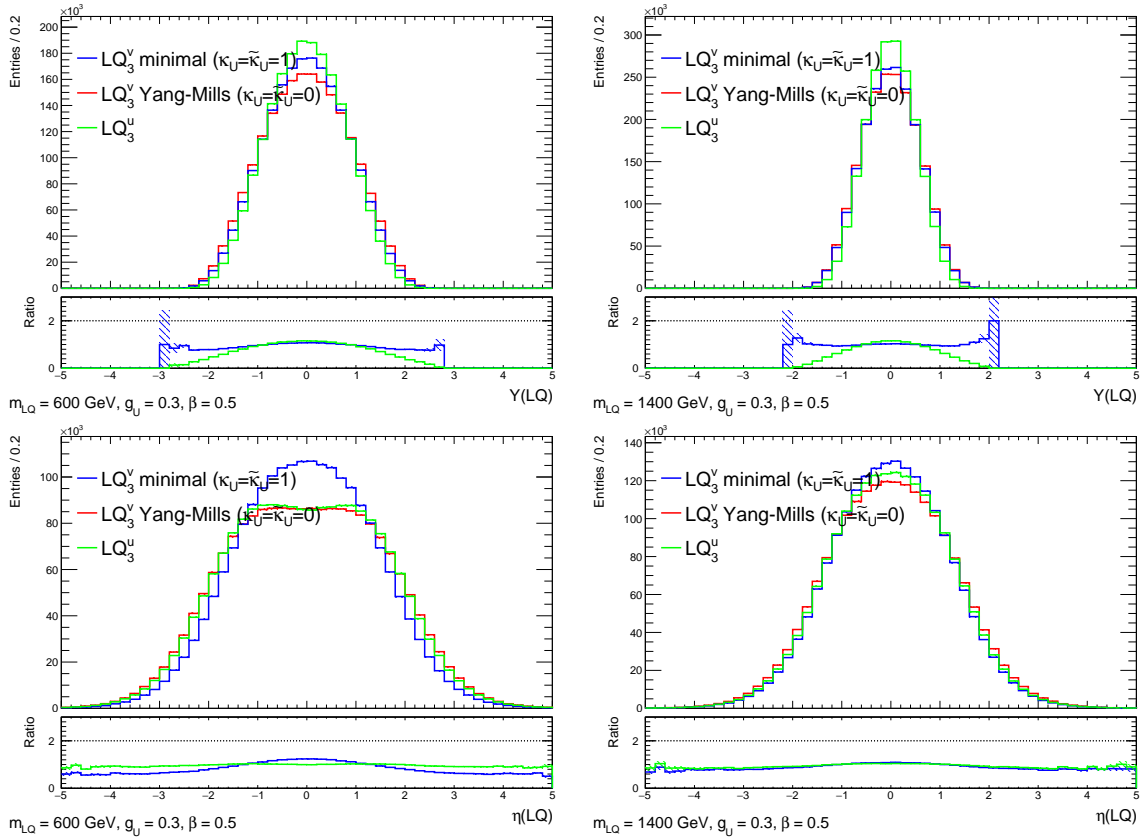


## APPENDIX C

### ADDITIONAL PLOTS

#### C.1 Kinematics

Kinematic distributions discussed in section 5.3 are shown in figs. C.1 to C.8, at different mass points. Kinematic variables defining the SRs are shown in figs. C.9 and C.10 at additional mass points.

Figure C.1: Comparison of  $p_T(\text{LQ})$  between scalar LQ and vector LQ at different mass pointsFigure C.2: Comparison of rapidity ( $Y$ ) and pseudorapidity ( $\eta$ ) between scalar LQ and vector LQ at different mass points

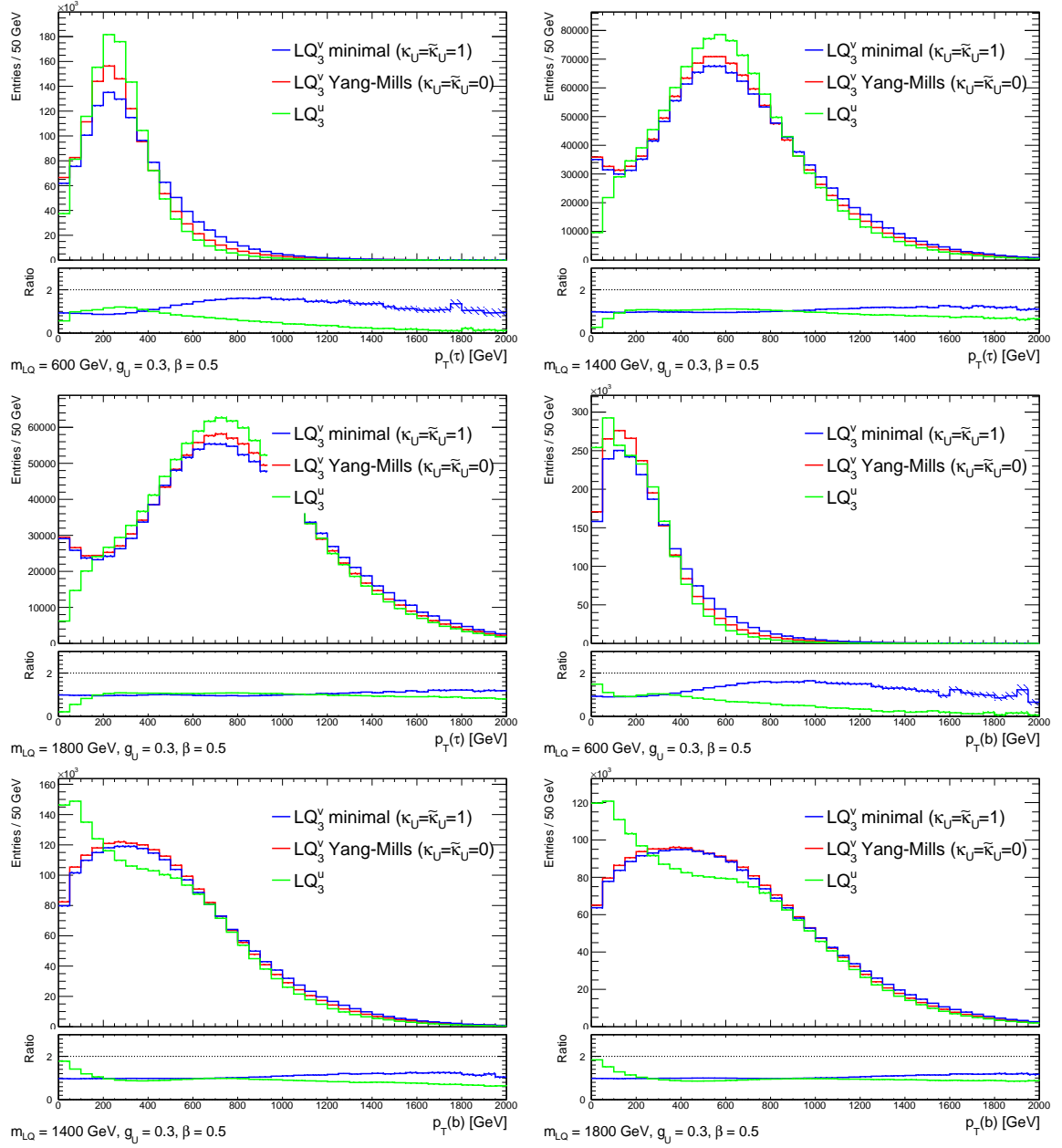
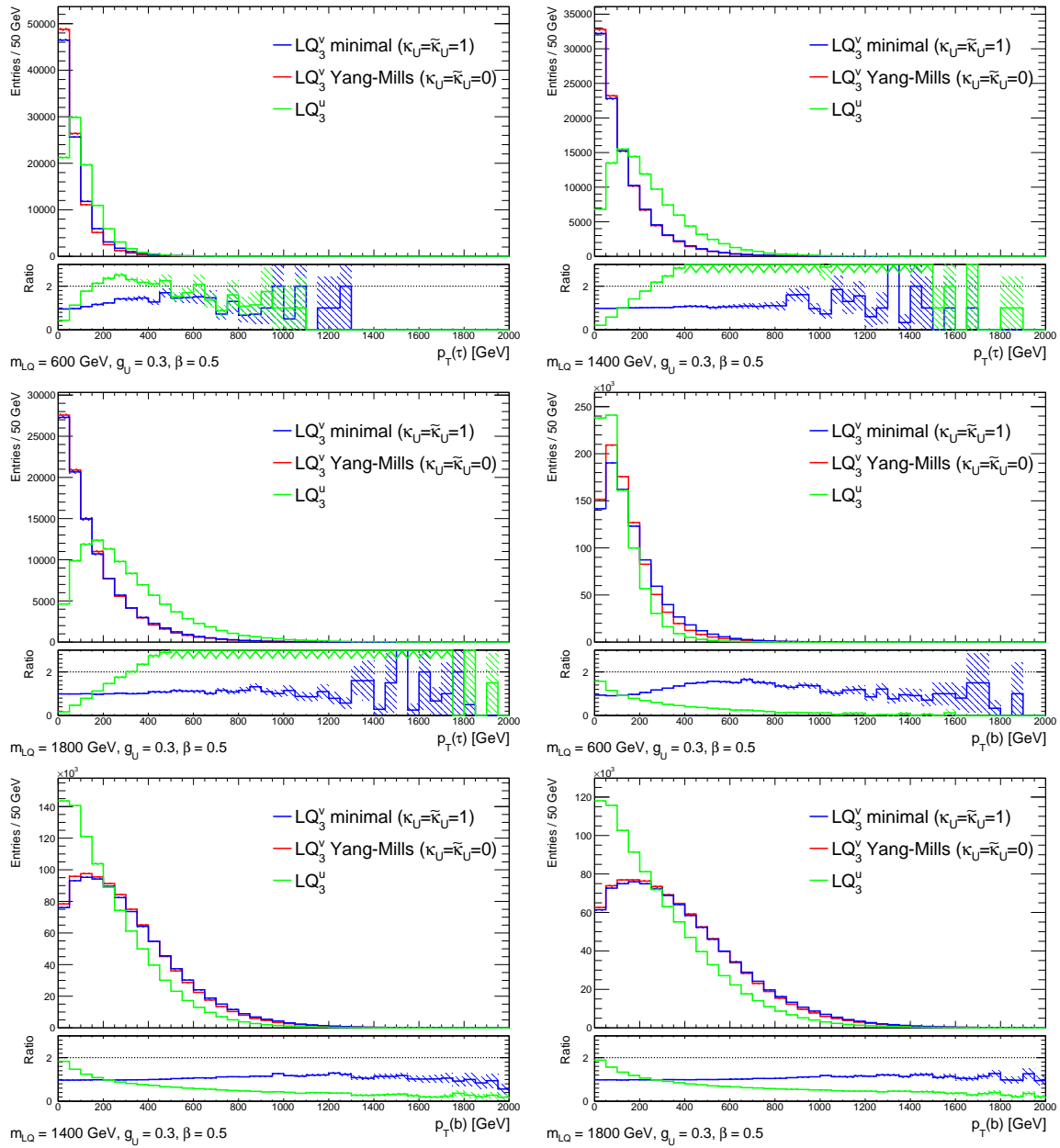


Figure C.3: Comparison of  $p_T(\tau)$  and  $p_T(b)$  between scalar LQ and vector LQ at different mass points

Figure C.4: Distribution of  $p_T$  of tau leptons and  $b$  quarks originating from top quark decays.

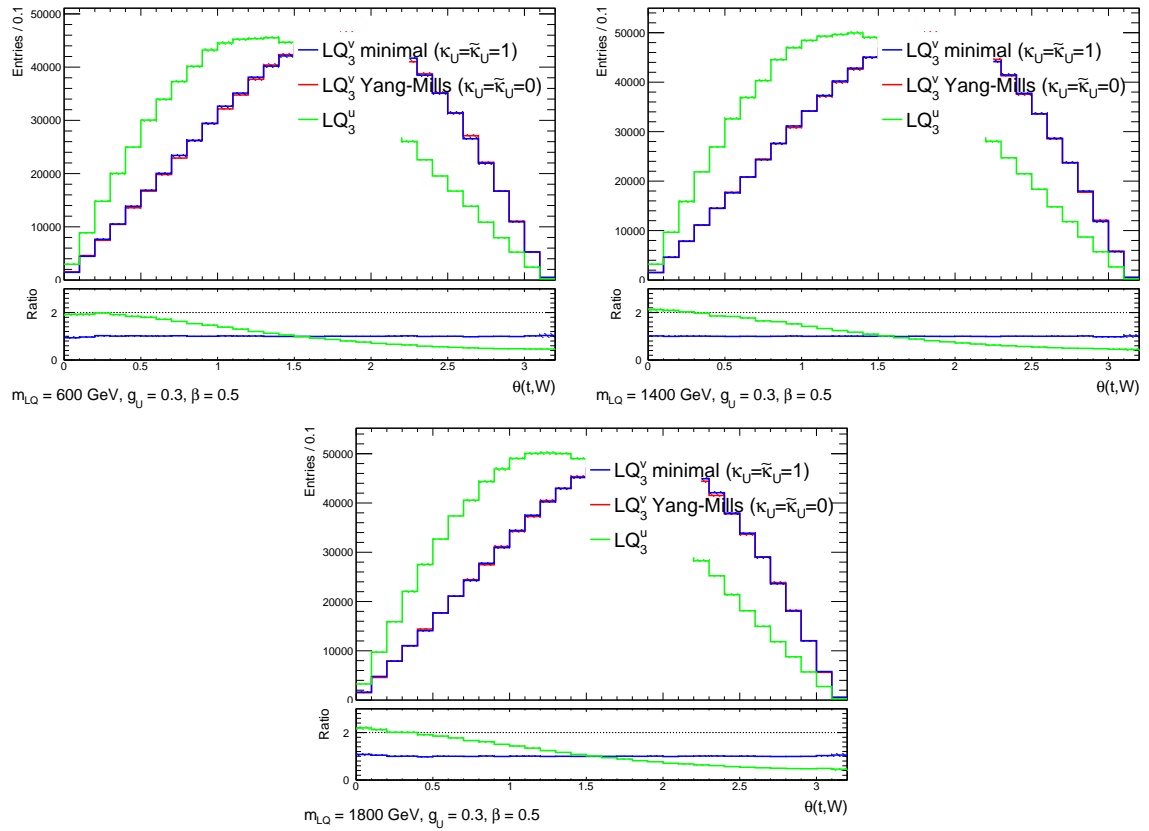


Figure C.5: Distribution of the angle between the top quark momentum in the LQ rest frame and the  $W$  boson momentum in the top quark rest frame

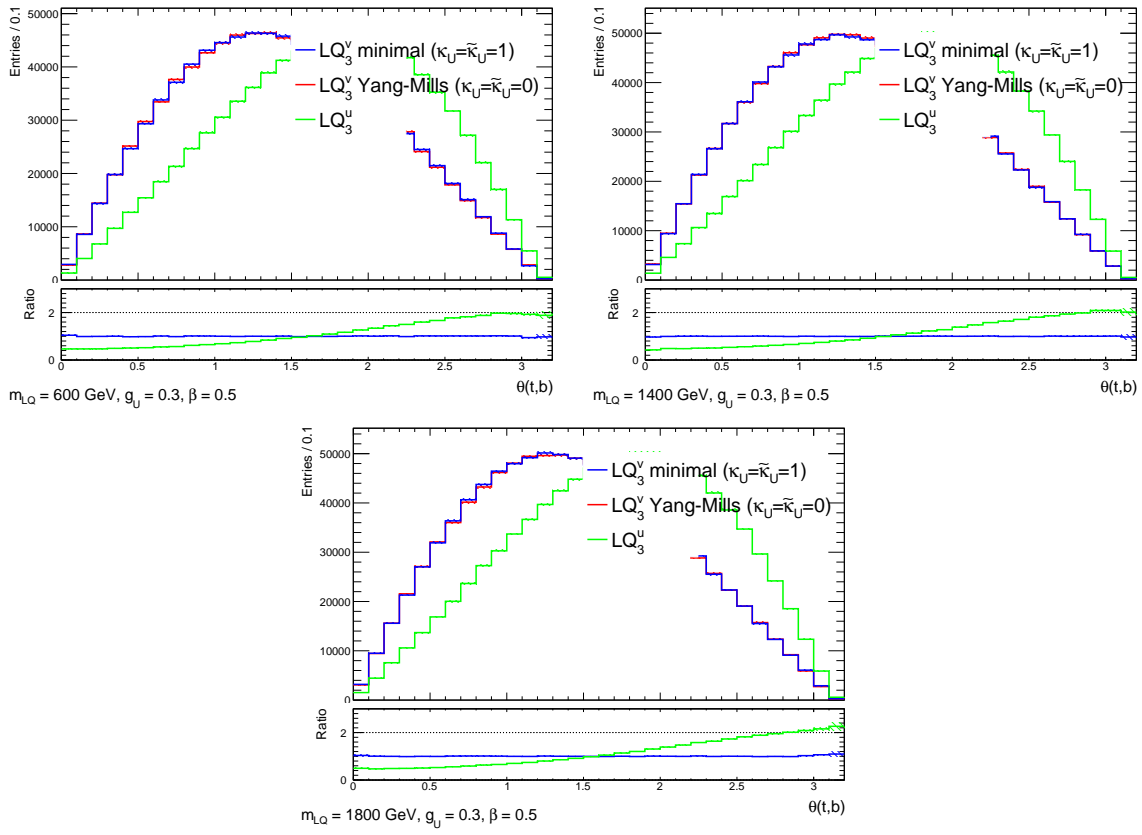


Figure C.6: Distribution of the angle between the top quark momentum in the LQ rest frame and the  $b$  quark momentum in the top quark rest frame.

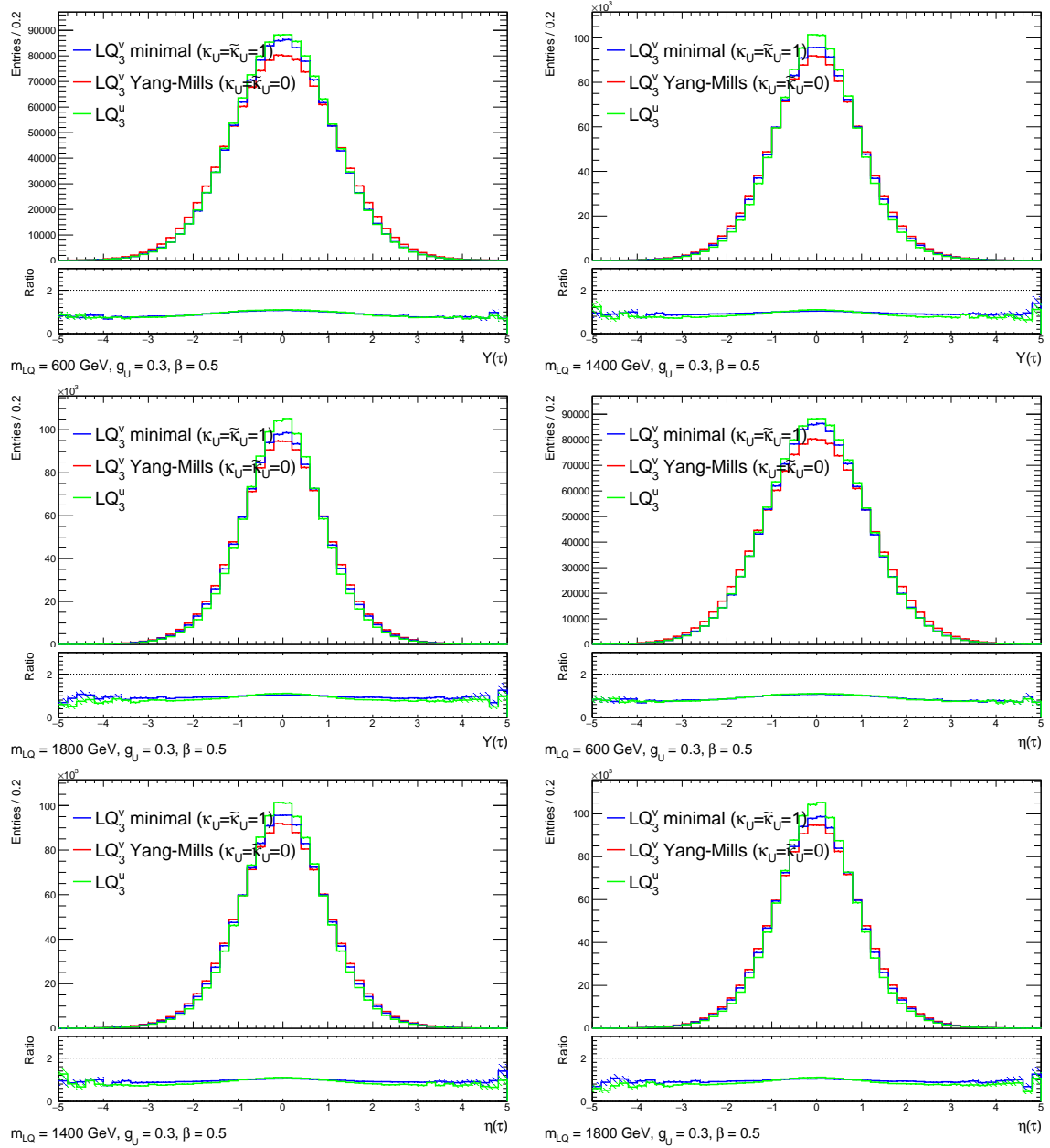


Figure C.7: Comparison of rapidity ( $Y$ ) and pseudorapidity ( $\eta$ ) of tau lepton between scalar LQ and vector LQ at different mass points

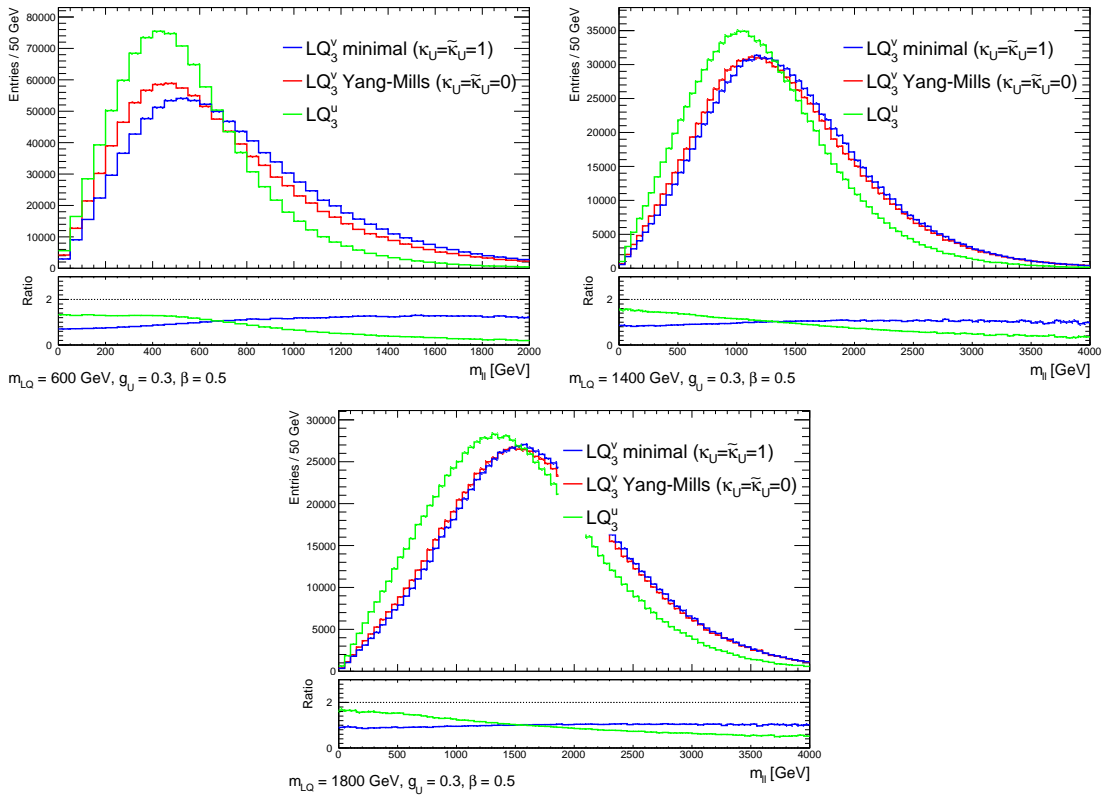
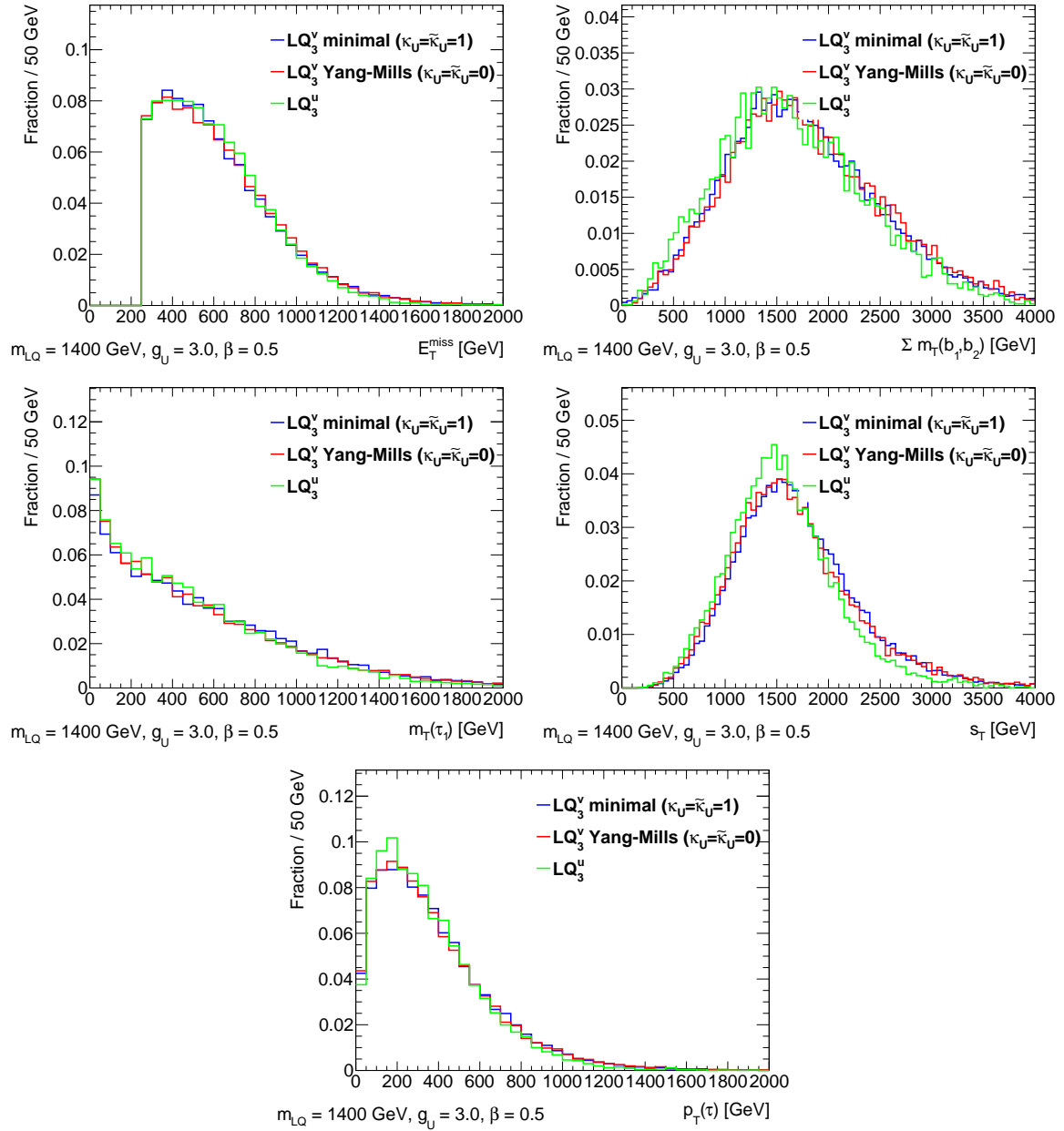


Figure C.8: Comparison of  $m_{ll}$  ( $l = \tau, \nu_\tau$ ) between scalar LQ and vector LQ at different mass points

Figure C.9: Distributions of variables defining the single-tau SRs, at  $m(\text{LQ}) = 1.4 \text{ TeV}$ .

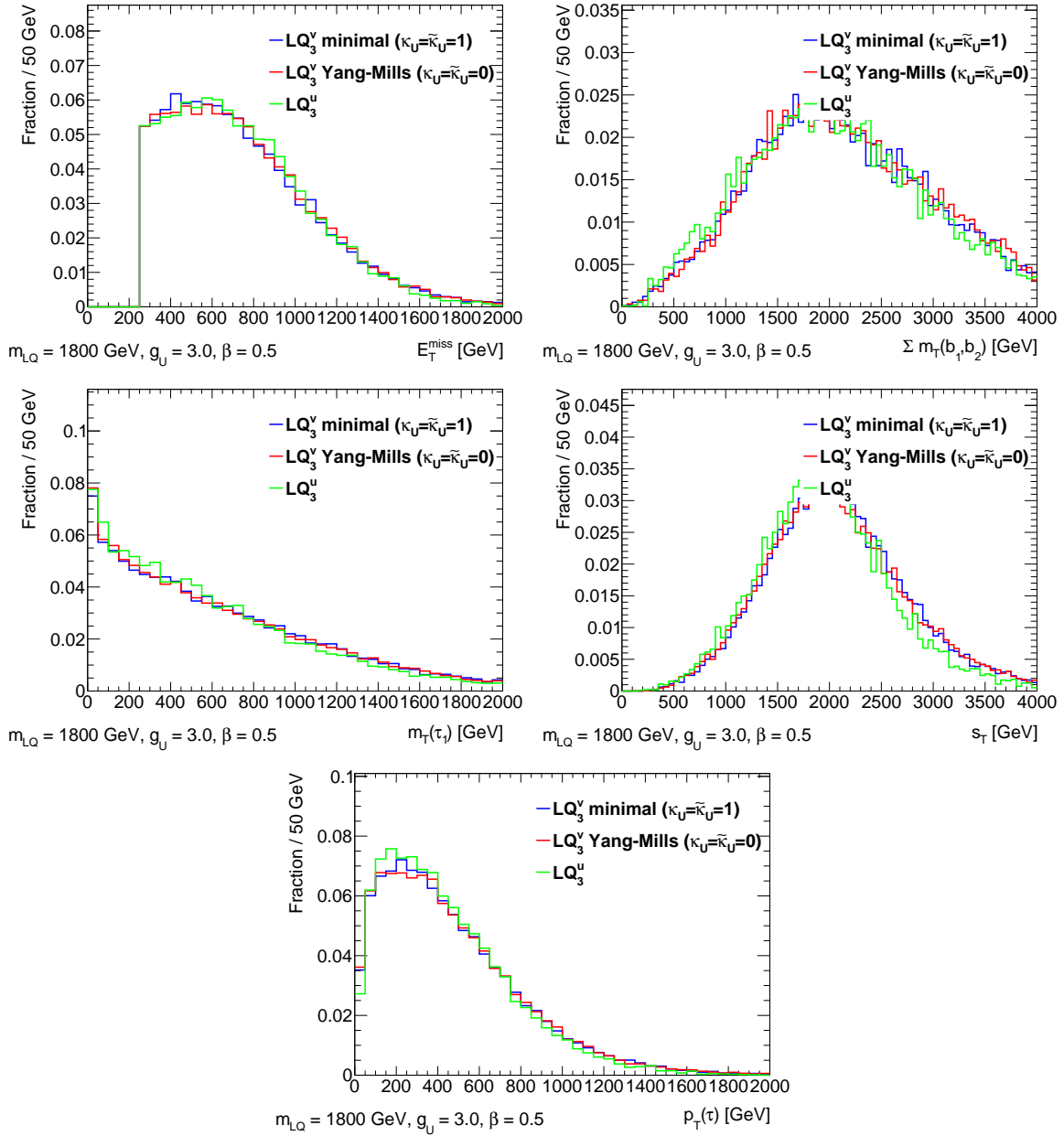


Figure C.10: Distributions of variables defining the single-tau SRs, at  $m(\text{LQ}) = 1.8 \text{ TeV}$ .

## C.2 Observed $CL_s$ Values

The observed  $CL_s$  values at the scanned signal points are shown in fig. C.11, with the same exclusion contours as in fig. 7.4. The points where the  $CL_s$  value is missing indicate failures in hypothesis tests, which is typically due to high signal contamination. These points can be still excluded by upper limit scans, which is shown in appendix C.3.

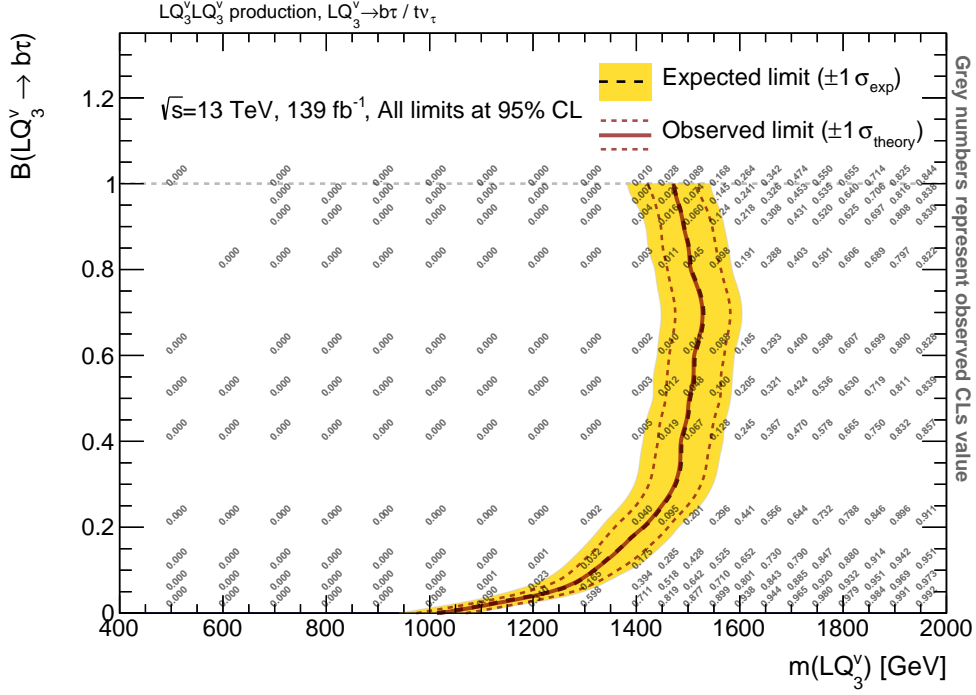
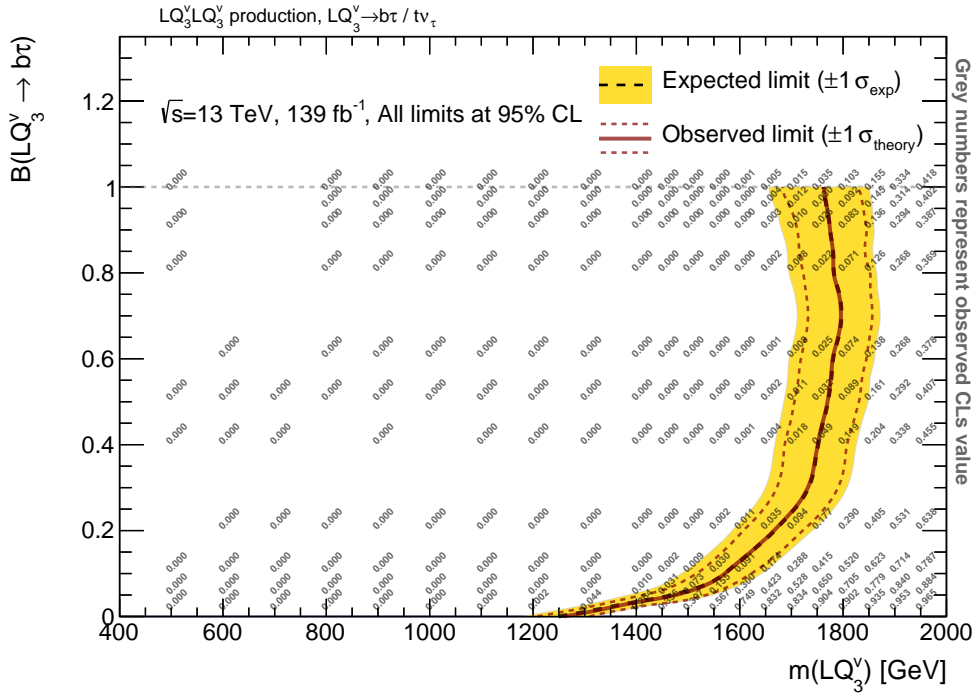
(a)  $LQ_3^V$  (minimal coupling)(b)  $LQ_3^V$  (Yang-Mills)

Figure C.11: Exclusion contours identical to fig. 7.4, with  $CL_s$  values for each signal point. Gray numbers represent the  $CL_s$  values.

### C.3 Observed Upper Limits on Cross Section

The results of upper limit scans are shown in fig. C.12. The scan returns upper limit values on signal strength parameter  $\mu_{\text{sig}}$ , which means signal strength above this value is excluded. The upper limit value scaled by the cross section of the signal point means the signal with cross section larger than the limit is excluded. Comparing the upper limits in fig. C.12 with the cross section values in tables 6.1 and 6.2, it is confirmed that the points with missing  $\text{CL}_s$  values in fig. C.11 are also excluded, as their upper limit values are far below the cross sections.

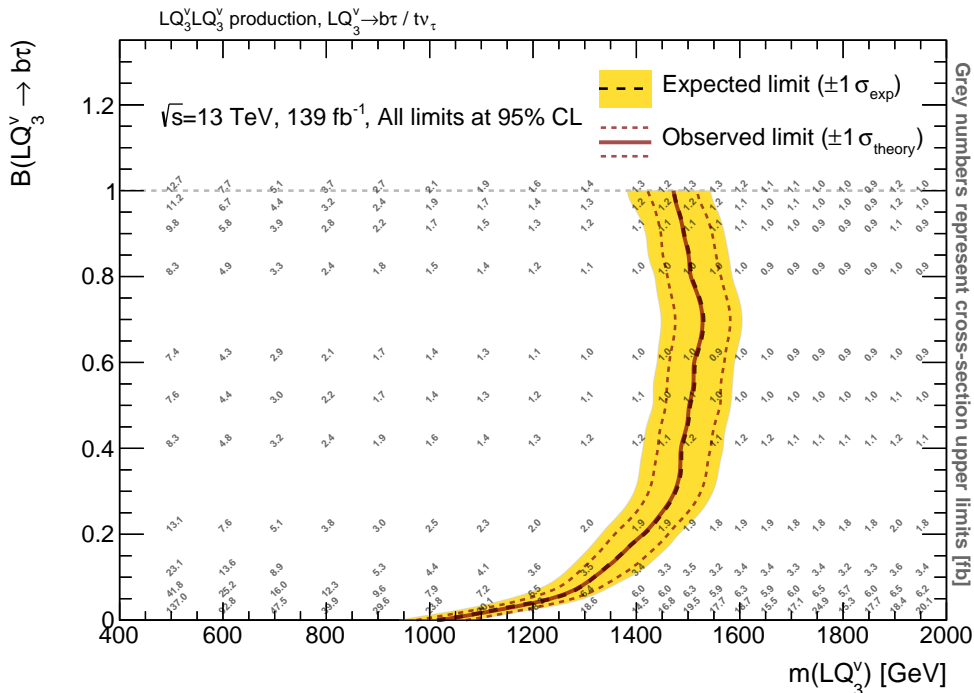
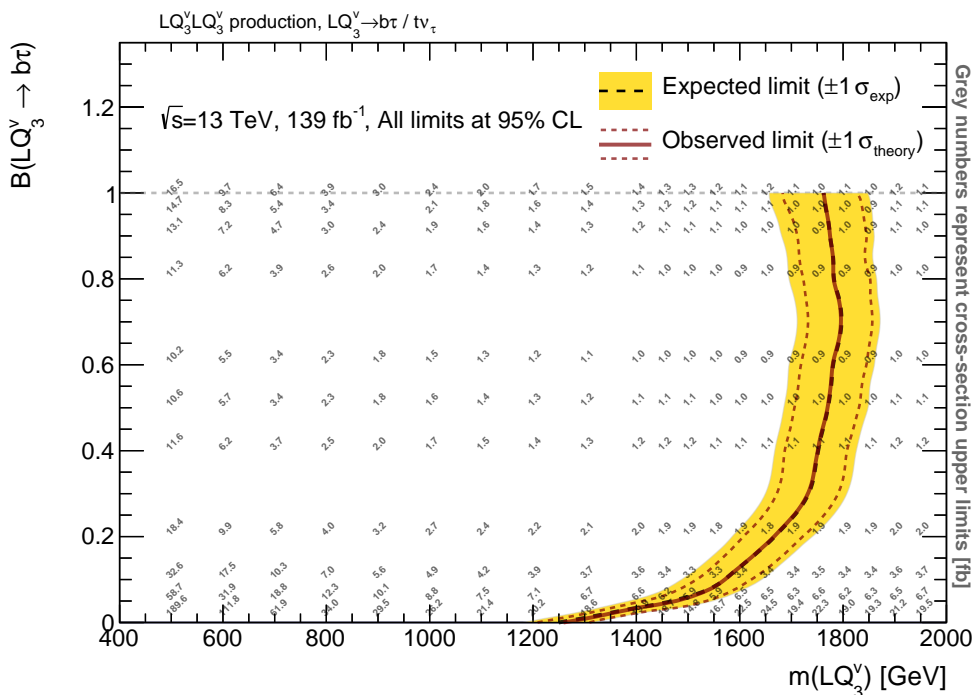
(a)  $LQ_3^V$  (minimal coupling)(b)  $LQ_3^V$  (Yang-Mills)

Figure C.12: Exclusion contours identical to fig. 7.4, with observed upper limits on cross section for each signal point. Gray numbers represent the upper limits.

# Selbständigkeitserklärung

Hiermit erkläre ich, die vorliegende Arbeit selbständig verfasst zu haben und keine anderen als die in der Arbeit angegebenen Quellen und Hilfsmittel benutzt zu haben.

Kyeong Ro Lee

München, den 28. Juni 2021